Inviscid global linear instability of compressible flow on an elliptic cone: Algorithmic developments

B y Vassilios Theofilis †

Rohnsterrassen 14, D-37085 Göttingen, GERMANY

tel./fax: +49 551 48 76 25 vassilios.theofilis@nu-modelling.com http://www.nu-modelling.com

(20 June 2002)

The subject of the present effort is numerical developments in support of a BiGlobal linear instability analysis[26] of the compressible three-dimensional steady laminar basic flows obtained within the framework of F61775-99-WE049. The first objective becomes extraction from the aforementioned results of the appropriate two-dimensional basic flow data. The assumption is made, and is verified in the numerical results to be increasingly applicable as the flow Mach number increases, that the dependence of the basic flow on an appropriately defined downstream spatial direction is much weaker than that in the wall-normal and the circumferential directions of the elliptic cone. In terms of the basic flow, derivatives in the downstream direction are thus neglected; in the disturbance equations an eigenmode Ansatz is introduced in this direction. A discussion is presented regarding the choice of coordinate system for the analysis. The viscous disturbance equations of the two-dimensional compressible partial-derivative eigenvalue problem are presented in cartesian coordinates. It is subsequently proposed that on grounds of numerical efficiency the analysis be performed in an inviscid framework on the elliptic confocal coordinate system. The governing equation is derived in the chosen coordinate system and numerical means for its discretisation are discussed.

In an inviscid global linear analysis the issue of avoidance of singularities of the governing equations through indentation of the path of integration must be addressed. However, the concept of direction is ill-defined in the framework of an inviscid global analysis. One alternative to shooting in both the local and the global theory is to pose the disturbance equations as a matrix eigenvalue problem on complex calculation grids. A new spectral collocation method has been devised, which employs this technique and is validated by solving several one-dimensional linear eigenvalue problems on different families of collocation grids. Tensor products of the optimal grids identified through the present effort can be employed for the solution of the two-dimensional eigenvalue problem at hand, if marginally amplified/damped or neutral modes are sought. The suite of numerical tools proposed for the BiGlobal instability analysis has been validated. First, model Poisson problems have been solved on the elliptic confocal coordinate system and the expected exponential convergence property has been demonstrated. Subsequently, three flow configurations in the subsonic, supersonic and hypersonic regimes have been solved. Most interestingly, large-scale non-azimuthally-periodic disturbances, inaccessible to classic linear theory, have been identified in all flow regimes.

REPORT DOCUMENTATION PAGE

Form Approved OMB No. 0704-0188

1. REPORT DATE *(DD-MM-YYYY)*	2. REPORT TYPE	3. DATES COVERED *(From – To)*
02-07-2002	Final Report	28 September 2000 - 28-Sep-01

4. TITLE AND SUBTITLE

Inviscid Global Linear Instability Of Compressible Flow On An Elliptic Cylinder: Algorithmic Developments

5a. CONTRACT NUMBER
F61775-00-WE069

5b. GRANT NUMBER

5c. PROGRAM ELEMENT NUMBER

6. AUTHOR(S)

Dr. Vassilios Theofilis

5d. PROJECT NUMBER

5d. TASK NUMBER

5e. WORK UNIT NUMBER

7. PERFORMING ORGANIZATION NAME(S) AND ADDRESS(ES)
Nu-modeling, Inc.
Rohnsterrassen 14
Gottingen D-37085
Germany

8. PERFORMING ORGANIZATION REPORT NUMBER

N/A

9. SPONSORING/MONITORING AGENCY NAME(S) AND ADDRESS(ES)

EOARD
PSC 802 BOX 14
FPO AE 09499-0014

10. SPONSOR/MONITOR'S ACRONYM(S)

11. SPONSOR/MONITOR'S REPORT NUMBER(S)
SPC 00-4069

12. DISTRIBUTION/AVAILABILITY STATEMENT

Approved for public release; distribution is unlimited.

13. SUPPLEMENTARY NOTES

14. ABSTRACT

This report results from a contract tasking Nu-modeling, Inc. as follows: The contractor will perform a three-dimensional inviscid analysis of the nonparallel steady compressible basic flow over an elliptic cone. The inviscid stability solutions have been proven in the past, within the framework of simplified instability theories, very useful in understanding the stability of 2-D supersonic/hypersonic boundary/shear layers and are extremely useful in getting to the essential physics at the heart of the problem at a much more moderate cost compared with the respective full viscous analysis. The proposed research has a threefold objective, 1) Derive the inviscid governing equation in a coordinate system appropriate for the elliptic cone geometry and discretise it using novel, to be developed, spectral collocation methods; 2) Tackle the issue of the boundary conditions associated with the system of equations to be solved; 3) Develop a theory analogous to the classic one-dimensional instability analyses for global instability analyses. In the latter case the integration grid will comprise two coupled real spatial directions and is defined on a real plane, as opposed to the real line of the former one-dimensional analysis. On completion of the proposed research the code necessary for compressible global linear instability analysis of the steady two-dimensional laminar basic flows being generated within the scope of F61775-99-WE049, will be developed and validated. If unexpected challenges are encountered with the novel elements of the inviscid analysis proposed, the focus will be shifted towards the full viscous global instability eigenvalue problem.

15. SUBJECT TERMS
EOARD, Combustion, Plasma Chemistry

16. SECURITY CLASSIFICATION OF:

a. REPORT	b. ABSTRACT	c. THIS PAGE	17. LIMITATION OF ABSTRACT	18, NUMBER OF PAGES	19a. NAME OF RESPONSIBLE PERSON
UNCLAS	UNCLAS	UNCLAS	UL	77	Wayne Donaldson

19b. TELEPHONE NUMBER *(Include area code)*
+44 (0)20 7514 4299

Standard Form 298 (Rev. 8/98)
Prescribed by ANSI Std. Z39-18

Contents

1. Introduction

The present effort concentrates on global linear instability analyses of the steady laminar flows on an elliptic cone presented in [25]. These flows are intrinsically three-dimensional; as a matter of fact the three-dimensionality of the geometry of the elliptic cone accounts for the departure of the laminar-turbulent transition process from the fairly well-understood scenaria on circular cones [21] and other axisymmetric bodies of revolution. Shedding light on the essentially three-dimensional transition process on the elliptic cone from the perspective of global linear analysis provides motivation for several current experimental [15, 16, 12, 6] and numerical [29, 30] efforts, as well as for the theoretical/numerical methodology described herein.

The most general framework in which a global linear instability analysis can be performed is that of three-dimensional linear theory in which all three spatial directions are resolved. This is consistent with the separability in the governing equations of time on one hand and the three spatial directions on the other. Formulation of the three-dimensional global linear eigenvalue problem is straightforward; however, its numerical solution is not feasible with present-generation computer architectures. Indeed, coupled resolution of *dim* spatial directions requires storage of two arrays for the real and imaginary parts of the eigenfunctions, each of size

$$5 \times 2^6 \times N^{2 \times dim} \times 10^{-9} \text{ Gbytes}$$

of core memory in primitive variables formulation and 64-bit arithmetic if N points resolve each spatial direction. The size of each array is doubled if 128-bit arithmetic is deemed to be necessary [7]. If a numerical method of optimal resolution power for a given number of discretisation points is utilised, such as spectral collocation, experience with the one-dimensional eigenvalue problem suggests that in excess of $N = 64$ must be used for adequate resolution of eigenfunction features at critical Reynolds numbers typical of boundary layer flows. The resulting sizes of the respective matrices are

$$\sim 22 \text{ Tbytes } \sim 5.4 \text{ Gbytes and } \sim 1.3 \text{ Mbytes},$$

if $dim = 3, 2$ and 1, respectively. It becomes clear that while the classic linear local analysis ($dim = 1$) requires very modest computing effort and is indeed part of industrial prediction toolkits, the main memory required for a three-dimensional linear instability analysis is well beyond any currently available or forecast computing technology. Between the two limits, a global linear analysis based on solution of the two-dimensional linear eigenvalue problem is well feasible and has indeed been performed using a variety of numerical methods and platforms, delivering results inaccessible to local theory (e.g. [22, 24]) or new insights into old instability problems (e.g. [28]); a review is presented in [27].

It thus becomes clear that in order to proceed with a global analysis of the elliptic cone basic flows the disturbance equations must be posed in the framework of solution of a *two-dimensional* eigenvalue problem. The underlying assumption is that the basic flow is independent of one spatial direction; in the problem at hand an appropriate direction must be identified such that the dependence of the basic flow on it is much weaker than that on the other two spatial directions. While the arc-length direction is an obvious candidate to be considered as homogeneous in the global instability problem, the choice of the other two spatial directions is not unique. Indeed, three alternative directions complementing the arc-length and wall-normal coordinates are identified in what follows. From the point of view of numerical feasibility, the elliptic confocal coordinate system is one natural basis on which to express and collocate the various forms of the two-dimensional compressible eigenvalue problems.

The viscous two-dimensional eigenvalue problem is derived herein in cartesian coordinates. From it the generalised Rayleigh equation presented in [25] may be derived; the latter is expressed here in the elliptic confocal coordinate system. If no loss of physical information is to be expected it is attractive to consider working with the matrices discretising the inviscid global eigenvalue problem, whose size is $(3/5)^2$ that of their viscous counterparts. However, a new issue is raised when working in an inviscid framework, namely the appearance of critical layers and potential singularities of the governing

4 *V. Theofilis*

equations. This problem is well-known in local linear theory, where its solution through indentation of the path of integration is straightforward. This is so because there is no ambiguity in defining the path of integration; in other words, the line on which basic flow data is defined in a boundary-layer context is the wall-normal spatial direction. The necessary basic flow data are obtained on the indented path by Taylor expansion around the critical layer. In such a framework, efficient numerical approaches exist, based on finite-differences and shooting [8], to obtain the leading eigenvalue. In a global analysis on the elliptic cone, on the other hand, the basic flow is defined on a plane and both concepts of *integration-path* and *shooting* are inapplicable. This led us to propose a new algorithm for the integration of the inviscid disturbance equations, based on complex spectral collocation grids. Technical details are presented by Theofilis *et al.* [13]. Tensor products of the optimal grids identified through the present effort will be employed for the solution of the two-dimensional eigenvalue problem at hand.

Progress has been made on several fronts. Firstly, in § 2 we present for the first time the viscous compressible partial-derivative eigenvalue problem in cartesian coordinates. The inviscid limit of the eigenvalue problem is then recalled [25] as being the most efficient method of analysis from a numerical point of view. The elliptic confocal coordinate system is thus introduced in § 3, which on the one hand preserves the numerical advantage of efficiency and on the other offers natural means of resolving boundary-layer flow features by an analytic exponentially stretched body-fitted coordinate system. Secondly, we also discuss in this section the continuing quest to express the equations of motion in alternative coordinate systems. An approximation of the type made to derive the two-dimensional eigenvalue problem in cartesian coordinates must be made subsequently and it is interesting to compare the respective systems with respect to optimal representation of the underlying physical instability mechanisms. Ultimately, experience from experiment could decide the optimal choice of coordinate system.

The main thrust of the current effort has been along the first path and in § 4 we present the numerical means by which the generalised Rayleigh equation may be collocated on the elliptic confocal coordinate system and solved as either a temporal or a spatial two-dimensional eigenvalue problem at the same level of numerical effort. However, in view of the issue of two-dimensional critical layers, particular to the inviscid two-dimensional eigenvalue problem, we proceed in § 5 to elaborate on the concept of a complex calculation grid. The latter permits performing inviscid instability analyses by solving the eigenvalue problem in a direct manner. Several validation cases in the limit of one-dimensional linear inviscid equations are presented. Attention is then focussed in § 6 on the BiGlobal eigenvalue problem. First, the proposed spectral collocation numerical discretisation scheme is validated by solution of Poisson problems on the elliptic confocal coordinate system. Subsequently, two-dimensional planes of steady basic flow data on different aspect ratio elliptic cones are extracted from three-dimensional solutions at $M = 0.5, 4$ and 8. No analysis from a physical point of view as such has been performed here; rather, attention has been focussed on numerical aspects, such as feasibility of the methodology, resolution and its influence on different classes of eigendisturbances and extent of the integration domain and its relation to the boundary conditions imposed. It is demonstrated that application of BiGlobal analysis is relatively straightforward in terms of the resolution necessary for subsonic flow, although the assumptions underlying the derivation of the compressible generalised Rayleigh equation are increasingly applicable to supersonic/hypersonic flow. Classes of BiGlobal eigendisturbances that can be recovered accurately in high-speed flow are identified. Interestingly, results obtained provide indications that BiGlobal instability theory can be utilised as an alternative to classic linear theory in investigations of vortex breakdown over delta wing configurations in high-angle of attack and as a tool alternative to DNS in computational aeroacoustics studies. A short discussion in § 7 summarises the present effort, while we use the Appendix to present technical details.

Contract No. F61775-00-WE069

2. The viscous compressible two-dimensional eigenvalue problem

In this section we start from first principles to derive the equations describing the compressible two-dimensional eigenvalue problem. This governs small-amplitude perturbations developing upon a steady laminar compressible basic state which is *inhomogeneous* in two spatial directions. The amplitude functions themselves are two-dimensional functions of the resolved spatial directions. We choose to focus the discussion on cartesian coordinates in view of their wider utility as compared with any of the body-fitted elliptic cone coordinate systems discussed in the previous section. In this framework any flow quantity may be decomposed as

$$\mathbf{q} = \bar{\mathbf{q}}(x, y) + \varepsilon\, \hat{\mathbf{q}}(x, y)\, E, \tag{2.1}$$

where

$$E = \exp\left[i(\beta z - \omega t)\right]$$

and $\mathbf{q} = (\rho, u, v, w, p)^{\mathrm{T}}$ is the vector of the three-dimensional nonconservative variables embedded in cartesian space $Oxyz$, $\bar{\mathbf{q}} = (\bar{\rho}(x, y), \bar{u}(x, y), \bar{v}(x, y), \bar{w}(x, y), \bar{p}(x, y))^{\mathrm{T}}$ is the vector of the *two-dimensional* steady basic flow quantities and $\hat{\mathbf{q}} = (\hat{\rho}(x, y), \hat{u}(x, y), \hat{v}(x, y), \hat{w}(x, y), \hat{p}(x, y))^{\mathrm{T}}$ is that of the amplitude functions of the three-dimensional disturbances, which are periodic in one spatial direction alone, z. As usual, an equation of state for ideal gases relates pressure p and density ρ through temperature T,

$$\gamma M^2 p = \rho T, \tag{2.2}$$

and a general law relating viscosity μ and temperature is adopted. Upon decomposition of temperature and viscosity into their steady two-dimensional and unsteady disturbance components one also has

$$T = \overline{T}(x, y) + \varepsilon\, \hat{T}(x, y)\, E,$$
$$\mu = \overline{\mu}(x, y) + \varepsilon\, \hat{\mu}(x, y)\, E. \tag{2.3}$$

Further quantities introduced are the viscous stresses

$$\tau^{XX} = (\mu/Re)\left[4/3 u_x - 2/3(v_y + w_z)\right] \tag{2.4}$$

$$\tau^{YY} = (\mu/Re)\left[4/3 v_y - 2/3(u_x + w_z)\right] \tag{2.5}$$

$$\tau^{ZZ} = (\mu/Re)\left[4/3 w_z - 2/3(u_x + v_y)\right] \tag{2.6}$$

$$\tau^{XY} = \tau^{YX} = (\mu/Re)(u_y + v_x) \tag{2.7}$$

$$\tau^{XZ} = \tau^{ZX} = (\mu/Re)(u_z + w_x) \tag{2.8}$$

$$\tau^{YZ} = \tau^{ZY} = (\mu/Re)(v_z + w_y), \tag{2.9}$$

and the viscous heat fluxes

$$Q^X = -\frac{\mu T_x}{(\gamma - 1)M^2 PrRe} \tag{2.10}$$

$$Q^Y = -\frac{\mu T_y}{(\gamma - 1)M^2 PrRe} \tag{2.11}$$

$$Q^Z = -\frac{\mu T_z}{(\gamma - 1)M^2 PrRe}. \tag{2.12}$$

In this context, the equations of motion can be written in conservative form,

$$\rho_t + (\rho u)_x + (\rho v)_y + (\rho w)_z = 0 \tag{2.13}$$

$$(\rho u)_t + (p + \rho u^2)_x + (\rho uv)_y + (\rho uw)_z - \tau_x^{XX} - \tau_y^{XY} - \tau_z^{XZ} = 0 \tag{2.14}$$

$$(\rho v)_t + (\rho uv)_x + (p + \rho v^2)_y + (\rho vw)_z - \tau_x^{XY} - \tau_y^{YY} - \tau_z^{YZ} = 0 \tag{2.15}$$

$$(\rho w)_t + (\rho uw)_x + (\rho vw)_y + (p + \rho w^2)_z - \tau_x^{XZ} - \tau_y^{YZ} - \tau_z^{ZZ} = 0 \tag{2.16}$$

$$e_t + [u(e + p)]_x + [v(e + p)]_y + [w(e + p)]_z$$
$$+ Q_x^X + Q_y^Y + Q_z^Z$$
$$- \left[u\tau^{XX} + v\tau^{XY} + w\tau^{XZ} \right]_x$$
$$- \left[u\tau^{XY} + v\tau^{YY} + w\tau^{YZ} \right]_y$$
$$- \left[u\tau^{XZ} + v\tau^{YZ} + w\tau^{ZZ} \right]_z = 0 \tag{2.17}$$

where

$$e = \frac{1}{\gamma - 1}p + \frac{1}{2}\rho(u^2 + v^2 + w^2) \tag{2.18}$$

and subscripts denote partial differentiation with respect to an independent variable. The global viscous linear analysis proceeds by substitution of (2.1) into (2.13-2.17) upon which systems of equations at $O(1)$, $O(\varepsilon)$ and $O(\varepsilon^2)$ are obtained in a manner conceptually identical with that of classic linear theory [17]. The terms at $O(1)$ represent the steady basic state, those at $O(\varepsilon^2)$ are neglected in a linear framework, while the system of equations to be solved at $O(\varepsilon)$ reads

Disturbance Continuity

$$\hat{v}\,\overline{\rho}_y + \overline{v}\,\hat{\rho}_y + \hat{u}\,\overline{\rho}_x + \overline{u}\,\hat{\rho}_x + \hat{\rho}\,(-i\,\omega + i\,\beta\,\overline{w} + \overline{v}_y + \overline{u}_x) + \overline{\rho}\,(i\,\beta\,\hat{w} + \hat{v}_y + \hat{u}_x) = 0, \qquad (2.19)$$

Disturbance X-Momentum

$$\hat{u}\,\overline{v}\,\overline{\rho}_y + \overline{u}\,\hat{v}\,\overline{\rho}_y + \overline{u}\,\overline{v}\,\hat{\rho}_y + \hat{p}_x + 2\,\overline{u}\,\hat{u}\,\overline{\rho}_x + \overline{u}^2\,\hat{\rho}_x$$

$$+\hat{\rho}\left\{\overline{v}\,\overline{u}_y + \overline{u}\,(-i\,\omega + i\,\beta\,\overline{w} + \overline{v}_y + 2\,\overline{u}_x)\right\}$$

$$+\overline{\rho}\,(-i\,\omega\,\hat{u} + i\,\beta\,\hat{u}\,\overline{w} + i\,\beta\,\overline{u}\,\hat{w} + \hat{v}\,\overline{u}_y + \overline{v}\,\hat{u}_y + \hat{u}\,\overline{v}_y + \overline{u}\,\hat{v}_y + 2\,\hat{u}\,\overline{u}_x + 2\,\overline{u}\,\hat{u}_x)$$

$$+\frac{1}{3\,Re}\Big\{ - 3\,\overline{\mu}_y\,\hat{u}_y - 3\,\hat{\mu}\,\overline{u}_{yy} + 2\,i\,\beta\,\hat{w}\,\overline{\mu}_x + 2\,\hat{v}_y\,\overline{\mu}_x + 2\,\overline{v}_y\,\hat{\mu}_x - 4\,\hat{\mu}_x\,\overline{u}_x$$

$$-4\,\overline{\mu}_x\,\hat{u}_x - 3\,\hat{\mu}_y\,(\overline{u}_y + \overline{v}_x) - 3\,\overline{\mu}_y\,\hat{v}_x - 3\,i\,\beta\,\hat{\mu}\,\overline{w}_x - \hat{\mu}\,\overline{v}_{xy} - 4\,\hat{\mu}\,\overline{u}_{xx}$$

$$- \overline{\mu}\left(-3\,\beta^2\,\hat{u} + 3\,\hat{u}_{yy} + i\,\beta\,\hat{w}_x + \hat{v}_{xy} + 4\,\hat{u}_{xx}\right)\Big\} = 0, \qquad (2.20)$$

Disturbance Y-Momentum

$$\hat{p}_y + 2\,\overline{v}\,\hat{v}\,\overline{\rho}_y + \overline{v}^2\,\hat{\rho}_y + \hat{u}\,\overline{v}\,\overline{\rho}_x + \overline{u}\,\hat{v}\,\overline{\rho}_x + \overline{u}\,\overline{v}\,\hat{\rho}_x$$

$$+\hat{\rho}\left\{\overline{v}\,(-i\,\omega + i\,\beta\,\overline{w} + 2\,\overline{v}_y + \overline{u}_x) + \overline{u}\,\overline{v}_x\right\}$$

$$+\overline{\rho}\,(-i\,\omega\,\hat{v} + i\,\beta\,\hat{v}\,\overline{w} + i\,\beta\,\overline{v}\,\hat{w} + 2\,\hat{v}\,\overline{v}_y + 2\,\overline{v}\,\hat{v}_y + \hat{v}\,\overline{u}_x + \overline{v}\,\hat{u}_x + \hat{u}\,\overline{v}_x + \overline{u}\,\hat{v}_x)$$

$$\frac{1}{3\,Re}\Big\{ + 2\,i\,\beta\,\hat{w}\,\overline{\mu}_y - 4\,\hat{\mu}_y\,\overline{v}_y - 4\,\overline{\mu}_y\,\hat{v}_y - 3\,i\,\beta\,\hat{\mu}\,\overline{w}_y - 4\,\hat{\mu}\,\overline{v}_{yy} - 3\,\hat{u}_y\,\overline{\mu}_x$$

$$-3\,\overline{u}_y\,\hat{\mu}_x + 2\,\hat{\mu}_y\,\overline{u}_x + 2\,\overline{\mu}_y\,\hat{u}_x - 3\,\hat{\mu}_x\,\overline{v}_x - 3\,\overline{\mu}_x\,\hat{v}_x - \hat{\mu}\,\overline{u}_{xy} - 3\,\hat{\mu}\,\overline{v}_{xx}$$

$$- \overline{\mu}\left(-3\,\beta^2\,\hat{v} + i\,\beta\,\hat{w}_y + 4\,\hat{v}_{yy} + \hat{u}_{xy} + 3\,\hat{v}_{xx}\right)\Big\} = 0, \qquad (2.21)$$

V. Theofilis

Disturbance Z-Momentum

$$i\,\beta\,\hat{p} - i\,\omega\,\overline{\rho}\,\hat{w} + 2\,i\,\beta\,\overline{\rho}\,\overline{w}\,\hat{w} + \hat{v}\,\overline{w}\,\overline{\rho}_y + \overline{v}\,\hat{w}\,\overline{\rho}_y + \overline{v}\,\overline{w}\,\hat{\rho}_y + \overline{\rho}\,\hat{w}\,\overline{v}_y + \overline{\rho}\,\overline{w}\,\hat{v}_y$$

$$+\overline{\rho}\,\hat{v}\,\overline{w}_y + \overline{\rho}\,\overline{v}\,\hat{w}_y + \hat{u}\,\overline{w}\,\overline{\rho}_x + \overline{u}\,\hat{w}\,\overline{\rho}_x + \overline{u}\,\overline{w}\,\hat{\rho}_x + \overline{\rho}\,\hat{w}\,\overline{u}_x + \overline{\rho}\,\overline{w}\,\hat{u}_x + \overline{\rho}\,\hat{u}\,\overline{w}_x$$

$$+\hat{\rho}\left(-i\,\omega\,\overline{w} + i\,\beta\,\overline{w}^2 + \overline{w}\,\overline{v}_y + \overline{v}\,\overline{w}_y + \overline{w}\,\overline{u}_x + \overline{u}\,\overline{w}_x\right) + \overline{\rho}\,\overline{u}\,\hat{w}_x$$

$$+\frac{1}{3\,Re}\Big\{-3\,i\,\beta\,\hat{v}\,\overline{\mu}_y + 2\,i\,\beta\,\hat{\mu}\,\overline{v}_y - 3\,\hat{\mu}_y\,\overline{w}_y - 3\,\overline{\mu}_y\,\hat{w}_y - 3\,\hat{\mu}\,\overline{w}_{yy}$$

$$-3\,i\,\beta\,\hat{u}\,\overline{\mu}_x + 2\,i\,\beta\,\hat{\mu}\,\overline{u}_x - 3\,\hat{\mu}_x\,\overline{w}_x - 3\,\overline{\mu}_x\,\hat{w}_x - 3\,\hat{\mu}\,\overline{w}_{xx}$$

$$-\overline{\mu}\left(-4\,\beta^2\,\hat{w} + i\,\beta\,\hat{v}_y + 3\,\hat{w}_{yy} + i\,\beta\,\hat{u}_x + 3\,\hat{w}_{xx}\right)\Big\} = 0, \qquad (2.22)$$

Disturbance Energy

$$\frac{i\,\omega}{2(\gamma-1)}\Big\{2\,\hat{p} + (\gamma-1)\left[\hat{\rho}\left(\overline{u}^2 + \overline{v}^2 + \overline{w}^2\right) + 2\,\overline{\rho}\left(\overline{u}\,\hat{u} + \overline{v}\,\hat{v} + \overline{w}\,\hat{w}\right)\right]\Big\}$$

$$+\frac{1}{2\,(\gamma-1)}\Big\{(\gamma-1)\,\overline{u}^3\,\hat{\rho}_x + 2\,\gamma\,\hat{p}\,\overline{u}_x - \hat{\rho}\,\overline{v}^2\,\overline{u}_x + \gamma\,\hat{\rho}\,\overline{v}^2\,\overline{u}_x - 2\,\overline{\rho}\,\overline{v}\,\hat{v}\,\overline{u}_x$$

$$+2\,\gamma\,\overline{\rho}\,\overline{v}\,\hat{v}\,\overline{u}_x - \hat{\rho}\,\overline{w}^2\,\overline{u}_x + \gamma\,\hat{\rho}\,\overline{w}^2\,\overline{u}_x - 2\,\overline{\rho}\,\overline{w}\,\hat{w}\,\overline{u}_x$$

$$+2\,\gamma\,\overline{\rho}\,\overline{w}\,\hat{w}\,\overline{u}_x + 2\,\gamma\,\overline{p}\,\hat{u}_x - \overline{\rho}\,\overline{v}^2\,\hat{u}_x + \gamma\,\overline{\rho}\,\overline{v}^2\,\hat{u}_x$$

$$-\overline{\rho}\,\overline{w}^2\,\hat{u}_x + \gamma\,\overline{\rho}\,\overline{w}^2\,\hat{u}_x + 3\,(\gamma-1)\,\overline{u}^2\left(\hat{\rho}\,\overline{u}_x + \overline{\rho}\,\hat{u}_x\right)$$

$$\hat{u}\Big[2\,\gamma\,\overline{p}_x + (\gamma-1)$$

$$\left(3\,\overline{u}^2\,\overline{\rho}_x + \overline{v}^2\,\overline{\rho}_x + \overline{w}^2\,\overline{\rho}_x + 6\,\overline{\rho}\,\overline{u}\,\overline{u}_x + 2\,\overline{\rho}\,\overline{v}\,\overline{v}_x + 2\,\overline{\rho}\,\overline{w}\,\overline{w}_x\right)\Big]\Big\}$$

$$+\frac{\overline{u}}{2\,(\gamma-1)}\Big\{+2\,\gamma\,\hat{p}_x - 2\,\overline{v}\,\hat{v}\,\overline{\rho}_x + 2\,\gamma\,\overline{v}\,\hat{v}\,\overline{\rho}_x - 2\,\overline{w}\,\hat{w}\,\overline{\rho}_x$$

$$+2\,\gamma\,\overline{w}\,\hat{w}\,\overline{\rho}_x - \overline{v}^2\,\hat{\rho}_x + \gamma\,\overline{v}^2\,\hat{\rho}_x - \overline{w}^2\,\hat{\rho}_x + \gamma\,\overline{w}^2\,\hat{\rho}_x$$

$$-2\,\hat{\rho}\,\overline{v}\,\overline{v}_x + 2\,\gamma\,\hat{\rho}\,\overline{v}\,\overline{v}_x - 2\,\overline{\rho}\,\hat{v}\,\overline{v}_x + 2\,\gamma\,\overline{\rho}\,\hat{v}\,\overline{v}_x$$

$$-2\,\overline{\rho}\,\overline{v}\,\hat{v}_x + 2\,\gamma\,\overline{\rho}\,\overline{v}\,\hat{v}_x - 2\,\hat{\rho}\,\overline{w}\,\overline{w}_x + 2\,\gamma\,\hat{\rho}\,\overline{w}\,\overline{w}_x$$

$$-2\,\overline{\rho}\,\hat{w}\,\overline{w}_x + 2\,\gamma\,\overline{\rho}\,\hat{w}\,\overline{w}_x - 2\,\overline{\rho}\,\overline{w}\,\hat{w}_x + 2\,\gamma\,\overline{\rho}\,\overline{w}\,\hat{w}_x\Big\}$$

$$+\frac{1}{2\,(\gamma-1)}\Big\{\,(\gamma-1)\,\bar{v}^3\,\hat{\rho}_y + 2\,\gamma\,\hat{p}\,\bar{v}_y - \hat{\rho}\,\bar{u}^2\,\bar{v}_y + \gamma\,\hat{\rho}\,\bar{u}^2\,\bar{v}_y - 2\,\overline{\rho}\,\bar{u}\,\hat{u}\,\bar{v}_y$$

$$+2\,\gamma\,\overline{\rho}\,\bar{u}\,\hat{u}\,\bar{v}_y - \hat{\rho}\,\bar{w}^2\,\bar{v}_y + \gamma\,\hat{\rho}\,\bar{w}^2\,\bar{v}_y - 2\,\overline{\rho}\,\bar{w}\,\hat{w}\,\bar{v}_y + 2\,\gamma\,\overline{\rho}\,\bar{w}\,\hat{w}\,\bar{v}_y$$

$$+2\,\gamma\,\bar{p}\,\hat{v}_y - \overline{\rho}\,\bar{u}^2\,\hat{v}_y + \gamma\,\overline{\rho}\,\bar{u}^2\,\hat{v}_y - \overline{\rho}\,\bar{w}^2\,\hat{v}_y + \gamma\,\overline{\rho}\,\bar{w}^2\,\hat{v}_y$$

$$+3\,(-1+\gamma)\,\bar{v}^2\,(\hat{\rho}\,\bar{v}_y + \overline{\rho}\,\hat{v}_y)$$

$$\hat{v}\,\Big[2\,\gamma\,\bar{p}_y + (\gamma-1)$$

$$\Big(\bar{u}^2\,\overline{\rho}_y + 3\,\bar{v}^2\,\overline{\rho}_y + \bar{w}^2\,\overline{\rho}_y + 2\,\overline{\rho}\,\bar{u}\,\bar{u}_y + 6\,\overline{\rho}\,\bar{v}\,\bar{v}_y + 2\,\overline{\rho}\,\bar{w}\,\bar{w}_y\Big)\Big]\Big\}$$

$$+\frac{\bar{v}}{2\,(\gamma-1)}\Big\{2\,\gamma\,\hat{p}_y - 2\,\bar{u}\,\hat{u}\,\overline{\rho}_y + 2\,\gamma\,\bar{u}\,\hat{u}\,\overline{\rho}_y - 2\,\bar{w}\,\hat{w}\,\overline{\rho}_y + 2\,\gamma\,\bar{w}\,\hat{w}\,\overline{\rho}_y$$

$$-\bar{u}^2\,\hat{\rho}_y + \gamma\,\bar{u}^2\,\hat{\rho}_y - \bar{w}^2\,\hat{\rho}_y + \gamma\,\bar{w}^2\,\hat{\rho}_y - 2\,\hat{\rho}\,\bar{u}\,\bar{u}_y + 2\,\gamma\,\hat{\rho}\,\bar{u}\,\bar{u}_y$$

$$-2\,\overline{\rho}\,\hat{u}\,\bar{u}_y + 2\,\gamma\,\overline{\rho}\,\hat{u}\,\bar{u}_y - 2\,\overline{\rho}\,\bar{u}\,\hat{u}_y + 2\,\gamma\,\overline{\rho}\,\bar{u}\,\hat{u}_y - 2\,\hat{\rho}\,\bar{w}\,\bar{w}_y$$

$$+2\,\gamma\,\hat{\rho}\,\bar{w}\,\bar{w}_y - 2\,\overline{\rho}\,\hat{w}\,\bar{w}_y + 2\,\gamma\,\overline{\rho}\,\hat{w}\,\bar{w}_y - 2\,\overline{\rho}\,\bar{w}\,\hat{w}_y + 2\,\gamma\,\overline{\rho}\,\bar{w}\,\hat{w}_y\Big\}$$

$$+\frac{i\,\beta}{2(\gamma-1)}\Big\{2\,\gamma\,\hat{p}\,\bar{w} - 2\,\overline{\rho}\,\bar{u}\,\hat{u}\,\bar{w} + 2\,\gamma\,\overline{\rho}\,\bar{u}\,\hat{u}\,\bar{w} - 2\,\overline{\rho}\,\bar{v}\,\hat{v}\,\bar{w}$$

$$+2\,\gamma\,\overline{\rho}\,\bar{v}\,\hat{v}\,\bar{w} + (-1+\gamma)\,\hat{\rho}\,\bar{w}\,\left(\bar{u}^2 + \bar{v}^2 + \bar{w}^2\right)$$

$$+2\,\gamma\,\bar{p}\,\hat{w} - \overline{\rho}\,\bar{u}^2\,\hat{w} + \gamma\,\overline{\rho}\,\bar{u}^2\,\hat{w} - \overline{\rho}\,\bar{v}^2\,\hat{w}$$

$$+\gamma\,\overline{\rho}\,\bar{v}^2\,\hat{w} - 3\,\overline{\rho}\,\bar{w}^2\,\hat{w} + 3\,\gamma\,\overline{\rho}\,\bar{w}^2\,\hat{w}\Big\}$$

$$-\frac{1}{(\gamma-1)M^2\,Pr\,Re}\Big\{\hat{\mu}_x\,\overline{T}_x + \overline{\mu}_x\,\hat{T}_x + \hat{\mu}\,\overline{T}_{xx} + \overline{\mu}\,\hat{T}_{xx}$$

$$\hat{\mu}_y\,\overline{T}_y + \overline{\mu}_y\,\hat{T}_y + \hat{\mu}\,\overline{T}_{yy} + \overline{\mu}\,\hat{T}_{yy}\Big\}$$

$$+\frac{\beta^2\,\overline{\mu}\,\hat{T}}{(\gamma-1)M^2\,Pr\,Re}$$

$$+\frac{1}{3\,Re}\Big\{\,+3\,\hat{v}\,\bar{u}_y\,\overline{\mu}_x + 3\,\bar{v}\,\hat{u}_y\,\overline{\mu}_x + 3\,\bar{v}\,\bar{u}_y\,\hat{\mu}_x - 2\,i\,\beta\,\overline{\mu}\,\hat{w}\,\bar{u}_x - 2\,\hat{\mu}\,\bar{v}_y\,\bar{u}_x$$

$$-2\,\overline{\mu}\,\hat{v}_y\,\bar{u}_x + 4\,\hat{\mu}\,\bar{u}_x^2 + 3\,i\,\beta\,\overline{\mu}\,\bar{w}\,\hat{u}_x - 2\,\overline{\mu}\,\bar{v}_y\,\hat{u}_x + 8\,\overline{\mu}\,\bar{u}_x\,\hat{u}_x$$

$$+3\,\hat{\mu}\,\bar{u}_y\,\bar{v}_x + 3\,\overline{\mu}\,\hat{u}_y\,\bar{v}_x + 3\,\hat{v}\,\overline{\mu}_x\,\bar{v}_x + 3\,\bar{v}\,\hat{\mu}_x\,\bar{v}_x + 3\,\hat{\mu}\,\bar{v}_x^2$$

$$+3\,\overline{\mu}\,\bar{u}_y\,\hat{v}_x + 3\,\bar{v}\,\overline{\mu}_x\,\hat{v}_x + 6\,\overline{\mu}\,\bar{v}_x\,\hat{v}_x + 3\,\hat{w}\,\overline{\mu}_x\,\bar{w}_x + 3\,\bar{w}\,\hat{\mu}_x\,\bar{w}_x$$

$$+3\,\hat{\mu}\,\bar{w}_x^2 + 3\,\bar{w}\,\overline{\mu}_x\,\hat{w}_x + 6\,\overline{\mu}\,\bar{w}_x\,\hat{w}_x + 3\,\hat{\mu}\,\bar{v}\,\bar{u}_{xy} + 3\,\overline{\mu}\,\hat{v}\,\bar{u}_{xy}$$

$$+3\,\overline{\mu}\,\bar{v}\,\hat{u}_{xy} + 3\,\hat{\mu}\,\bar{v}\,\bar{v}_{xx} + 3\,\overline{\mu}\,\hat{v}\,\bar{v}_{xx} + 3\,\overline{\mu}\,\bar{v}\,\hat{v}_{xx} + 3\,\hat{\mu}\,\bar{w}\,\bar{w}_{xx}$$

$$+3\,\overline{\mu}\,\hat{w}\,\bar{w}_{xx} + 3\,\overline{\mu}\,\bar{w}\,\hat{w}_{xx} + 3\,\hat{u}\,\overline{\mu}_y\,\bar{u}_y + 3\,\bar{u}\,\hat{\mu}_y\,\bar{u}_y + 3\,\hat{\mu}\,\bar{u}_y^2$$

$$+3\,\bar{u}\,\overline{\mu}_y\,\hat{u}_y + 6\,\overline{\mu}\,\bar{u}_y\,\hat{u}_y - 2\,i\,\beta\,\overline{\mu}\,\hat{w}\,\bar{v}_y + 4\,\hat{\mu}\,\bar{v}_y^2 + 3\,i\,\beta\,\overline{\mu}\,\bar{w}\,\hat{v}_y$$

$$+8\,\overline{\mu}\,\bar{v}_y\,\hat{v}_y + 3\,\hat{w}\,\overline{\mu}_y\,\bar{w}_y + 3\,\bar{w}\,\hat{\mu}_y\,\bar{w}_y + 3\,\hat{\mu}\,\bar{w}_y^2 + 3\,\bar{w}\,\overline{\mu}_y\,\hat{w}_y$$

$$+6\,\overline{\mu}\,\bar{w}_y\,\hat{w}_y + 3\,\hat{\mu}\,\bar{u}\,\bar{u}_{yy} + 3\,\overline{\mu}\,\hat{u}\,\bar{u}_{yy} + 3\,\overline{\mu}\,\bar{u}\,\hat{u}_{yy} + 3\,\hat{\mu}\,\bar{w}\,\bar{w}_{yy}$$

$$+3\,\overline{\mu}\,\hat{w}\,\bar{w}_{yy} + 3\,\overline{\mu}\,\bar{w}\,\hat{w}_{yy} - 2\,\hat{\mu}\,\bar{v}_y\,\bar{u}_x - 2\,\overline{\mu}\,\hat{v}_y\,\bar{u}_x - 2\,\overline{\mu}\,\bar{v}_y\,\hat{u}_x$$

$$+3\,\hat{u}\,\overline{\mu}_y\,\bar{v}_x + 3\,\bar{u}\,\hat{\mu}_y\,\bar{v}_x + 3\,\hat{\mu}\,\bar{u}_y\,\bar{v}_x + 3\,\overline{\mu}\,\hat{u}_y\,\bar{v}_x + 3\,\bar{u}\,\overline{\mu}_y\,\hat{v}_x$$

$$+3\,\overline{\mu}\,\bar{u}_y\,\hat{v}_x + 3\,\hat{\mu}\,\bar{u}\,\bar{v}_{xy} + 3\,\overline{\mu}\,\hat{u}\,\bar{v}_{xy} + 3\,\overline{\mu}\,\bar{u}\,\hat{v}_{xy}\Big\}$$

$$+\frac{\hat{u}}{3\,Re}\Big\{3\,i\,\beta\,\bar{w}\,\overline{\mu}_x - 2\,\bar{v}_y\,\overline{\mu}_x + 4\,\overline{\mu}_x\,\bar{u}_x + 3\,i\,\beta\,\overline{\mu}\,\bar{w}_x - 2\,\overline{\mu}\,\bar{v}_{xy} + 4\,\overline{\mu}\,\bar{u}_{xx}\Big\}$$

$$+\frac{\bar{u}}{3\,Re}\Big\{-2\,i\,\beta\,\hat{w}\,\overline{\mu}_x - 2\,\hat{v}_y\,\overline{\mu}_x - 2\,\bar{v}_y\,\hat{\mu}_x + 4\,\hat{\mu}_x\,\bar{u}_x + 4\,\overline{\mu}_x\,\hat{u}_x$$

$$-2\,i\,\beta\,\overline{\mu}\,\hat{w}_x - 2\,\hat{\mu}\,\bar{v}_{xy} - 2\,\overline{\mu}\,\hat{v}_{xy} + 4\,\hat{\mu}\,\bar{u}_{xx} + 4\,\overline{\mu}\,\hat{u}_{xx}\Big\}$$

$$+\frac{\hat{v}}{3\,Re}\Big\{3\,i\,\beta\,\bar{w}\,\overline{\mu}_y + 4\,\overline{\mu}_y\,\bar{v}_y + 3\,i\,\beta\,\overline{\mu}\,\bar{w}_y + 4\,\overline{\mu}\,\bar{v}_{yy} - 2\,\overline{\mu}_y\,\bar{u}_x - 2\,\overline{\mu}\,\bar{u}_{xy}\Big\}$$

$$+\frac{\bar{v}}{3\,Re}\Big\{-2\,i\,\beta\,\hat{w}\,\overline{\mu}_y + 4\,\hat{\mu}_y\,\bar{v}_y + 4\,\overline{\mu}_y\,\hat{v}_y - 2\,i\,\beta\,\overline{\mu}\,\hat{w}_y + 4\,\hat{\mu}\,\bar{v}_{yy}$$

$$+4\,\overline{\mu}\,\hat{v}_{yy} - 2\,\hat{\mu}_y\,\bar{u}_x - 2\,\overline{\mu}_y\,\hat{u}_x - 2\,\hat{\mu}\,\bar{u}_{xy} - 2\,\overline{\mu}\,\hat{u}_{xy}\Big\}$$

$$-\frac{-i\,\hat{\mu}\,\beta}{3\,Re}\Big\{2\,\bar{w}\,(\bar{v}_y+\bar{u}_x)-3\,(\bar{v}\,\bar{w}_y+\bar{u}\,\bar{w}_x)\Big\}$$

$$-\frac{\overline{\mu}\,\beta}{3\,Re}\Big\{3\,\beta\,\bar{v}\,\hat{v}+4\,\beta\,\bar{w}\,\hat{w}+2\,i\,\hat{w}\,\bar{v}_y+2\,i\,\bar{w}\,\hat{v}_y-3\,i\,\hat{v}\,\bar{w}_y$$

$$-\,3\,i\,\bar{v}\,\hat{w}_y+2\,i\,\hat{w}\,\bar{u}_x+2\,i\,\bar{w}\,\hat{u}_x-3\,i\,\hat{u}\,\bar{w}_x+3\,\bar{u}\,(\beta\,\hat{u}-i\,\hat{w}_x)\Big\}=0 \qquad (2.23)$$

These equations may be recast as follows. First, in line with analogous practice of classic linear theory, viscosity is taken to be a function of temperature only. A law $\mu = \mu(T)$ is considered to relate the two quantities, taking viscosity in general to be a nonlinear function of temperature. A Taylor expansion about the basic state

$$\mu = \mu(\bar{T} + \varepsilon\hat{T}) \approx \mu(\bar{T}) + \varepsilon\frac{\partial\mu}{\partial\bar{T}}\hat{T} + O(\varepsilon^2) \tag{2.24}$$

may then be used to identify the basic state viscosity and relate that of the disturbance field to the disturbance temperature $\hat{T}$ through

$$\hat{\mu} = \frac{\partial\mu}{\partial T}\hat{T}. \tag{2.25}$$

Equation (2.25) may be used to eliminate $\hat{\mu}$ from the system (2.19-2.23) in favour of the disturbance temperature. The latter is related with the respective disturbance pressure and density of the medium through

$$\gamma M^2\hat{p} = \bar{\rho}\hat{T} + \bar{T}\hat{\rho}, \tag{2.26}$$

which may be used to eliminate one of $\hat{p}, \hat{\rho}, \hat{T}$ and cast the final system to be solved in terms of five two-dimensional disturbance amplitude functions, the three velocity components and two thermodynamic variables. Once a solution of the eigenvalue problem is known (2.26) may be used to calculate the eliminated third thermodynamic disturbance quantity.

(*a*) *Challenges and potential simplifications of the compressible two-dimensional eigenvalue problem*

The challenges associated with a numerical solution of the system (2.19-2.23) can be classified into two categories. One is related with issues analogous with those of the incompressible two-dimensional eigenvalue problem [26] and stems from the simultaneous resolution of two spatial directions, in this case the problem being aggravated by the existence of an additional constitutive equation to be solved. In addition, the system to be solved becomes increasingly stiff with increasing Reynolds number; note that the diagonal dominance of the matrix decreases linearly with *Re*. This leads to the need for simplifications, which will be discussed in what follows. The second class of challenges is raised by compressibility. From a numerical point of view mixed derivatives of both the basic flow and the disturbance quantities appear, which couple the system stronger but are prone to propagating errors in the numerical discretisation in one spatial direction into the entire resolved plane. Cubic nonlinearities give rise to the need for finer discretisation of the compressible eigenvalue problem compared with its incompressible counterpart. An additional source of stiffness in the eigenvalue problem stems from the quadratically decreasing diagonal dominance of the system of equations with increasingly high supersonic and hypersonic Mach number. On the positive side, the issue of boundary conditions for the (elliptic) incompressible partial-derivative eigenvalue problem is absent in compressible flow, where pressure becomes a variable to be solved for as opposed to a constrain to be imposed.

In dealing with the issue of the size of the eigenvalue problem one notes that, unlike the incompressible eigenvalue problem where considering a wavenumber vector perpendicular to the plane on which the basic flow develops, i.e. setting $\bar{w} \equiv 0$, leads to the ability to recast the eigenvalue problem as one with real coefficients requiring approximately half the computing resources for its numerical solution compared with the original complex system, in compressible flow this simplification is not possible. This is so on account of density and viscosity variations which are absent in incompressible flow. Focussing on the application at hand, even if such a simplification were possible it would be physically meaningless, since the predominant flow direction on the elliptic cone coincides with that of the wavenumber vector. Using the same physical rationale for the development of the basic flow on the elliptic cone one may attempt to neglect the lateral and wall-normal velocity components, $\bar{u} \equiv \bar{v} \equiv 0$.

One radical simplification from a numerical point of view is offered by the inviscid limit of the equations of motion, $Re \to \infty, M \to 0$, which removes both these sources of stiffness in the system to be solved. However, this resulting system is a coupled problem for five variables, say $(\rho, \hat{u}, \hat{v}, \hat{w}, \hat{T})^{\mathrm{T}}$. In this respect, the issue of size of the eigenvalue problem remains unresolved. Furthermore, an inviscid analysis introduces a major currently unresolved physical issue, that of the extension of the concept of a critical layer (introduced and unambiguously defined in the context of one-dimensional instability analysis) in two resolved spatial directions. A first step towards resolving the issue of critical layers in two spatial dimensions numerically is discussed in the next section.

(b) One inviscid limit

The only means by which an inviscid analysis could be performed at a lower numerical effort compared with the various forms of the original problem is the case

$$\bar{u} = \bar{v} = 0, \ \bar{w} \neq 0, \qquad (2.27)$$

which results in the compressible generalisation of the Rayleigh equation [25]

$$\mathcal{L}\hat{p} + \left[\left(\frac{\bar{p}_x}{\gamma \bar{p}} - \frac{\overline{\rho}_x}{\overline{\rho}} \right) - \frac{2\beta \bar{w}_x}{(\beta \bar{w} - \omega)} \right] \hat{p}_x + \left[\left(\frac{\bar{p}_y}{\gamma \bar{p}} - \frac{\overline{\rho}_y}{\overline{\rho}} \right) - \frac{2\beta \bar{w}_y}{(\beta \bar{w} - \omega)} \right] \hat{p}_y + \left[\frac{\overline{\rho} \left(\beta \bar{w} - \omega \right)^2}{\gamma \bar{p}} \right] \hat{p} = 0, \quad (2.28)$$

where $\mathcal{L} \equiv \partial/\partial x^2 + \partial/\partial y^2 - \beta^2$. This most simple form in which the compressible two-dimensional eigenvalue problem may be recast can be solved as a cubic equation for either a complex temporal eigenvalue ω, taking β to be a constant real wavenumber parameter in the z spatial direction, or for the complex spatial eigenvalue β, taking the frequency parameter ω to be a real constant. Notably there is no overhead when solving the spatial compared with the temporal two-dimensional eigenvalue problem (2.28).

From a physical point of view the implication of addressing (2.28) as opposed to (2.19-2.23) is that the three-dimensional elliptic cone geometry is reduced to a three-dimensional elliptic cylinder geometry which is periodic in the third direction with a periodicity length $L_z = 2\pi/\beta$. The analysis may be performed at a $z = z_0 = const.$ location along the axis of rotation of the cone taking, of course, as a basic flow an extract from the correct three-dimensional basic steady state already calculated. Having performed the analysis, one needs to compare the wavelength of any globally unstable mode predicted with the lengthscale of the neglected three-dimensionality of the elliptic cone surface downstream of the location $z = z_0$. If the first length scale is much smaller than the second, the predicted instability may be physically realisable. Otherwise, either or both of the approximations (2.27) and an inviscid analysis must be abandoned in favour of viscous analysis based on numerical solution of the full system (2.19-2.23). At this point in time, which of the two scenarios will prevail is unclear; the potential savings realised by the inviscid approach make the latter the obvious candidate to commence global instability analyses on the elliptic cone. In the next chapter we develop the two-dimensional grid on which an inviscid global instability analysis may be performed and provide the elements forming the basis to derive the three-dimensional extension of the global eigenvalue problem for the application at hand.

3. On frames of reference on the elliptic cone

In the preceding discussion we justified interest in a global linear analysis based on the two-dimensional eigenvalue problem from the point of view of numerical feasibility. From a physical point of view this approach can be justified using one of the fundamental assumptions of boundary-layer theory, namely that the dependence of the basic flow quantities on the downstream direction (to be defined shortly in the context of the elliptic cone) is $O(1/Re)$ weaker than that on the wall-normal direction, Re denoting the free-stream Reynolds number of the flow. Experimentation and three-dimensional numerical solutions of the equations of motion for the basic flow have verified this assumption; this property is also to be found in the low angle-of-attack solutions of the Navier-Stokes equations presented in [25].

Regarding instability analyses information on three-dimensionality comes principally from experiments and direct numerical simulations on planar and axisymmetric geometries [17, 21]. One- and quasi two-dimensional linear and nonlinear instability analyses are performed at a particular location on the surface of the object examined. Homogeneity of space in the case of planar geometries and axisymmetry of the circular cone permit introduction of a harmonic decomposition of disturbances in the spanwise or circumferential direction, respectively. As has been mentioned, the dependence of the basic flow on the streamwise direction is neglected and a harmonic decomposition is introduced in this direction. The latter assumption is made also in the context of a global analysis based on the two-dimensional eigenvalue problem. As far as the downstream location is concerned, the arc-length defined along the generators and measured from the tip of the elliptic cone is the natural choice of coordinate along which the dependence of the basic flow can be neglected in comparison with that along the other two spatial directions. This choice is straightforward if the oncoming flow is at zero angle of attack; at increasingly large nonzero values of the angles of attack and yaw/bank the choice is less clear since the three-dimensionality of the flowfield is enhanced by nonzero values of the angle of attack; nevertheless, we adhere to the arc-length as the downstream coordinate in these cases also. As the case is with the one- and quasi two-dimensional analyses the wall-normal direction defines one essential spatial direction on which information is required for a global linear analysis. On the other hand, the definition of the third spatial direction on the elliptic cone is not unique.

(a) The elliptic confocal coordinate system

In anticipation of solving a two-dimensional global linear eigenvalue problem, in which on grounds of feasibility the dependence of the flow on the third direction is neglected, the natural choice of coordinate system to express the basic flow quantities and solve the eigenproblem is the confocal elliptic coordinate system $O\xi\eta$, schematically depicted in figure 1. A conformal transformation in the complex plane, discussed in detail in appendix A, relates the cartesian coordinate system Oxy to $O\xi\eta$ through

$$x = c \cosh\xi \cos\eta \qquad (3.1)$$
$$y = c \sinh\xi \sin\eta \qquad (3.2)$$

in two spatial dimensions, while the extension to three dimensions is trivial and leads to the well-known elliptic cylindrical coordinate system The inverse transformation is given by

$$\xi = \frac{1}{c}\,\mathrm{Re}\{\cosh^{-1}(x + iy)\}, \qquad (3.3)$$

$$\eta = \frac{1}{c}\,\mathrm{Im}\{\cosh^{-1}(x + iy)\}. \qquad (3.4)$$

The coordinate lines of this orthogonal system are confocal ellipses $\xi = cnst.$ and hyperbolae $\eta = cnst.$ with common foci at $x = \pm c = \pm\sqrt{a^2 - b^2}$. The semiaxes themselves are

$$a = c \cosh \xi, \tag{3.5}$$

$$b = c \sinh \xi, \tag{3.6}$$

which ensures satisfaction of the equation of the ellipse in cartesian coordinates. The semi-axes a and b and the focal distance c of the ellipse are used to define $\xi_w = cnst.$, the ellipse describing the wall of the elliptic cone at a particular location z_0, through

$$\xi_w = \frac{1}{2} \ln \frac{a+b}{a-b} = \ln \frac{a+b}{c}. \tag{3.7}$$

Chain rule for partial differentiation is used to relate derivatives in the two coordinate systems,

$$\left(\begin{array}{c} \partial f/\partial \xi \\ \partial f/\partial \eta \end{array} \right) = J \left(\begin{array}{c} \partial f/\partial x \\ \partial f/\partial y \end{array} \right). \tag{3.8}$$

The inverse Jacobian matrix of the transformation is

$$J^{-1} = \frac{c}{h^2} \left(\begin{array}{cc} \sinh \xi \cos \eta & -\cosh \xi \sin \eta \\ \cosh \xi \sin \eta & \sinh \xi \cos \eta \end{array} \right) = \frac{1}{h^2} \left(\begin{array}{cc} j_1 & -j_2 \\ j_2 & j_1 \end{array} \right), \tag{3.9}$$

where h is the metric of the transformation

$$h = h_\xi = h_\eta = c\sqrt{\sinh^2 \xi + \sin^2 \eta}. \tag{3.10}$$

The gradient and Laplacian operators, appearing in the two-dimensional eigenvalue problems, have the forms

$$\text{grad } f = (f_\xi/h, f_\eta/h) \tag{3.11}$$

and

$$\nabla^2 f = f_{\xi\xi}/h^2 + f_{\eta\eta}/h^2 \tag{3.12}$$

respectively.

Desirable properties of this coordinate system are its strong clustering of points in the neighbourhood of the wall, itself being a coordinate line, such that no numerically introduced discontinuities are to be expected. Indeed it has been known for some time [14] that when using high-order numerical methods for the approximation of a differential operator in the neighbourhood of a solid boundary care has to be taken that the boundary itself is approximated with the same degree of accuracy. Furthermore, this natural clustering at the wall is expected to be advantageous in resolving the boundary layer and its instabilities. In the far-field, the exponential decay of the density of the coordinate lines $\xi = cnst.$ as $\xi \to \infty$ permits taking the outflow boundary of the computational domain ξ_∞ well away from viscous regions and the only limitation in the choice of a value for ξ_∞ is expected to be the shock location.

The physical implication of an instability analysis based on the elliptic confocal coordinate system is that the three-dimensionality of the elliptic cone is locally neglected in the following sense. The basic flow is calculated by a three-dimensional steady scheme and may be extracted on an arbitrary two-dimensional grid. Using the elliptic confocal coordinate system one selects a particular location z_0 along the cone axis and extracts the three velocity components, density and pressure on a plane

normal to the axis Oz. The inverse transformation (3.3-3.4) permits describing the non-conservative variables on the $O\xi\eta$ coordinate system, while the discussion of this paragraph forms the basis for transforming any of the forms of the two-dimensional eigenvalue problem discussed in the previous section into the elliptic confocal coordinate system and solving it.

In so doing, one approximates the elliptic cone surface locally by an elliptic cylinder. Potentially unstable global eigenmodes to be delivered by the analysis will be characterised by a periodicity length $L_z = 2\pi/\beta$ corresponding to the most unstable wavenumber parameter β. A comparison of the wavelength of the most unstable global eigenmode with the length scale locally characterising the departure of the actual elliptic cone from the assumed elliptic cylinder, Δz. Essential for a meaningful global instability analysis from a physical point of view is the satisfaction of the condition

$$L_z \ll \Delta z \tag{3.13}$$

which implies that the neglected three-dimensionality of the elliptic cone does not affect locally the development of an unstable $z-$wise periodic global eigenmode.

On account of the underlying analytic conformal transformation, the elliptic confocal coordinate system is the simplest and most elegant means of performing a global instability analysis on the elliptic cone. However, this is not the only possible approach and in what follows we discuss briefly the building blocks of two different methodologies towards arriving at *three-dimensional* global instability analysis equations. In following this approach we intend to provide alternative three-dimensional coordinate systems, the coordinate lines of which are by construction mutually orthogonal. This is the case for the three-dimensional extension of the elliptic confocal coordinate system, namely the elliptic cylinder, but not for the elliptic cone. The following two paragraphs sketch two alternative approaches to arrive at consistent means of neglecting the third spatial direction, while retaining the three-dimensionality of the elliptic cone surface. The resulting two-dimensional surfaces are expected to be different than the plane defined by the cone base on which the elliptic confocal coordinate system has been discussed. As a consequence performance of global instability analyses on such three-dimensional surfaces would require an extension of the approach based on (2.1). Such an extension will be considered in future efforts. Ultimately, comparisons of the global instability analysis results on the two different two-dimensional planes could embed the known physical mechanisms into a 2 framework and shed light at potentially existing additional physical mechanisms that cannot be captured by the simple one-dimensional linear theory.

(b) A body-fitted three-dimensional coordinate system

Tensor analysis may be used to arrive at a general three-dimensional body-fitted system to describe the equations of motion. In this case a transformation between a given cartesian frame of reference $O(x, y, z)^{\mathrm{T}}$ and an orthogonal body-fitted coordinate system $O(\xi, \eta, \theta)^{\mathrm{T}}$, in which ξ denotes the coordinate from the elliptic cone tip along the cone surface, η denotes the wall-normal and θ the angle between the cone axis of symmetry and the line $O\xi$, can be constructed by simple trigonometric relationships. On the plane $x = x_0 = 0$, schematically presented in figure 2,

$$x_0 = 0, \tag{3.14}$$

$$y_0 = y_1 + y_2 = (\xi - \Delta\xi)\sin\theta + \frac{\eta}{\cos\theta} = (\xi - \eta\tan\theta)\sin\theta + \frac{\eta}{\cos\theta}, \tag{3.15}$$

$$\tag{3.16}$$

where the elliptic cone semiangle θ is in general a function of the angle ϕ, shown in figure 3. The equation of the ellipse, expressed in terms of its eccentricity $\epsilon = c/a$ and the parameter $\kappa = b^2/a$, a and b being the semiaxes of the ellipse, is

$$R(\phi) = \frac{\kappa}{1 + \epsilon \cos \phi}.$$ (3.17)

In three-dimensional space, ξ, θ and R are functions of the angle ϕ, as shown in figure 4. Simple trigonometrical relations permit solving for the independent variable

$$\theta(\phi) = \arctan \left[\frac{1}{L} \frac{\kappa}{(1 + \epsilon \cos \phi)} \right].$$ (3.18)

Combining (3.17) and (3.18) it follows that

$$\xi(\phi) = \sqrt{L^2 + \left(\frac{\kappa}{(1 + \epsilon \cos \phi)} \right)^2},$$ (3.19)

such that the body-fitted coordinate system $O(\xi, \eta, \theta)^{\mathrm{T}}$ is related with the cartesian system $Oxyz$ through

$$x = \left(\left[\xi - \eta \tan \theta \right] \sin \theta + \frac{\eta}{\cos \theta} \right) \cos \phi,$$ (3.20)

$$y = \left(\left[\xi - \eta \tan \theta \right] \sin \theta + \frac{\eta}{\cos \theta} \right) \sin \phi,$$ (3.21)

$$z = (\xi - \eta \tan \theta) \cos \theta.$$ (3.22)

The objective now becomes to express the three-dimensional compressible continuity, Navier-Stokes and energy equations in the body-fitted coordinate system. This is currently pursued, however at lower priority compared with the current main focus, which is to obtain two-dimensional eigenvalue problem results on the two-dimensional elliptic confocal coordinate system introduced in the previous section.

(c) *Differential geometry concepts for the derivation of the instability equations*

In this section we follow an alternative little known methodology in order to arrive at the desired two-dimensional global stability equations as the limit of those expressed in a three-dimensional body-fitted coordinate system. Ultimately, the present approach and that of the previous section should yield identical results. In view of the non-trivial nature of the systems of equations in question, following two alternative methodologies is useful in cross-verifying the results of the respective derivations.

An essential property of the geometry in question, introduced by the departure of the elliptic cone from axisymmetry, is the non-orthogonality of the azimuthal direction and the plane defined by the arc-length and wall-normal directions. This is illustrated by the introduction of a body-fitted coordinate system† defined by the arc-length coordinate s, the wall-normal coordinate n and a coordinate θ normal to the plane Osn. This system is shown in the upper part of figure 5; also shown is the azimuthal coordinate ϕ, which is normal to the Oyz plane. Along the (s, n, θ) directions we introduce unit vectors $\mathbf{e}_s, \mathbf{e}_n, \mathbf{e}_\theta$ and $\mathbf{e}_\phi$. The Cartesian frame of reference (x, y, z) on which the basic flow calculations have been performed in [25] and the newly introduced frames of reference are related by

$$x = \cos \phi(sa + nbL),$$ (3.23)
$$y = \sin \phi(sb + naL),$$ (3.24)
$$z = sL - nab.$$ (3.25)

---

† in general different than that of the previous section - different notation underlines this point

The unit vectors along the (s, n, θ) directions are

$$\mathbf{e}_s = \frac{1}{\sqrt{S}} \begin{pmatrix} a\cos\phi \\ b\sin\phi \\ L \end{pmatrix},$$

(3.26)

$$\mathbf{e}_n = \frac{1}{\sqrt{N}} \begin{pmatrix} Lb\cos\phi \\ La\sin\phi \\ -ab \end{pmatrix},$$

(3.27)

$$\mathbf{e}_\theta = \frac{1}{\sqrt{\Theta}} \begin{pmatrix} a[b^2 + L^2]\sin\phi \\ -b[a^2 + L^2]\cos\phi \\ L[b^2 - a^2]\sin\phi\cos\phi \end{pmatrix},$$

(3.28)

where

$$S = a^2\cos^2\phi + b^2\sin^2\phi + L^2,$$
$$N = L^2b^2\cos^2\phi + L^2a^2\sin^2\phi + a^2b^2,$$
$$\Theta = a^2(b^2 + L^2)^2\sin^2\phi + b^2(a^2 + L^2)^2\cos^2\phi + L^2(b^2 - a^2)^2\sin^2\phi\cos^2\phi,$$

while the unit vector in the $O\phi$ direction is

$$\mathbf{e}_\phi = \frac{1}{\sqrt{a^2\sin^2\phi + b^2\cos^2\phi}} \begin{pmatrix} a\sin\phi \\ -b\cos\phi \\ 0 \end{pmatrix}.$$

(3.29)

In the limit case $a = b = r$, which corresponds to a cone with circular base of radius r, $\phi \equiv \theta$ and $\mathbf{e}_\phi = \mathbf{e}_\theta$. However, if $a \neq b$ the third component of $\mathbf{e}_\theta$ is nonzero and $\mathbf{e}_\theta$ defines the tangent vector along the $2\pi-$periodic line $L[b^2 - a^2]\sin\phi\cos\phi$. Also, $\mathbf{e}_\theta$ is by construction tangent to the line $s = cnst.$ on which the elliptic cone is shown to terminate in the lower left part of figure 5 and to the wall-normal direction. In this case $\mathbf{e}_\phi \cdot \mathbf{e}_\theta \neq 0$, a fact which has far-reaching consequences for the global instability analysis in terms of the definition of the plane on which the global analysis will be performed and hence we elaborate on the coordinate systems defined further.

The two coordinate systems $(\mathbf{e}_s, \mathbf{e}_n, \mathbf{e}_\phi)$ and $(\mathbf{e}_s, \mathbf{e}_n, \mathbf{e}_\theta)$ have the following properties. Both reference systems have in common a local origin which is placed as the same distance from the cone tip, a property which may be interesting in the subsequent analysis if we wish to describe the three-dimensionality of the flow in terms of its impact on local instability properties. Specifically, local linear analyses could be performed by monitoring the flow at equidistant locations from the tip of the elliptic cone and resolving the wall-normal direction and the results could be compared with those of global analyses in which the $s = cnst.$ line defines one resolved spatial direction. The second common property of the two coordinate systems is that they encompass one direction normal to the elliptic cone surface; this is an essential characteristic independently of the type of global or local instability analysis to be performed. The discriminating characteristic of the two coordinate systems is that $(\mathbf{e}_s, \mathbf{e}_n, \mathbf{e}_\phi)$ is non-orthogonal by contrast to $(\mathbf{e}_s, \mathbf{e}_n, \mathbf{e}_\theta)$ which is orthonormal. While the last characteristic is appealing in the derivation of the global instability equations on the $On\theta$ plane, use of the $(\mathbf{e}_s, \mathbf{e}_n, \mathbf{e}_\phi)$ coordinate system could be advantageous in facilitating comparisons with experiment in which a light sheet is used to visualise instabilities on the $On\phi$ plane [12].

A third coordinate system may also be introduced along the following lines. The arc-length direction Os and its unit vector $\mathbf{e}_s$ as well as the *local* wall-normal direction On and its unit vector $\mathbf{e}_n$ are introduced as before. The third coordinate direction is defined in this coordinate system *numerically* by reference to the basic flow data of Theofilis [25]. The three-dimensional flowfields could be post-processed to recover the magnitude and direction of the flow perpendicular to the Ons plane, which we loosely refer to as the *crossflow* direction. The third coordinate could then be defined by the

requirement

$$\text{crossflow magnitude} = cnst. \tag{3.30}$$

This introduces a different direction $O\vartheta$, termed the crossflow direction, along which a tangent vector $\mathbf{e}_\vartheta$ could be defined numerically. The global linear analysis can the be performed on any of the three coordinate systems $(\mathbf{e}_s, \mathbf{e}_n, \mathbf{e}_\phi)$, $(\mathbf{e}_s, \mathbf{e}_n, \mathbf{e}_\theta)$ or $(\mathbf{e}_s, \mathbf{e}_n, \mathbf{e}_\vartheta)$ by resolving, respectively, the planes $On\phi$, $On\theta$ or $On\vartheta$. The advantage of performing the analysis on the $On\vartheta$ plane would be that the effects of wall-normal and crossflow direction on flow instability would be separated in the the global analysis.

The benefit of choosing any of the three coordinate systems to perform the global instability calculations could be assessed by reference to experiment. However, the form of the equations of motion is obviously affected by choosing different coordinate systems and the nontrivial nature of the derivations of the three-dimensional compressible equations of motion in arbitrary coordinate systems warrants a decision at this stage on the reference system to be used in the subsequent analysis. As an example, we use Appendix C to demonstrate derivation of the gradient operator using a little-known methodology of differential geometry[11, 3], which delivers transformation of equations in *arbitrary* coordinate systems including those defined numerically, such as the $(\mathbf{e}_s, \mathbf{e}_n, \mathbf{e}_\vartheta)$ frame of reference, *without* having to resort to tensor analysis. The result in the $(\mathbf{e}_s, \mathbf{e}_n, \mathbf{e}_\theta)$ coordinate system is

$$df = \frac{1}{\omega_s^s}\frac{\partial f}{\partial s}\tilde{\omega}^s + \left[\frac{1}{\omega_\phi^\theta} - \frac{\omega_\phi^s}{\omega_s^s\omega_\phi^\theta} - \frac{\omega_\phi^n}{\omega_n^n\omega_\phi^\theta}\right]\frac{\partial f}{\partial\theta}\tilde{\omega}^\theta + \frac{1}{\omega_n^n}\frac{\partial f}{\partial n}\tilde{\omega}^n. \tag{3.31}$$

with the shorthand notation explained in Appendix C. The differential geometry concepts are useful in providing alternative ways of deriving the three-dimensional compressible Navier-Stokes equations in general three-dimensional frames of reference, the only requirement for which is that they be orthogonal at each point in space. In view of the relative simplicity of the three-dimensional shape of an elliptic cone surface, which will form the basis for the derivation of an body-fitted frame of reference, we turn to deriving the equations of motion using classic tensor analysis and will return to differential geometry in order to cross-validate the results of the anticipated extensive calculations.

4. The numerical solution of the generalised Rayleigh equation

In view of the transformation (3.1-3.2) the generalised Rayleigh equation (2.28) becomes on the elliptic confocal coordinate system

$$
\hat{p}_{\xi\xi} + \hat{p}_{\eta\eta} - h^2\beta^2\hat{p} + \frac{j_1^2 + j_2^2}{h^2}\left[\left(\frac{\bar{p}_\xi}{\gamma\bar{p}} - \frac{\overline{\rho}_\xi}{\overline{\rho}}\right) - \frac{2\beta\bar{w}_\xi}{(\beta\bar{w} - \omega)}\right]\hat{p}_\xi
$$
$$
+ \frac{j_1^2 + j_2^2}{h^2}\left[\left(\frac{\bar{p}_\eta}{\gamma\bar{p}} - \frac{\overline{\rho}_\eta}{\overline{\rho}}\right) - \frac{2\beta\bar{w}_\eta}{(\beta\bar{w} - \omega)}\right]\hat{p}_\eta
$$
$$
+ \left[\frac{\overline{\rho}\,(\beta\bar{w} - \omega)^2}{\gamma\bar{p}}\right]\hat{p} = 0. \tag{4.1}
$$

However, $j_1^2 + j_2^2 = h^2$, such that one finally has to solve

$$
\mathcal{M}\hat{p} + \left[\left(\frac{\bar{p}_\xi}{\gamma\bar{p}} - \frac{\overline{\rho}_\xi}{\overline{\rho}}\right) - \frac{2\beta\bar{w}_\xi}{(\beta\bar{w} - \omega)}\right]\hat{p}_\xi + \left[\left(\frac{\bar{p}_\eta}{\gamma\bar{p}} - \frac{\overline{\rho}_\eta}{\overline{\rho}}\right) - \frac{2\beta\bar{w}_\eta}{(\beta\bar{w} - \omega)}\right]\hat{p}_\eta + \left[\frac{\overline{\rho}\,(\beta\bar{w} - \omega)^2}{\gamma\bar{p}}\right]\hat{p} = 0. \tag{4.2}
$$

where the linear operator $\mathcal{M} \equiv \partial_{\xi\xi} + \partial_{\eta\eta} - h^2\beta^2$. In a manner analogous with classic one-dimensional linear theory, (4.2) may be solved either iteratively or by direct means. In view of the lack of any prior physical insight into global linear disturbances in the application at hand, a direct method is preferable on account of the access to the full eigenvalue spectrum that it provides.

Either the temporal or the spatial form of the eigenvalue problem may be solved at the same level of numerical effort using a direct method since, in both cases, a cubic eigenvalue problem must be solved. In its temporal form, this is

$$
T_1\,\hat{p}_{\xi\xi} + T_2\,\hat{p}_{\eta\eta} + T_3\,\hat{p}_\xi + T_4\,\hat{p}_\eta + T_5\,\hat{p} = \omega\,(T_6\,\hat{p}_{\xi\xi} + T_7\,\hat{p}_{\eta\eta} + T_8\,\hat{p}_\xi + T_9\,\hat{p}_\eta + T_{10}\,\hat{p})
$$
$$
+ \omega^2\,T_{11}\,\hat{p}
$$
$$
+ \omega^3\,T_{12}\,\hat{p} \tag{4.3}
$$

while the spatial generalised Rayleigh equation on the elliptic confocal coordinate system is

$$
S_1\,\hat{p}_{\xi\xi} + S_2\,\hat{p}_{\eta\eta} + S_3\,\hat{p}_\xi + S_4\,\hat{p}_\eta + S_5\,\hat{p} = \beta\,(S_6\,\hat{p}_{\xi\xi} + S_7\,\hat{p}_{\eta\eta} + S_8\,\hat{p}_\xi + S_9\,\hat{p}_\eta + S_{10}\,\hat{p})
$$
$$
+ \beta^2\,S_{11}\,\hat{p}
$$
$$
+ \beta^3\,S_{12}\,\hat{p} \tag{4.4}
$$

The coefficients appearing in (4.3-4.4) are given in appendix B.

(a) Spectral collocation for the inviscid instability problem

Either of the systems (4.3) or (4.4) may be discretised by spectral collocation means. The natural choices for basis functions are a member of the Jacobi family of polynomials; here Chebyshev polynomials have been chosen to discretise the $\xi-$ spatial direction [4]. The natural boundary of the elliptic cone surface dictates the need for a mapping of the standard Chebyshev domain $x_j = \cos j\pi/N_\xi$ onto ξ through

$$
\xi_j = \frac{1}{2}\,x_j\,(\xi_w - \xi_\infty) + \frac{1}{2}\,(\xi_w - \xi_\infty), \qquad j = 0, \cdots, N_\xi \tag{4.5}
$$

where ξ_w is given by (3.7) and ξ_∞ represents the far-field location along the ξ coordinate where the domain is truncated. Chain rule is used to account for the metric of the transformation between x_j and ξ_j analytically and arrive at the expression for the collocation derivative matrices, $\mathcal{D}_\xi$, for the first and $\mathcal{D}_{\xi\xi}$ for the second derivative in the $\xi-$direction in terms of their standard Chebyshev counterparts $\mathcal{D}_c$ and $\mathcal{D}_c^2$,

$$\mathcal{D}_\xi = \frac{2}{(\xi_w - \xi_\infty)}\mathcal{D}_c, \tag{4.6}$$

$$\mathcal{D}_{\xi\xi} = \frac{4}{(\xi_w - \xi_\infty)^2}\mathcal{D}_c^2. \tag{4.7}$$

A Fourier expansion is used to discretise the $2\pi-$periodic spatial direction η. Here no mapping is necessary and one may use the standard Fourier points,

$$\eta_j = 2\,j\,\pi\,/N_\eta, \qquad\qquad j = 0, \cdots, N_\eta - 1 \tag{4.8}$$

and the the first two associated Fourier collocation derivative matrices $\mathcal{D}_f$ and $\mathcal{D}_f^2$ to perform differentiation along η,

$$\mathcal{D}_\eta = \mathcal{D}_f, \tag{4.9}$$

$$\mathcal{D}_{\eta\eta} = \mathcal{D}_f^2. \tag{4.10}$$

The generalised Rayleigh equation may now be discretised in elliptic confocal coordinate space to arrive at its temporal

$$\begin{aligned}
\{T_1\,\mathcal{D}_{\xi\xi} + T_2\,\mathcal{D}_{\eta\eta} + T_3\,\mathcal{D}_\xi + T_4\,\mathcal{D}_\eta + T_5\,I\}\,\hat{p} &= \omega\,\{T_6\,\mathcal{D}_{\xi\xi} + T_7\,\mathcal{D}_{\eta\eta} + T_8\,\mathcal{D}_\xi + T_9\,\mathcal{D}_\eta + T_{10}\,I\} \\
&+ \omega^2\,T_{11}\,I\,\hat{p} \\
&+ \omega^3\,T_{12}\,I\,\hat{p}
\end{aligned} \tag{4.11}$$

or spatial form

$$\begin{aligned}
\{S_1\,\mathcal{D}_{\xi\xi} + S_2\,\mathcal{D}_{\eta\eta} + S_3\,\mathcal{D}_\xi + S_4\,\mathcal{D}_\eta + S_5\,I\}\,\hat{p} &= \beta\,\{S_6\,\mathcal{D}_{\xi\xi} + S_7\,\mathcal{D}_{\eta\eta} + S_8\,\mathcal{D}_\xi + S_9\,\mathcal{D}_\eta + S_{10}\,I\} \\
&+ \beta^2\,S_{11}\,I\,\hat{p} \\
&+ \beta^3\,S_{12}\,I\,\hat{p}
\end{aligned} \tag{4.12}$$

which may be readily collocated.

However, before either equation can be solved, the issue of critical layer in two spatial dimensions arises, which must be resolved. In the next chapter we provide one solution based on the idea of complex collocation calculation grids. This is extending spectral collocation grids of the type (4.5) and (4.8) into complex space, where the calculations are performed; the physical quantities of interest are extracted as the real part of the results obtained. For simplicity of the demonstration and in view of the abundance of comparison data existing we adhere to the classic one-dimensional compressible linear stability eigenvalue problem.

5. On complex spectral collocation grids for inviscid instability analysis

In anticipation of an inviscid global analysis to follow, we discuss here the development of a new methodology based on spectral collocation methods to address this issue. While (real-grid) spectral methods have long been applied to the solution of the basic flow problem [20] their application to the resultant inviscid instability analysis has proved prohibitive due to the existence of the critical layers. Two solutions exist in order to regain spectral accuracy. The first is to use a standard Chebyshev Gauss-Lobatto (real) grid [4] but Taylor-expand the basic flow around the critical layer. The second, followed herein, is to extend the Zaat-Mack technique for the integration of the instability equations in the complex plane and introduce complex collocation grids, forcing a spectral method to integrate the equations on a complex contour suitably adapted to avoid the critical layer. Use of this second approach was first suggested by Boyd and Christidis [2] and further investigated by Boyd [1] in the context of atmospheric and hydrodynamic instability calculations. These works were extended by Gill and Sneddon [10], who gave an analytic formula for optimizing one family of complex (quadratic) maps.

Here we validate the key element of an inviscid global linear instability analysis, namely complex spectral collocation calculation grids, by introducing a novel spectral scheme for the solution of the one-dimensional incompressible inviscid linear eigenvalue problem in planar geometries and that pertaining to supersonic flow in both planar and curved geometries. The first problem is governed by the classic Rayleigh equation while compressibility and curvature are discussed using the equations of Duck [8] or their planar limits. We employ complex spectral collocation grid techniques first to the solution of the basic flow problem and subsequently to both the incompressible and the compressible inviscid linear eigenvalue problems. The accuracy and the efficiency of the proposed algorithms are assessed in comprehensive comparisons of results obtained using our spectral approach against the work of Mack [17, 18] and the finite–difference algorithm of Duck [8].

(a) Linear local inviscid instability theoretical background

With reference to the conical geometry presented by [9], introduction of the local theory Ansatz into the full Navier-Stokes, energy and continuity equations results in a sixth-order system for the linear disturbance amplitude functions; further, if one takes the $O(\varepsilon \ll 1)$-terms with the leading order in Reynolds number (i.e., ignoring viscous terms), the sixth-order system can be reduced to

$$\varphi_\eta + \frac{\zeta}{1 + \lambda\zeta^2 + \zeta\eta}\varphi - \frac{W_{0\eta}\varphi}{W_0 - \beta} = \frac{i\tilde{p}}{\gamma M_\infty^2 (W_0 - \beta)}\left\{T_0\left[1 + \frac{n^2\zeta^2}{\alpha^2(1 + \lambda\zeta^2 + \zeta\eta)^2}\right] - M_\infty^2(W_0 - \beta)^2\right\},$$

$$\tag{5.1}$$

$$i\alpha^2(W_0 - \beta)\frac{\varphi}{T_0} = -\frac{\tilde{p}_\eta}{\gamma M_\infty^2},\tag{5.2}$$

in the independent variable η, where W_0 and T_0 are respectively the single basic flow velocity component and basic flow temperature profiles, $\lambda = 0$ corresponds to a cylinder and $\lambda \neq 0$ generates families of conical geometries, ζ is the scaled downstream coordinate, $\varphi = \tilde{v}_1/\zeta$ and $\tilde{p}$ are the scaled disturbance velocity component and disturbance pressure amplitude functions, M_∞ is the free-stream Mach number, γ is the ratio of specific heats, $n \neq 0$ corresponds to non-axisymmetric disturbances, $\alpha = \overline{\alpha}\zeta$, $\omega = \overline{\omega}\zeta$ and $\beta = c$ (c complex and α real) for temporal instability calculations while $\beta = \omega/\alpha$ (α complex and ω real) for spatial instability calculations and $i = \sqrt{-1}$. The boundary conditions are [9]

$$\varphi = \tilde{p}_\eta = 0 \qquad \text{on} \qquad \eta = 0,\tag{5.3}$$

$$\varphi \sim \frac{\varphi_\infty}{2} \left\{ K_{n+1}(\hat{\eta}) + K_{|n-1|}(\hat{\eta}) \right\} \quad \text{as} \quad \eta \to \infty, \tag{5.4}$$

$$\tilde{p} \sim \mp \frac{\varphi_\infty M_\infty^2 \mathrm{i}\alpha\gamma(1-\beta)K_n(\hat{\eta})}{[1 - M_\infty^2(1-\beta)^2]^{1/2}} \quad \text{as} \quad \eta \to \infty, \tag{5.5}$$

where $\hat{\eta} = \pm\alpha[1 - M_\infty^2(1-\beta)^2]^{1/2}(1/\zeta + \lambda\zeta + \eta)$, the sign of which is chosen such that the real part of the argument is positive in order for boundedness as $\eta \to \infty$ to be ensured, φ_∞ is a constant and $K_n(z_1)$ denotes the modified Bessel function of order n and argument z_1.

To achieve the planar limits, we firstly set $\lambda = 0$ in (5.1-5.2) and subsequently apply the limit $\zeta \to 0$, corresponding to flow in planar geometries. This yields

$$\varphi_\eta - \frac{W_{0\eta}\varphi}{W_0 - \beta} = \frac{\mathrm{i}\tilde{p}}{\gamma M_\infty^2(W_0 - \beta)} \left[T_0 - M_\infty^2(W_0 - \beta)^2 \right], \tag{5.6}$$

$$\mathrm{i}\alpha^2(W_0 - \beta)\frac{\varphi}{T_0} = -\frac{\tilde{p}_\eta}{\gamma M_\infty^2}. \tag{5.7}$$

The corresponding boundary conditions are

$$\varphi = \tilde{p}_\eta = 0 \quad \text{at} \quad \eta = 0, \tag{5.8}$$

and

$$\varphi \sim \varphi_\infty \exp[-\alpha\sqrt{1 - (1-\beta)^2 M_\infty^2}\, \eta], \tag{5.9}$$

$$\tilde{p} \sim -\frac{\mathrm{i}\varphi_\infty \gamma M_\infty^2(1-\beta)\exp[-\alpha\sqrt{1 - (1-\beta)^2 M_\infty^2}\, \eta]}{\sqrt{1 - (1-\beta)^2 M_\infty^2}} \quad \text{as} \quad \eta \to \infty. \tag{5.10}$$

Combining equations (5.6–5.7) and taking the limits $M_\infty \to 0$ and $T_0 \to cnst.$, results in

$$(W_0 - \beta)\left[\varphi_{\eta\eta} - \alpha^2\varphi \right] - W_{0\eta\eta}\varphi = 0, \tag{5.11}$$

which is the classic Rayleigh equation governing inviscid linear instability of incompressible boundary–layer flow in planar geometries.

(b) Numerical Methods

The physical range of the type of boundary layer being considered in what follows extends from zero at the solid boundary to suitably chosen far-field positions. This necessitates the use of mapping transformations between this range and the domain upon which the Chebyshev spectral collocation points are defined. The standard (real) Gauss-Lobatto collocation points

$$x_j = \cos\frac{j\pi}{N}, \qquad (j = 0, ..., N), \tag{5.12}$$

form the basis of all complex grids constructed in the sequel. The first of the complex grids employed (and the most straightforward) is based on transforming $[-1, 1]$ to a parabolic contour in the complex domain [1]. There are two ways to construct a complex grid which passes from the point $\eta = 0$ to $\eta = \eta_{max}$, the location on the real axis where the calculation domain is truncated.

One approach is to apply first the complex quadratic transformation [1]

$$y_j = x_j + \mathrm{i}\delta_1(x_j^2 - 1), \qquad \mathrm{i} = \sqrt{-1}, \tag{5.13}$$

taking the parabola that cuts the real axis at $y = -1$ and $y = 1$. Here δ_1 is a parameter whose effect

on the resultant solutions has been discussed by Theofilis *et al.* [13]. The physical domain is then mapped onto the computational domain using the following algebraic transformation [23]

$$\eta_j = l \frac{1 - y_j}{1 + s + y_j}, \tag{5.14}$$

where $s = 2l/\eta_{\max}$ and l is a stretching parameter. The grid defined by (5.14) is parabolic and avoids the critical point/layer by passing below it.

Conversely, the interval $[-1, 1]$ may be transformed to the computational interval $[0, y_{max}]$ (where $y_{max} = \eta_{max}$) using the algebraic transformation

$$y_j = l \frac{1 - x_j}{1 + s + x_j}, \tag{5.15}$$

and then maps it onto the complex domain, passing through the real points $\eta = 0, \eta = \eta_{max}$, using

$$\eta_j = y_j + i\, \delta_2 \left[(-1)^m \frac{(y_j - \eta_{max})^m}{\eta_{max}^{(m-1)}} + (y_j - \eta_{max}) \right], \tag{5.16}$$

where m is an integer with $m \geq 2$ and δ_2 is a parameter, both of which determine the characteristics of the integration path; as m increases (assuming that $\delta_2 < 0$ and remains constant) the maximum depth of the complex integration path increases and its minimum shifts towards the $Re(\eta) = 0$ axis, thus enabling the handling of critical points/layers which lie close to $\eta = 0$. This is useful in calculations of inviscid instability of incompressible wall-bounded flows. On the other hand, by changing the sign of δ_2, one can integrate above or below the real axis, for $\delta_2 > 0$ or $\delta_2 < 0$, respectively. Further, by increasing the absolute value of δ_2 one can increase the maximum depth/height of the complex integration path. Note, the real parts of the complex grid points (5.14) and (5.16) constructed using these alternate approaches are *not* identical. In other words, the real grid generated by setting $\delta_1 = 0$ is not the same as the one obtained for $\delta_2 = 0$.

The second complex grid considered is dependent on the availability of an estimate of the critical layer position. If such an estimate exists, then the grid can be deformed locally into the complex plane using an exponential complex mapping such as that proposed by Boyd [1]

$$y_j = x_j + i\delta_3\, e^{-(x_j - x_0)^2/c_0^2}, \tag{5.17}$$

where δ_3, c_0, x_0 are parameters. This mapping, combined with the algebraic transformation (5.14), allows for a short detour around the critical layer while hugging the real axis for the rest of the interval. Alternatively, the algebraic mapping (5.15) combined with the transformation

$$\eta_j = y_j + i\delta_4 y_j e^{-y_j}, \tag{5.18}$$

could be used. Note, this complex grid may result in serious convergence problems in the Chebyshev polynomials expansion of the eigenfunctions [1]. As in the case of real grid calculations, the chain rule is used to derive the modified collocation derivative matrices [4] which are employed in the computations.

(c) Instability results in planar and axisymmetric geometries

The classic Rayleigh equation is considered first. This, despite its apparent simplicity, provides a good test for the proposed algorithm due to the fact that for incompressible boundary–layer flows the critical layer is typically located very close to the wall. The complex grids which we employ need to coincide with the real point on the fixed boundary, where the boundary conditions are applied. Thus the computational grid must be deviated around the critical layer at a very short distance away from the boundary. In what follows we use two sets of complex mappings resulting from a combination of (5.15) with either (5.16) or (5.18), both of which have the ability to divert the complex grid over short distances.

The first test case considered is the Blasius boundary layer [17] which has a critical layer location close to the solid wall. The basic flow profile $W_0(\eta)$ was obtained by solving the Blasius equation on a real grid or directly on a complex grid. If the former case, a Taylor expansion was used to calculate the values of $W(\eta)$ on the complex nodes. The Rayleigh equation was discretised on the complex grid resulting from the combination of (5.15) and (5.16) or (5.15) and (5.18), using the appropriate collocation derivative matrices. The discrete eigenvalue problem was thus formulated as a generalized eigenvalue problem which was solved using the QZ algorithm. Mack [17] computed eigenvalues with an indented integration contour. For $\alpha = 0.179$ Mack quotes the eigenvalue $\omega = 0.05750554 - i0.00657109$ while the present spectral method yields $\omega = 0.05750493 - i0.00657192$ when the exponential mapping with $\delta_1 = -3.0$ is employed, and $\omega = 0.05750493 - i0.00657191$ when the polynomial mapping with $\delta_2 = -0.15, m = 5$ is used. For both spectral method calculations 100 collocation points were used with $\eta_{max} = l = 50$.

The second test case is the flat-plate boundary layer in compressible flow. It is well-known that as the Mach number increases the critical layer moves away from the wall outwards towards the edge of the boundary layer [17]. Thus for compressible calculations it is easier to determine a suitable complex grid which avoids the large gradient problems in the critical layer. By contrast to the Blasius boundary layer, where an inviscid linear instability analysis is of largely academic interest, linear instability of (viscous) compressible flow on both flat-plate and curved geometries can be well approximated by an inviscid analysis. Mode I and II inviscid linear instability calculations were performed for supersonic boundary-layer flow over a flat plate, choosing the relevant parameters from the related work of Duck [8] who monitored the planar limit of his equations against the calculations of Mack [18]. Basic flow calculations were performed on the complex collocation points defined by the combination of (5.15) and (5.16) with $m = 5$. The subsequent instability analysis was pursued in a temporal framework in order for comparisons with the aforementioned works to be possible. The analysis is based on equations (5.6-5.7) together with boundary conditions (5.8-5.10). First, we considered the incompressible planar limit taking $M_\infty = 10^{-4}$ and the mapping parameters of the incompressible calculations, $N = 100, \eta_{max} = l = 50, \delta_2 = 1.5$. The calculated eigenvalue at $\alpha = 0.179$ is $\omega = \alpha c = 0.05750493 - i0.00657192$, which agrees with the incompressible result in all decimal places. Next, supersonic inviscid linear instability calculations were performed at $M_\infty = 3.8$ for flow over an insulated flat-plate. We chose for all subsequent calculations $\eta_{max} = l = 25$ and present in Table 1 the combined effect of grid resolution and variation of the single remaining complex grid parameter δ_2 on the mode II eigenvalue obtained at $\alpha = 0.365$. In these results it may be seen that a real grid is inadequate to cope with this instability problem. The same conclusion may be drawn for calculations performed with $\delta_2 \geq 0.15$ at modest resolutions, while calculations at $\delta_2 \approx 0.05$ deliver the most accurate results at low resolutions. Finally, the results of Table 1 as well as others not shown here show that grid refinement in combination with a small positive value of δ_2, corresponding to a short detour into the complex plane, can deliver the converged eigenvalue. Taking the optimal parameters resulting from the present study, $N = 64$ and $\delta_2 = 0.05$, we present in Figure 6 the dependence of the eigenvalue c on the wavenumber parameter α for both mode I and mode II calculations. Excellent agreement with the superimposed relevant inviscid instability analysis results of Duck[8] may be seen. At maximum growth rate conditions the viscous analysis of Mack [18] predicts a mode II instability wave that is about 10% more stable than the inviscid result of Duck[8] reproduced herein by the complex–grid analysis.

The final validation calculation addressed solution of the linear instability equations for supersonic flow past axisymmetric bodies. The temporal linear instability analysis results of [9] are used for comparisons with our predictions. Figure 7 displays results obtained with the Runge-Kutta technique of Duck and Shaw [9] and our algorithm for the modes I and II of instability, for the case of a cone ($\lambda = 1$), at $\zeta = 0.05$, $M_\infty = 3.8$ and azimuthal wavenumbers, n, as shown. The complex grid used is defined as a combination of (5.13) and (5.14) with $N = 64, \delta_1 = -0.05, \eta_{max} = l = 25$. The graphical agreement of the results is very satisfactory. Next, we perform spatial calculations for the same physical parameters. We use a combination of (5.13) and (5.14) and an iterative algorithm at

variable resolutions to recover the leading eigenvalue. The dependence of the eigenvalues determined by the spectral collocation scheme on the complex grid mapping parameters is shown in Table 2. The bracket of δ_1 values in which we were able to obtain accurate results is rather narrow; erroneous results were obtained when the mapping parameter exceeds a threshold value. For this set of physical parameters the threshold was found to be $\delta_1 \approx -0.05$. However, the principal result of this section is that the complex spectral collocation technique proposed is capable of recovering inviscid linear local instability analysis results and thus becomes one viable candidate to address the corresponding two-dimensional eigenvalue problem. The results of this effort will be presented in due course.

6. Results

(a) Validation runs

(I) POISSON EQUATION ON THE ELLIPTIC CONFOCAL COORDINATE SYSTEM

Our first concern has been with the demonstration of the tools employed for the numerical solution of the generalised compressible Rayleigh equation on the elliptic confocal coordinate system. At the heart of this problem lies the ability to solve the appropriate Poisson equation

$$\left[\partial_{\xi\xi} + \partial_{\eta\eta} + h^2 p(\xi, \eta)\right] f(\xi, \eta) = q(\xi, \eta), \tag{6.1}$$

with $h = h(\xi, \eta)$ defined in (3.10) and $p(\xi, \eta), q(\xi, \eta)$ being infinitely differentiable functions on the elliptic confocal coordinate system $O\xi\eta$. Boundary conditions to close the system, which are relevant to the subsequent instability analysis, are homogeneous Dirichlet at the farfield and either Dirichlet or Neumann at the wall of the ellipse.

Several examples have been devised and solved, in order to validate (*i*) the coupled two-dimensional spectral collocation discretisation used, (*ii*) the imposed boundary conditions and (*iii*) the associated problem of symmetries expected (as opposed to imposed) in the solution. In all cases

$$q(\xi, \eta) = 1 \tag{6.2}$$

has been considered, while three cases have been monitored for $p(\xi, \eta)$,

$$\text{Case H}: \qquad p(\xi, \eta) = 1, \tag{6.3}$$

and

$$\text{Case S}: \qquad p(\xi, \eta) = \frac{\sinh\xi \sin^2 2\eta}{\left[c\sqrt{\sinh^2\xi + \sin^2\eta}\right]^3}, \tag{6.4}$$

resulting in symmetric solutions about both axes of the ellipse, and

$$\text{Case A}: \qquad p(\xi, \eta) = \frac{\sinh\xi \sin 2\eta}{\left[c\sqrt{\sinh^2\xi + \sin^2\eta}\right]^3}, \tag{6.5}$$

which breaks this symmetry in the solution, while it retains generalised symmetry about the centre of the integration domain.

Natural periodic boundary conditions are imposed by the Fourier expansion along the η coordinate direction, while along the ξ coordinate either Dirichlet

$$f(\xi = \xi_w, \eta) = 0, \ f(\xi = \xi_\infty, \eta) = 0 \tag{6.6}$$

or Neumann

$$f_\xi(\xi = \xi_w, \eta) = 0, \ f(\xi = \xi_\infty, \eta) = 0 \tag{6.7}$$

boundary conditions are imposed, ξ_w denoting the coordinate line (3.7) which defines the ellipse surface and ξ_∞ being the location along the ξ coordinate where the integration domain is truncated.

(II) NUMERICAL SOLUTIONS

A single configuration of an aspect ratio 4 elliptic cone with unit major semiaxis has been considered. A cut plane parallel to the cone base at a distance $z_0 = 0.5$ from the cone base results in an ellipse with geometric parameters

$$a = 0.5, \ b = 0.125, \ \xi_w \approx 0.255, \tag{6.8}$$

while $\xi_\infty = 1.5$ has been taken to truncate the integration domain. Six problems are then solved, namely H, S and A, employing Dirichlet or Neumann boundary conditions at the wall. The spectral collocation discretisation scheme of § 4 is used and the convergence history of the results for the wall value $f(x = a, y = 0) = f(\xi = \xi_w, \eta = 0)$, obtained from numerical solution of the Neumann problems, is presented in table 3 to within six significant digits, while the convergence history of the numerical solution of problems S and A is presented in figure 10. The spatial distribution of $f(x, y)$ for both Dirichlet and Neumann boundary data can be found in figures 11-13.

A key conclusion based on these results is that in all cases studied exponential convergence of the solutions of (6.1) has been obtained. The symmetries of the solutions are recovered, rather than being imposed, by the numerical approach taken. Furthermore, when the function sought has a simple, essentially one-dimensional (in ξ) structure, as the case is in problem H, a small number of collocation points suffices to solve (6.1) and further increases in resolution are unnecessary. This result is attributed to the convergence properties of the Fourier expansion in η and underlines the significance of the choice of the natural elliptic confocal coordinate system for the problem at hand. The low resolution requirements in the η direction in this class of problems, effectively suggesting that the available computing power can be almost exclusively devoted to resolution of the ξ spatial direction, is significant in terms of the ability of the two-dimensional eigenvalue problem to recover results of classic one-dimensional linear theory; in this case the instability mode can be described with a small number of Fourier modes accounting for resolution of the geometry in the lateral (η) direction, while its principal variation is along the wall-normal ξ direction.

As the structure of the sought function becomes increasingly more complicated higher resolution is necessary compared with that needed for problem H, although in both problems S and A also exponential convergence has been obtained. However, to the degree that conclusions on the spatial structure of the sought BiGlobal instability modes on the elliptic cone can be drawn upon evidence provided by the numerical solutions of problems A and S, a resolution issue for the inviscid compressible eigenvalue problem may arise if accuracy of the eigenvalue problem results beyond three to four significant digits is necessary, for instance in the case of near-neutral modes. In such cases a combination of the numerical methods of § 4 and § 5 may be necessary.

(*b*) *Instability analysis results on the elliptic confocal coordinate system*

(i) EXTRACTION AND MAPPING OF BASIC FLOW DATA ONTO THE $O\xi\eta$ PLANE

The numerical solution of the compressible generalised Rayleigh equation (2.28) requires basic state results on a plane $z = z_0$, parallel to the elliptic cone base, as schematically depicted on figure 8. Simple trigonometric formulae relate the semiaxes a, b and focal distance c of the ellipse on the cut plane with the respective quantities at the base of the elliptic cone, A, B, C, through

$$\frac{a}{A} = \frac{b}{B} = \frac{c}{C} = \frac{z_0}{Z}. \tag{6.9}$$

For a given elliptic cone geometry and distance z_0 of the cut plane from the tip of the cone, the quantities a, b and c can be calculated in this manner. In turn, with known semiaxes of the ellipse on the cut plane (3.1-3.2) relate the cartesian system $Oxyz$ of the basic flow calculations (Theofilis [25]) with the elliptic confocal system $O\xi\eta$ on which the instability analysis is to be performed.

Basic flow data are transferred from the steady three-dimensional unstructured-grid results using second-order accurate interpolation onto an optimal *'nearest-neighbour'* two-dimensional tessellation of the Oxy plane, the latter generated by the interpolation software which supports the 3D-visualisation package used. Since the basic flow results have been obtained using a second-order accurate finite-volume method, use of a higher order interpolation procedure is not justified and one has to rely on

high resolution in order to improve the quality of the basic state. A second bivariate interpolation procedure generates a unique Thiessen triangulation and calculates basic flow derivatives on the new unstructured grid on the Oxy plane. The result is then used to perform a third and final, also second-order accurate, interpolation, which delivers the necessary basic flow streamwise velocity component, density and pressure on the elliptic confocal coordinate system $O\xi\eta$. Derivatives of these quantities with respect to ξ and η are then calculated using the collocation derivative matrices.

Clearly, this sequence of interpolations carries the potential of cumulative error being introduced, so alternative approaches pointing to future research directions are briefly discussed here. Use of the same ($z-$independent) elliptic confocal coordinate system to obtain basic flow data and perform the instability analysis would eliminate the error introduced by interpolations. However, the implication would be that flow on an elliptic cylinder, rather than on an elliptic cone, would be monitored by such an approach and information on flow three-dimensionality, currently obtained through successive instability analyses at different z_0 locations, would be lost. As has been discussed in § 3, a three-dimensional grid constructed of elliptic confocal planes normal to the cone axis at different z_0 locations is not an orthonormal frame of reference; in other words, on account of the three-dimensionality of the elliptic cone geometry it is not possible to construct a three-dimensional orthonormal frame of reference having the two-dimensional plane Oxy on which the present analyses are performed embedded to it.

Returning to the coordinate system of figure 1, a related issue that must be addressed in this context is the extent of the domain on which basic flow data are interpolated/retained along the ξ direction. Although it is in principle possible to define the cut plane for the instability analysis so that it either incorporates or avoids the Mach cone (in supersonic/hypersonic flow), this was not done in anticipation of potential resolution issues in the instability analysis should the first course of action be taken or the ambiguity of defining an outer boundary in the ξ direction in the region between the cone surface itself and the shock location. Consequently, the shock location itself was chosen as the boundary at which homogeneous Dirichlet boundary conditions were imposed on the disturbance pressure in all subsequent calculations. At the wall homogeneous Neumann conditions were imposed.

(ii) INVISCID EIGENDISTURBANCES ON THE ELLIPTIC CONE

With these considerations in mind, attention has been focussed on three configurations, an aspect ratio 3 elliptic cone in subsonic viscous ($M = 0.5, Re = 10^3$) flow, an aspect ratio 4 elliptic cone in supersonic inviscid ($M = 4$) and an aspect ratio 2 elliptic cone in hypersonic viscous ($M = 8, Re = 10^3$) flow. The subsonic calculations have been performed on a 3D unstructured grid encompassing $\sim 2 \times 10^6$ points on the half plane $x > 0$; the converged (in time) steady results were mirrored with respect to the plane $x = 0$, while in the second and third cases flow over the entire cone has been solved. The subsequent instability analysis is expected to deliver an answer, in the form of sign of the amplification rate, as to whether the assumptions of symmetry in the case of the subsonic flow and steadiness in both cases studied are physically realisable. The supersonic/hypersonic calculations have been performed on unstructured 3D grids encompassing $> 2.5 \times 10^6$ points. Respectively, the angles of attack $\alpha = 20^\circ, 5^\circ$ and $\alpha = 0^\circ$ have been considered, while in all cases a zero yaw angle has been taken. Monitoring three different basic states at several different parameters parameters may make physical interpretation of the respective results and their relation to one another a rather challenging task. However, the primary focus of this work has been demonstration of the tools necessary for the analysis from a numerical point of view; systematic investigations of inviscid BiGlobal instability from a physical point of view is a task of future research.

The basic states utilised for the analyses at the extreme Mach number conditions are shown graphically in figures 14 and 15 [25]. In line with the assumptions underlying the compressible generalised Rayleigh equation, only the streamwise basic flow velocity component $\bar{w}$ was retained in the analyses (alongside the density and pressure distributions). This assumption is increasingly valid as the Mach number increases; for example, in the supersonic and hypersonic cases solved, the peak $\bar{w}$ value is more than one order of magnitude larger than that of $\bar{v}$ and several orders of magnitude larger than that of

the velocity component $\bar{u}$ along the lateral spatial direction x. Correspondingly, the results obtained are expected to be increasingly relevant to the three-dimensional physical problem as M increases. In all cases solved the spatial concept has been followed, in which ω is taken to be a real parameter denoting frequency and the eigenvalue $\beta = \beta_{\mathrm{r}} + \mathrm{i}\beta_{\mathrm{i}}$ is sought; in a manner analogous with classic linear theory, $\beta_{\mathrm{r}} = \mathrm{Re}\{\beta\}$ represents a wavenumber along the homogeneous z spatial direction along which the disturbance grows or decays if $\beta_{\mathrm{i}} = \mathrm{Im}\{\beta\} < 0$, or > 0, respectively. A final point relevant to all calculations performed is that the QZ algorithm has been used for the recovery of the full eigenspectrum. While this algorithm is highly inefficient and its application may even lead to concealment of physically relevant modes on account of the modest attainable resolution in comparison with Krylov subspace iteration methods [26], use of the QZ algorithm was deemed necessary at this stage, since no prior guiding information on potentially interesting areas of the eigenvalue spectrum is available. Consequently, on account of the $O((N_\xi N_\eta)^3)$ CPU time scaling of the QZ algorithm, only modestly high resolutions, up to $N_\xi \times N_\eta = 40 \times 40$ have been used.

Figure 16 presents the spatial eigenspectrum obtained at $M = 0.5, \omega = 10^{-2}$. The calculations are are inconsistent for most travelling disturbances and only stationary neutral pressure eigenmodes could be converged at these conditions using up to 30×30 collocation points; higher resolution increased the number of converged stationary disturbances but did not yield converged travelling mode results. Three stationary neutral eigenmodes are shown in figures 17-19. The most striking feature is the symmetry about $x = 0$ in all three results, alongside the absence of symmetry in the azimuthal ξ direction in the first two eigenmodes. The symmetry about $x = 0$ is a result of that of the basic state, while the absence of azimuthal symmetry implies that the respective eigenmodes cannot be obtained by application of the simplified linear analysis concept in which the Ansatz

$$\mathbf{q} = \bar{\mathbf{q}}(\xi, \eta) + \varepsilon\,\hat{\mathbf{q}}(\xi)\,\exp\left[i(\lambda\eta + \beta z - \omega t)\right] \qquad (6.10)$$

replaces (2.1). The present results are the first indication that employing (6.10) inhibits large-scale non-azimuthally-periodic perturbations, such as those shown in figures 17-18, from revealing themselves in the eigenvalue spectrum. For such non-azimuthally-periodic disturbances (2.1) must be used. Focussing on the result of figure 17 one notes that this eigenmode possesses a structure which is resolved to (qualitatively) the same good degree as those of the model Poisson problems shown in the earlier section. The pressure eigenfunction and its derivatives are smoothly reduced to zero at the outer boundary, while most of the activity takes place in the immediate vicinity of the cone surface. The differential pressure on the windward and leeward sides of the cone is clearly visible in the results. Further, the η−derivative of this result bears a striking similarity with the spatial structure of the basic velocity profile. Qualitatively analogous conclusions may be drawn from the results of figure 18, although in this case the locations of primary vortex separation is clearly visible in the results, as stagnation points in the disturbance pressure signal. This result points to the potential of utilising BiGlobal instability analysis to provide an alternative framework for the well-studies vortex breakdown problem on delta wings, a problem which has received a large amount of attention using (6.10) but virtually none by application of the more appropriate, in our opinion, decomposition (2.1). Such a study could be pursues by systematically departing from the classic circular cone geometry [21] to progress towards a delta wing configuration via a sequence of elliptic cones at aspect ratios $AR \in (1, \infty)$. Finally, the result of figure 19 is representative of a class of pressure eigenmodes also found in the simulations, which may be considered as azimuthally-periodic and, as such, might be able to be addressed by the simplified concept (6.10). However, although using (6.10) at a single (ξ_w, η)−location may be orders-of-magnitude less CPU-time-consuming than use of BiGlobal instability analysis, the simplified linear theory concept must be repeated at a sufficient number of η−locations along the wall ξ_w in order for a picture of the instability mode along the entire η−coordinate to be formed, such that BiGlobal analysis may be competitive even for this subclass of disturbances. All conclusions put forward in the subsonic case must be viewed in the framework of

the certainly questionable in subsonic flow simplifying assumption $\bar{u} = \bar{v} = 0$. The results obtained may be viewed as approximations of the BiGlobal eigenmodes which are expected to be obtained if the full viscous problem is solved. Nevertheless, solution of the latter problem is not expected to discredit the main result obtained herein, namely the existence of large-scale non-azimuthally periodic eigendisturbances. As mentioned before, the assumptions of the compressible generalised Rayleigh equation are increasingly valid as the flow Mach number increases, and we next turn to the supersonic and hypersonic cases addressed.

Figure 20 presents the spatial eigenspectrum obtained at $M = 4.0, \omega = 10^{-2}$. By contrast to the spectrum of figure 16 here both stationary and travelling disturbances could be converged using up to 30×30 collocation points. Attention is focussed here on four families of eigenmodes, indicated as A, B, C and D in figure 20, which at least qualitatively have converged and point to different classes of eigendisturbances; representative members of these families are respectively presented in figures 21- 24. In comparison with the respective subsonic modes, all supersonic pressure eigendisturbances recovered were found to be more compact, extending over a narrower $\xi-$range that their subsonic counterparts, in line with analogous experience with modes of classic linear theory. Members of family A, one of which is shown in figure 21, extend only on the windward face of the elliptic cone and may have a single- (as that shown in fig. 21) or multiple-mode structure along the azimuthal direction. Modes pertaining to family B, on the other hand, one representative member of which is shown in fig. 22, are the conceptual leeward analogon of the windward modes A and exhibit are in all other respects similar characteristics with the A modes, namely a compact structure in the neighbourhood of the body surface that quickly decays to zero as the free-stream is approached. Modes pertaining to either of families A or B might be well approximated by classic analysis based on (6.10), provided the latter is employed only on the appropriate face of the cone. Neutral modes, members of families C and D, possess a structure extending over the entire integration domain; two examples are shown in figures 23 and 24. A conclusion with far-reaching implications regarding results of family C is that BiGlobal instability analysis may have a useful role to play in identifying travelling neutral pressure eigenmodes which play a central role in the field of computational aeroacoustics (CAA). Further research to quantify this conjecture, which could form one potential extension of the present work, is required in this area; if this conjecture is confirmed, orders-of-magnitude computational savings may be realised in CAA by applying BiGlobal instability analysis instead of the currently almost exclusively used DNS methodology [5]. Before making final statements in this respect, the influence of the domain extent on the instability characteristics of the neutral travelling pressure eigenmodes must be assessed, for example by comparison with DNS studies of the same geometry [29, 30]. One question that may be posed in this respect is whether the structure of family C BiGlobal eigenmodes is a result of the imposed homogeneous Dirichlet boundary conditions at the shock location, and consequent reflections within the resolved domain, or whether imposition of (in)homogeneous Neumann far-field pressure boundary conditions would preserve/alter the recovered structure, for example in terms of the clearly identifiable wavelengths. Finally, in line with the analogous result obtained in the subsonic case, stationary neutral eigenmodes are also found in the BiGlobal spectrum, here identified as family D, a typical member of which is shown in figure 24. Both the different levels of disturbance pressure on the wind- and lee side of the flow as well as the slightly non-symmetric nature of this mode can be seen. The latter may be attributed either to poor spatial resolution of the basic state, although it is likely that the symmetric about $x = 0$ counterpart of this mode may also be found in the eigenspectrum. Another issue relevant to the existence of inviscid neutral modes, either stationary or travelling, has been introduced in § 5, namely the ambiguity in the definition of a critical 'layer' concept in the solution of the inviscid two-dimensional eigenvalue problem. Even if one is satisfied from a physical point of view that the present results are plausible solutions of the BiGlobal eigenvalue problem, the neutral results obtained herein should be contrasted against of solutions of (2.28) employing complex tensor-product grids before proclaimed as being physically relevant, which defines another potentially interesting extension of the present work.

Turning to the highest Mach number value monitored, one notes that on account of a zero angle of attack the basic state is symmetric about both $x = 0$ and $y = 0$, which results in analogous symmetries being preserved in the BiGlobal eigenvalue problem as well; a typical result is shown in figure 25. The far-field location ξ_∞ along the ξ−coordinate where homogeneous Dirichlet boundary conditions on the disturbance pressure have been imposed, namely $\xi_\infty \leq \xi_s$, $\xi_s(\eta)$ denoting the shock location, has been kept the same as in the $M = 4$ calculations. The main qualitative analogy between the BiGlobal eigenspectra at $M = 4$ and $M = 8$ is that (alongside stationary and neutral modes) families of travelling modes having analogous structure to families A and B are identified at $M = 8$ too. To the extent that comparisons are permitted without having established that the modes in question at $M = 8$ can be continuously obtained by systematically increasing the flow Mach number, the travelling modes of a specific family at $M = 8$ are found to be more stable than their counterparts at $M = 4$, a result which is in line with the predictions of classic linear theory based on (6.10) on wave-like linear disturbances.

In view of the qualitatively analogous results obtained in the $M = 8$ spectrum compared with the $M = 4$ case, no further discussion of the BiGlobal eigenspectra is included here. Instead, a different path in the multiparametric space at hand has been followed, namely investigation of the effect of extending the domain on which the BiGlobal eigenvalue problem has been solved well beyond the shock location. Motivation for this undertaking is provided by the different significance of the concepts of 'wall-normal distance' and 'far-field' when employing (6.10) or (2.1). In the case of classic linear theory a characteristic length scale in experimentation and calculations is provided by the thickness of the boundary layer developing on the elliptic cone. By contrast, the BiGlobal instability analysis results obtained so far at the lower Mach numbers point to the existence of large-scale disturbances which scale with the elliptic cone semiaxes. In this framework the shock location is too close to the cone surface to be considered as an appropriate 'far-field' position at which homogeneous Dirichlet boundary conditions on the disturbance pressure may be imposed. On the other hand, enlarging the extent of the integration domain approximately by a factor four along the ξ coordinate, in combination with the use of an unmapped grid in the ξ−direction which relies on the natural clustering of the elliptic confocal system to resolve near-wall structures, may result in loss of resolution adjacent to the cone surface and, possibly, inability to resolve wave-like disturbances scaling with the boundary layer thickness. It is precisely the objective of this part of the present investigation to determine whether certain instabilities exist that are insensitive to this domain change and determine their spatial structure.

The most interesting results of the latter investigation have been the following. First, analogously with the narrower domain computations, stationary and travelling neutral modes exist, while a strong modification of the location, in (β_r, β_i) parameter space, of the travelling eigendisturbances may be observed on account of the wider integration domain. The spectra at the resolutions utilised which, despite not having converged yet, demonstrate qualitatively consistent structure of their branches, are shown in figure 26. Second, the spatial structure of stationary and travelling neutral modes, which are marginally resolved at the resolutions utilised, points to the fact that these modes are sensitive to the location of the imposition of the boundary condition. A typical result may be found in figure 27, where it can be seen that no physical justification exists as to why homogeneous Dirichlet boundary conditions should be imposed on the disturbance pressure at the chosen ξ_∞ value; a different type of boundary condition is necessary to capture these modes correctly. Third, by contrast, homogeneous Dirichlet pressure boundary conditions appear to be adequate for travelling disturbances; members of two different classes (i.e. branches of travelling modes in the eigenspectrum of figure 26) are shown in figures 28 and 29. Interesting in these results are, at least, two facts. On the one hand, the shock location (which may be inferred by comparison with the result of figure 25) does not appear to interfere with / influence the spatial structure of such eigendisturbances which are smoothly reduced to zero in the far-field. On the other hand, these two classes of modes are essentially different in one aspect, namely their η−dependence: While the mode shown in figure 28 could be expected to be recovered by application of (6.10) at appropriately higher resolution, that shown in figure 29 appears to fall outside

the scope of the simplified linear analysis and require the present BiGlobal concept for its study. In other words, within the framework of the assumptions of the present approach, there appear to exist in the elliptic cone linearly amplified eigendisturbances which are localised in the neighbourhood of the cone itself, scale with an $O(1)$ geometrical length of the body in question and are beyond the scope of the simplified linear theory. Further study to quantify this discovery, which is consistent at all Mach numbers examined and could utilise existing experimental data or be performed in parallel with new experimental efforts, is essential for progress in the theoretical understanding of instability mechanisms operative in this technologically key flow configuration.

7. Discussion

The present effort has commenced with the global instability analyses of the steady-state basic flows on elliptic cones obtained in [25]. The three-dimensionality of the elliptic cone introduces a freedom in the choice of coordinate systems which may be utilised to isolate different factors affecting flow instability in a natural manner by appropriate choice of the coordinate system on which the analysis is performed. Three different alternatives have been introduced, having distinct properties the merits of which have been assessed. On grounds of numerical efficiency it has been proposed to conduct the analysis on the elliptic confocal coordinate system, which is the two-dimensional analogon of the elliptic cylindrical system in three-dimensional space. This mapping has (at least) three advantages; first, it takes into account the essential elliptical nature of the geometry surface in a natural manner. Second, it naturally clusters points in the boundary layer while the grid density decreases exponentially in the far-field, thus permitting placing the outflow boundary at a large distance from the body surface without wasting gridpoints in that region. Third, the analytical nature of the mapping permits the calculation of metrics of the transformation without introduction of numerical error. A potential disadvantage of the elliptic confocal coordinate system is that three-dimensionality of the flow in the streamwise direction is neglected; however, this is consistent with the assumption of two-dimensional global linear theory which neglects the dependence of the flow on the third spatial direction along the elliptic cone axis, i.e. derivatives of flow quantities along this direction are neglected. In this manner no additional physical information is expected to be lost on account of the choice of the coordinate system compared with that implied by two-dimensional BiGlobal analysis.

The two-dimensional viscous compressible partial-derivative eigenvalue problem has been derived in a cartesian coordinate system. Potential simplifications have been discussed one of which, the generalised Rayleigh equation, has been expressed in the elliptic confocal coordinate system as either a temporal or a spatial eigenvalue problem; numerical prescriptions have been provided for its collocation. However, if a global inviscid instability analysis methodology is followed, the common approach of shooting/iteration used in local inviscid analysis is inapplicable and the analysis must be performed by solving the partial derivative eigenvalue problem as a nonsymmetric generalised matrix eigenvalue problem. This may lead to inaccurate results on account of poor resolution of the critical layer(s) if computations are performed on a real grid and weakly-amplified/damped or (near-) neutral modes are sought. In order to circumvent this problem an algorithm has been presented which poses the inviscid local eigenvalue problem as a matrix eigenvalue problem defined on complex spectral collocation calculation grids. Since this algorithm could become the cornerstone of a potential global inviscid analysis, its accuracy and robustness has been demonstrated in several validation calculations of the local inviscid eigenvalue problem in planar and curved geometries.

The numerical tools proposed for the solution of the compressible generalised Rayleigh equation have been validated on model Poisson problems, devised to conform with the boundary conditions and mimic the spatial structure of the expected eigendisturbances; exponential convergence of the model problem solutions has been demonstrated. Attention has then been focussed on numerical aspects of the analysis of three elliptic cone configurations at a variery of parameters/conditions in order for experience with the different facets of this novel problem to be accumulated. Results obtained at all Reynolds and Mach numbers studied point to the existence of large-scale instabilities, which scale with a geometric length of the respective elliptic cone and not with the thickness of the boundary layer developing on its surface; indeed, the persistence of large-scale eigendisturbances superimposed upon inviscid basic states a-priori excludes the possibility that such disturbances can be associated with Tollmien-Schlichting instability on the cone surface. Nevertheless, numerical evidence (in the form of well-resolved azimuthally-periodic eigenmodes) has been obtained that the latter type of disturbance may also be resolvable if the integration domain is restricted within the Mach cone (in supersonic/hypersonic flow). A persistent finding of all analyses has been the appearance in the spectrum of neutral stationary and travelling disturbances. Although several such eigenmodes are converged, the complex grid technique presented must be used before neutral or marginally amplified/damped modes are proclaimed to be physically

relevant. On the other hand, travelling disturbances with $O(1)$ amplification rates have been identified, which can be reasonably well resolved on real grids: while the maximally attained resolution at which the model Poisson problems have been converged to within several significant places cannot be achieved on present-day hardware when using the QZ algorithm for the eigenvalue problem, specific parts of the eigenspectrum could be monitored with high resolution when using Krylov subspace iteration (e.g. [26]).

Several questions are left open and new issues have been generated by the present effort. The apparent ability of the methodology to address neutrally-stable travelling pressure eigendisturbances points to a potential utilisation of BiGlobal instability analysis in a CAA context; such efforts should be accompanied by theoretical considerations regarding the concept of critical 'layer' of the two-dimensional eigenvalue problem and the complex-grid algorithm presented herein. Subsonic flow has been found easiest to resolve numerically, albeit that the restrictive assumptions of the generalised Rayleigh equation may not permit studying such flows from a physical point of view when using this type of inviscid analysis. Nevertheless, the reasonably accurate description of the area of flow separation from an elliptic cone surface at an angle of attack points to the potential of BiGlobal instability analysis to address the issue of vortex breakdown in this or high-angle-of-attack flow over a delta-wing using this novel methodology. In the problem at hand, from a physical point of view, the assumptions of inviscid theory are increasingly applicable as the flow Mach number increases. Although subsonic BiGlobal calculations are the easiest to perform numerically, neglecting all but the streamwise velocity component in this case is highly questionable and may confuse potential discrepancies of BiGlobal instability analysis results with those of experiment/DNS. Consequently, further efforts on BiGlobal instability analysis on the elliptic cone should focus on the supersonic/hypersonic regimes alone. Further progress in this area is expected to be made by close interaction with experiment and/or DNS, so that physically interesting configurations and parameter ranges are isolated and studied in detailed in the framework of the present analysis.

Appendix A. The elliptic confocal coordinate system

Take the conformal transformation

$$w = \frac{1}{2}\left(z + \frac{1}{z}\right),\tag{A 1}$$

where z and w are complex variables. In polar notation,

$$z = r e^{i\eta}\tag{A 2}$$

which leads to

$$w = \frac{1}{2}\left(r e^{i\eta} + \frac{1}{r}e^{-i\eta}\right).\tag{A 3}$$

Introducing $w = \frac{1}{c}(x + iy)$, where c is a real parameter, leads to

$$x = \frac{1}{2}c\left(r + \frac{1}{r}\right)\cos\eta\tag{A 4}$$

$$y = \frac{1}{2}c\left(r - \frac{1}{r}\right)\sin\eta.\tag{A 5}$$

Key to the transformation is the introduction of

$$r = e^{i\xi},\tag{A 6}$$

which results in the relationship between the cartesian and the elliptic confocal coordinate system

$$x = c\cosh\xi\cos\eta\tag{A 7}$$

$$y = c\sinh\xi\sin\eta,\tag{A 8}$$

c being identified as the focal distance of the ellipse.
Combining (A 3) and (A 6) one arrives at

$$x + iy = c\cosh(\xi + i\eta)\tag{A 9}$$

which may be used to derive the inverse transformation, necessary for the numerical work in the $O\xi\eta$ plane given the basic flow results on the Oxy plane,

$$\xi + i\eta = \frac{1}{c}\cosh^{-1}(x + iy).\tag{A 10}$$

The semi-axes of the ellipse can be obtained by introducing into (A 7-A 8) the limits $\eta = 0$ and $\eta = \pi/2$,

$$a = c\cosh\xi,\tag{A 11}$$

$$b = c\sinh\xi.\tag{A 12}$$

Rearranging (A 11-A 12) the well-known relationship between the focal distance and the semiaxes of the ellipse

$$c^2 = a^2 - b^2\tag{A 13}$$

may also be obtained. Also, combining (A 11-A 12) the equation of the ellipse $\xi_w = cnst.$ describing the wall boundary is obtained,

$$\tanh \xi_w = \frac{\sinh \xi_w}{\cosh \xi_w} = \frac{b}{a} = \frac{\mathrm{e}^{\xi_w} - \mathrm{e}^{-\xi_w}}{\mathrm{e}^{\xi_w} + \mathrm{e}^{-\xi_w}}. \tag{A 14}$$

This may be rearranged to arrive at

$$\xi_w = \frac{1}{2} \ln \frac{a+b}{a-b} = \ln \frac{a+b}{c}, \tag{A 15}$$

which is the equation of the wall boundary in the elliptic confocal coordinate system in terms of the semiaxes and focal distance of the ellipse.

V. Theofilis

Appendix B. The temporal and spatial eigenvalue problems in elliptic confocal coordinates

Given basic flow quantities and their derivatives on the elliptic confocal system, the eigenvalue problems are defined by the matrices $T_1 - T_{12}$ and $S_1 - S_{12}$,

$$T_1 = \beta\,\gamma\,\overline{\rho}\,\bar{p}\,\bar{w}$$

$$T_2 = \beta\,\gamma\,\overline{\rho}\,\bar{p}\,\bar{w}$$

$$T_3 = \left(\beta\,\overline{\rho}\,\bar{p}_\xi\,\bar{w} - \beta\,\gamma\,\overline{\rho}_\xi\,\bar{p}\,\bar{w} - 2\beta\,\gamma\,\overline{\rho}\,\bar{p}\,\bar{w}_\xi\right)$$

$$T_4 = \left(\beta\,\overline{\rho}\,\bar{p}_\eta\,\bar{w} - \beta\,\gamma\,\overline{\rho}_\eta\,\bar{p}\,\bar{w} - 2\beta\,\gamma\,\overline{\rho}\,\bar{p}\,\bar{w}_\eta\right)$$

$$T_5 = \left(\beta^3\,\overline{\rho}^2\,\bar{w}^3 - h^2\,\beta^3\,\gamma\,\overline{\rho}\,\bar{p}\,\bar{w}\right)$$

$$T_6 = \gamma\,\overline{\rho}\,\bar{p}$$

$$T_7 = \gamma\,\overline{\rho}\,\bar{p}$$

$$T_8 = \left(\overline{\rho}\,\bar{p}_\xi - \gamma\,\overline{\rho}_\xi\,\bar{p}\right)$$

$$T_9 = \left(\overline{\rho}\,\bar{p}_\eta - \gamma\,\overline{\rho}_\eta\,\bar{p}\right)$$

$$T_{10} = \left(3\,\beta^2\,\overline{\rho}^2\,\bar{w} - h^2\,\beta^2\,\gamma\,\overline{\rho}\,\bar{p}\right)$$

$$T_{11} = -3\,\beta\,\overline{\rho}^2\,\bar{w}$$

$$T_{12} = \overline{\rho}^2$$

$$S_1 = \omega\,\gamma\,\overline{\rho}\,\bar{p}$$

$$S_2 = \omega\,\gamma\,\overline{\rho}\,\bar{p}$$

$$S_3 = \omega\left(\overline{\rho}\,\bar{p}_\xi - \gamma\,\overline{\rho}_\xi\,\bar{p}\right)$$

$$S_4 = \omega\left(\overline{\rho}\,\bar{p}_\eta - \gamma\,\overline{\rho}_\eta\,\bar{p}\right)$$

$$S_5 = \omega^3\,\overline{\rho}^2$$

$$S_6 = \gamma\,\overline{\rho}\,\bar{p}\,\bar{w}$$

$$S_7 = \gamma\,\overline{\rho}\,\bar{p}\,\bar{w}$$

$$S_8 = \left(\overline{\rho}\,\bar{p}_\xi\,\bar{w} - \gamma\,\overline{\rho}_\xi\,\bar{p}\bar{w} - 2\,\gamma\,\overline{\rho}\,\bar{p}\,\bar{w}_\xi\right)$$

$$S_9 = \left(\overline{\rho}\,\bar{p}_\eta\,\bar{w} - \gamma\,\overline{\rho}_\eta\,\bar{p}\bar{w} - 2\,\gamma\,\overline{\rho}\,\bar{p}\,\bar{w}_\eta\right)$$

$$S_{10} = 3\,\omega^2\,\overline{\rho}^2\,\bar{w}$$

$$S_{11} = \omega\left(h^2\,\gamma\,\overline{\rho}\,\bar{p} - 3\,\overline{\rho}^2\,\bar{w}\right)$$

$$S_{12} = \left(\overline{\rho}^2\,\bar{w}^3 - h^2\,\gamma\,\overline{\rho}\,\bar{p}\,\bar{w}\right)$$

(B 1)

in the temporal and spatial case, respectively.

Appendix C. Calculation of differential operators in arbitrary orthonormal coordinate systems

(a) Preliminaries

The first step required by differential form theory [11, 3] is to calculate the dual basis $(\tilde{\omega}^s, \tilde{\omega}^n, \tilde{\omega}^\theta)$ associated with a vector space according to the correspondence

$$
\begin{array}{ccc}
\text{vector components} & \Longleftrightarrow & \text{1-Forms} \\
\Updownarrow & & \Updownarrow \\
(v_s, v_n, v_\theta) & & (\tilde{\omega}^s, \tilde{\omega}^n, \tilde{\omega}^\theta) \\[2mm]
\text{basis vectors} & & \text{basis 1-Forms} \\
\Updownarrow & & \Updownarrow \\
(\mathbf{e}_s, \mathbf{e}_n, \mathbf{e}_\theta) & \Longleftrightarrow & (ds, dn, d\theta).
\end{array}
$$

The 1-Forms satisfy the schematic relation

$$
dx^i\left[\frac{\partial}{\partial x^k}\right] = \delta_k^i, \qquad \omega^i\left[\mathbf{e}_k\right] = \delta_k^i, \tag{C 1}
$$

where square brackets signify application of the operator to the vector/1-Form inside the bracket and δ_k^i is the Kronecker delta.

The second step, is to use the dual basis to express the operators appearing in the equations of motion. For example, the gradient operator is the 1-Form df, defined as the exterior derivative of a scalar field f,

$$
df = \partial f / \partial x^i \; dx^i, \tag{C 2}
$$

x^i being any chosen coordinate system and dx^i the corresponding basis 1-Forms. The definitions (C 1) are then used to express the coefficients of the expansion in (C 2) in terms of the dual basis $\left\{\tilde{\omega}^i\right\}$; the coefficients of the result express the gradient operator in an arbitrary coordinate system x^i.

(I) Gradient

For simplicity of exposition of the ideas of differential form theory we calculate the gradient operator in cylindrical coordinates. While this approach turns out to be rather long-winded for this simple problem, differential form theory can also be applied in case no analytic expressions are available to link the original and the target coordinate system; this is precisely the case with two of the three coordinate systems discussed in § 3(c) in the elliptic cone.

In vector-component form the coordinate transformation is defined by

$$
\begin{pmatrix} x \\ y \\ z \end{pmatrix} = \begin{pmatrix} r\cos\phi \\ r\sin\phi \\ z \end{pmatrix}.
$$

This yields

$$
dx = r\cos\phi \; dr - r\sin\phi \; d\phi, \tag{C 3}
$$

$$
dy = r\sin\phi \; dr + r\cos\phi \; d\phi, \tag{C 4}
$$

$$
dz = dz. \tag{C 5}
$$

The unknown 1-Forms $(\tilde{\omega}^r, \tilde{\omega}^\phi, \tilde{\omega}^z)$ can be expressed in terms of the basis 1-Forms $(dx,\ dy,\ dz)$ as

$$\tilde{\omega}^r = \tilde{\omega}^r_x\ dx + \tilde{\omega}^r_y\ dy + \tilde{\omega}^r_z\ dz,$$
$$\tilde{\omega}^\phi = \tilde{\omega}^\phi_x\ dx + \tilde{\omega}^\phi_y\ dy + \tilde{\omega}^\phi_z\ dz,$$
$$\tilde{\omega}^z = \tilde{\omega}^z_x\ dx + \tilde{\omega}^z_y\ dy + \tilde{\omega}^z_z\ dz.$$

where $\tilde{\omega}^i_j$ are unknown coefficients. Application of (C 1) yields three 3×3 systems for the unknown coefficients $\tilde{\omega}^i_j$ of the 1-Forms.

For example,

$$\left(\tilde{\omega}^r_x\ dx + \tilde{\omega}^r_y\ dy + \tilde{\omega}^r_z\ dz\right)\left[\mathbf{e}_r\right] = 1$$
$$\left(\tilde{\omega}^r_x\ dx + \tilde{\omega}^r_y\ dy + \tilde{\omega}^r_z\ dz\right)\left[\mathbf{e}_\phi\right] = 0,$$
$$\left(\tilde{\omega}^r_x\ dx + \tilde{\omega}^r_y\ dy + \tilde{\omega}^r_z\ dz\right)\left[\mathbf{e}_z\right] = 0.$$

Substituting the basis 1-Forms (dx, dy, dz) in terms of $(dr, d\phi, dz)$ and recalling (C 1), i.e. $dr\left[\mathbf{e}_r\right] = 1, d\phi\left[\mathbf{e}_r\right] = 0, dz\left[\mathbf{e}_r\right] = 0$, the system

$$\cos\phi\ \omega^r_x + \sin\phi\ \omega^r_y = 1/r,$$
$$-\sin\phi\ \omega^r_x + \cos\phi\ \omega^r_y = 0,$$
$$\omega^r_z = 0$$

is obtained from which $\omega^r_x = 1/r \cos\phi$, $\omega^r_y = 1/r \sin\phi$, and $\omega^r_z = 0$ follows. Substitution of these quantities into the expansion of $\tilde{\omega}^r$ and use of (C 3-C 5) completes the calculation of $\tilde{\omega}^r$. In an analogous manner the other components of the dual basis are obtained,

$$\omega^r = dr \tag{C 6}$$
$$\omega^\phi = r\ d\phi \tag{C 7}$$
$$\omega^z = dz. \tag{C 8}$$

Next, the dual basis calculated is used to express the gradient operator. In the chosen coordinate system the gradient operator takes the form

$$df = \frac{\partial f}{\partial r}\ dr + \frac{\partial f}{\partial \phi}\ d\phi + \frac{\partial f}{\partial z}\ dz$$
$$= \frac{\partial f}{\partial r}\ \tilde{\omega}^r + \frac{1}{r}\frac{\partial f}{\partial \phi}\ \tilde{\omega}^\phi + \frac{\partial f}{\partial z}\ \tilde{\omega}^z,$$

where the 1-Forms $(dr, d\phi, dz)$ have been expressed in the calculated dual basis (C 6-C 8). One recognizes that *the components of the 1-Form*

$$(\frac{\partial f}{\partial r}, \frac{1}{r}\frac{\partial f}{\partial \phi}, \frac{\partial f}{\partial z})$$

express the gradient operator in cylindrical coordinates.

(*b*) *The gradient operator in the* $(\mathbf{e}_s, \mathbf{e}_n, \mathbf{e}_\theta)$ *coordinate system of* § *3(c)*

In the problem at hand a vector can be expressed by the unit vectors $(\mathbf{e}_s, \mathbf{e}_n, \mathbf{e}_\theta)$ and the definition of the coordinate transformation (3.23-3.25) yields

$$dx = a \cos \phi \ ds - (as + nbL) \sin \phi \ d\phi + bL \cos \phi \ dn,$$
$$dy = b \sin \phi \ ds + (bs + naL) \cos \phi \ d\phi + aL \sin \phi \ dn,$$
$$dz = L \ ds - ab \ dn,$$

and

$$\mathbf{e}_s = \frac{1}{\sqrt{S}} \begin{pmatrix} a \cos \phi \\ b \sin \phi \\ L \end{pmatrix} \Longrightarrow$$

$$\tilde{\omega}^s = \sqrt{S}[a \cos \phi \ dx + b \sin \phi \ dy + L \ dz]$$
$$= \sqrt{S}\left\{\left[a^2 \cos^2 \phi + b^2 \sin^2 \phi + L^2\right] ds + s\left[b^2 - a^2\right] \sin \phi \cos \phi \ d\phi\right\}, \tag{C 9}$$

$$\mathbf{e}_n = \frac{1}{\sqrt{N}} \begin{pmatrix} Lb \cos \phi \\ La \sin \phi \\ -ab \end{pmatrix} \Longrightarrow$$

$$\tilde{\omega}^n = \sqrt{N}[Lb \cos \phi \ dx - La \sin \phi \ dy - ab \ dz]$$
$$= \sqrt{N}\left\{nL^2\left[a^2 + b^2\right] \sin \phi \cos \phi \ d\phi + L^2\left[a^2 \sin^2 \phi + b^2 \cos^2 \phi + 1\right] dn\right\}, \tag{C 10}$$

$$\mathbf{e}_\theta = \frac{1}{\sqrt{\Theta}} \begin{pmatrix} a[b^2 + L^2] \sin \phi \\ -b[a^2 + L^2] \cos \phi \\ L[b^2 - a^2] \sin \phi \cos \phi \end{pmatrix} \Longrightarrow$$

$$\tilde{\omega}^\theta = \sqrt{\Theta}\left\{a[b^2 + L^2] \sin \phi \ dx - b[a^2 + L^2] \cos \phi \ dy + L[b^2 - a^2] \sin \phi \cos \phi \ dz\right\},$$
$$= -\sqrt{\Theta}\left\{a\left(b^2 + L^2\right)\left[as + nbL\right] \sin^2 \phi + b\left(a^2 + L^2\right)\left[bs + naL\right] \cos^2 \phi\right\} d\phi. \tag{C 11}$$

The 3×3 system for the unknown basis 1-Forms $(ds, dn, d\phi)$ can be solved for in terms of the dual basis $(\tilde{\omega}^s, \tilde{\omega}^n, \tilde{\omega}^\theta)$. In order to simplify the algebra we write

$$\tilde{\omega}^s = \omega_s^s \ ds + \omega_\phi^s \ d\phi + 0 \ dn, \tag{C 12}$$
$$\tilde{\omega}^n = 0 \ ds + \omega_\phi^n \ d\phi + \omega_n^n \ dn, \tag{C 13}$$
$$\tilde{\omega}^\theta = 0 \ ds + \omega_\phi^\theta \ d\phi + 0 \ dn, \tag{C 14}$$

where

$$\omega_s^s = \sqrt{S}\left[a^2 \cos^2 \phi + b^2 \sin^2 \phi + L^2\right],$$
$$\omega_\phi^s = \sqrt{S}s\left[b^2 - a^2\right] \sin \phi \cos \phi,$$

V. Theofilis

$$\omega_\phi^n = \sqrt{N}\, nL^2 \left[a^2 + b^2\right] \sin\phi\cos\phi,$$

$$\omega_n^n = \sqrt{N} L^2 \left[a^2 \sin^2\phi + b^2 \cos^2\phi + 1\right],$$

$$\omega_\phi^\theta = -\sqrt{\Theta}\Big\{a\left(b^2 + L^2\right)\left[as + nbL\right]\sin^2\phi + b\left(a^2 + L^2\right)\left[bs + naL\right]\cos^2\phi\Big\}.$$

The solution of system (C 12-C 14) is

$$ds = \frac{1}{\omega_s^s}\tilde\omega^s - \frac{\omega_\phi^s}{\omega_s^s \omega_\phi^\theta}\tilde\omega^\theta, \tag{C 15}$$

$$d\phi = \frac{1}{\omega_\phi^\theta}\tilde\omega^\theta, \tag{C 16}$$

$$dn = \frac{1}{\omega_n^n}\tilde\omega^n - \frac{\omega_\phi^n}{\omega_n^n \omega_\phi^\theta}\tilde\omega^\theta. \tag{C 17}$$

Rearranging the gradient operator (C 2)

$$df = (\partial f/\partial s)\ ds + (\partial f/\partial \phi)\ d\phi + (\partial f/\partial n)\ dn \tag{C 18}$$

by substituting (C 15-C 17) into (C 18) the gradient operator in the the coordinate system (s, n, θ) can be obtained,

$$df = \frac{1}{\omega_s^s}\frac{\partial f}{\partial s}\tilde\omega^s + \left[\frac{1}{\omega_\phi^\theta} - \frac{\omega_\phi^s}{\omega_s^s \omega_\phi^\theta} - \frac{\omega_\phi^n}{\omega_n^n \omega_\phi^\theta}\right]\frac{\partial f}{\partial \phi}\tilde\omega^\theta + \frac{1}{\omega_n^n}\frac{\partial f}{\partial n}\tilde\omega^n. \tag{C 19}$$

Appendix D. Iterative scheme for the leading eigenvalue

At a given streamwise position ζ_i equations (5.1–5.2) are discretised at the $(N+1)$ spectral collocation grid points yielding a linear inhomogeneous algebraic system which can be expressed in the form

$$AX = \underline{b} \Leftrightarrow \begin{bmatrix} A_1 & A_2 \\ A_3 & A_4 \end{bmatrix} \begin{bmatrix} \varphi \\ \tilde{p} \end{bmatrix} = \underline{b}, \tag{D 1}$$

where $\varphi = (\varphi_0, \varphi_1, ..., \varphi_N)^T$, $\tilde{p} = (\tilde{p}_0, \tilde{p}_1, ..., \tilde{p}_N)^T$. The Nth and $2N$th lines of matrix A are reserved for the boundary conditions. All but two elements of the vector b are zero. The nonzero elements appear at the Nth and $2N$th positions corresponding to the asymptotic values of φ and $\tilde{p}$ at the far-field position η_{max}, i.e., conditions (5.4–5.5).

Starting with a suitable initial guess of the required eigenvalue, the algebraic system (D 1) is solved iteratively, by means of a Newton iteration scheme [17], until the impermeability condition on the surface (i.e., $\varphi(0) = 0$) is satisfied. The above described scheme is able to perform temporal as well as spatial instability calculations giving spectrally accurate results at the same level of computing effort. A similar iterative scheme was proposed by Malik [19] for the solution of viscous, compressible instability equations on a real grid. Standard numerical library subroutines were used for the solution of the linear system (D 1) and the evaluation of the modified Bessel functions. The non-zero elements of the submatrices A_1, A_2, A_3 and A_4 of the system (D 1) are

$$A_{1_{jk}} = D_{jk} + \frac{\zeta_i}{1 + \lambda\zeta_i^2 + \zeta_i\eta_j} - \frac{W_{0\eta_j}}{W_{0_j} - \beta}, \tag{D 2}$$

$$A_{2_{jk}} = \frac{-iT_{0_j}}{\gamma M_\infty^2(W_{0_j} - \beta)} \left[1 + \frac{n^2\zeta_i^2}{\alpha^2(1 + \lambda\zeta_i^2 + \zeta_i\eta_j)^2} \right] - \frac{i(W_{0_j} - \beta)}{\gamma}, \tag{D 3}$$

$$A_{3_{jk}} = \frac{i\alpha^2(W_{0_j} - \beta)}{T_{0_j}}, \tag{D 4}$$

$$A_{4_{jk}} = \frac{D_{jk}}{(\gamma M_\infty^2)}, \tag{D 5}$$

for $j = k$, and

$$A_{1_{jk}} = D_{jk}, \tag{D 6}$$

$$A_{4_{jk}} = \frac{D_{jk}}{(\gamma M_\infty^2)}, \tag{D 7}$$

for $j \neq k$, where $j, k = 0, 2, ..., N$. The elements of vector $\underline{b}$ are given by

$$b_j = 0, \quad \text{if} \quad j \neq N \quad \text{and} \quad j \neq 2N, \tag{D 8}$$

$$b_N = \frac{1}{2}[K_{n+1}(\hat{\eta}_i) + K_{|n-1|}(\hat{\eta}_i)], \tag{D 9}$$

$$b_{2N} = \mp \frac{M_\infty^2 i\alpha\gamma(1-\beta)K_n(\hat{\eta}_i)}{[1 - M_\infty^2(1-\beta^2)]^{1/2}}, \tag{D 10}$$

where

$$\hat{\eta}_i = \pm\alpha[1 - M_\infty^2(1-\beta^2)]^{1/2}(1/\zeta_i + \lambda\zeta_i + \eta_{max}),$$

and $j, k = 0, 2, ..., 2N$.

References

1. J. P. Boyd. Complex coordinate methods for hydrodynamic instabilities and Sturm-Liouville eigenproblems with an interior singularity. *J. Comp. Phys.*, 57:454–471, 1985.

2. J. P. Boyd and Z. D. Christidis. Low wavenumber instability on the equatorial beta-plane. *Geophys. Res. Letters*, 9(7):769–772, 1982.

3. W. L. Burke. *Applied differential geometry*. Cambridge University Press, 1989.

4. C. Canuto, M. Y. Hussaini, A. Quarteroni, and T. A. Zang. *Spectral methods in fluid dynamics*. Springer, 1987.

5. T. Colonius. An overview of simulation, modeling and active control of flow/acoustic resonance in open cavities. Technical Report 01-0076, AIAA, 2001. (invited).

6. T. Corke. In S. Walker, editor, *AFOSR Contractors' Meeting in Unsteady Aerodynamics and Hypersonics*, Wright-Patterson AFB, Dayton OH, 1999.

7. J. Dongarra, B. Straughan, and D. Walker. Chebyshev tau - QZ algorithm methods for calculating spectra of hydrodynamic stability problems. *J. Appl. Num. Math.*, 22:399 – 435, 1996.

8. P. W. Duck. The inviscid axisymmetric stability of the supersonic flow along a circular cylinder. *J. Fluid Mech.*, 214:611–637, 1990.

9. P. W. Duck and S. J. Shaw. The inviscid stability of supersonic flow past a sharp cone. *Theoret. Comput. Fluid Dynamics*, 2:139–163, 1990.

10. A. W. Gill and G. E. Sneddon. Complex mapped matrix methods in hydrodynamic stability problems. *J. Comp. Phys.*, 122:13–24, 1995.

11. E. Heil. *Differentialformen und Anwendung auf Vektoranalysis, Differentialgleichungen, Geometrie*. BI Wissenschaftsverlag, Zürich, 1974.

12. M. Huntley, A. J. Smits, P. Wu, and R. Miles. Mhz rate imaging of boundary-layer transition on elliptic cones at mach 8. In S. Walker, editor, *AFOSR Contractors' Meeting in Unsteady Aerodynamics and Hypersonics*, Wright-Patterson AFB, Dayton OH, 1999.

13. A. Karabis, V. Theofilis, and S. J. S. SJ. On the inviscid spatial instability of supersonic boundary layer flow along bodies of revolution. *Comp. Fluids*, (submitted), 2000.

14. G. E. Karniadakis and S. J. Sherwin. *Spetral/hp element methods for computational fluid dynamics*. Oxford University Press, 1999.

15. R. L. Kimmel, M. A. Klein, and S. N. Schwoerke. Three-dimensional hypersonic laminar boundary layer computations for transition experiment design. *J. of Spacecrafts and Rockets*, 34:409–415, 1997.

16. R. L. Kimmel, J. Poggie, and S. N. Schwoerke. Laminar-turbulent transition in a mach 8 elliptic cone flow. *AIAA J.*, 37 (9):1080–1087, 1999.

17. L. M. Mack. Boundary layer linear stability theory. In *AGARD Report No. 709, Special course on stability and transition of laminar flow*, pages 3–1 – 3–81, 1984.

18. L. M. Mack. Review of linear compressible stability theory. In D. L. Dwoyer and M. Y. Hussaini, editors, *Stability of time depependent and spatially varying flows. ICASE Workshop on the Stability of Time Dependent and Spatially Varying Flows*, pages 164–187, New York, 1987. Springer.

19. M. R. Malik. Numerical methods for hypersonic boundary layer stability. *J. Comp. Phys.*, 86:376–413, 1991.

20. C. D. Pruett and C. L. Street. A spectral collocation method for compressible, non-similar boundary layers. *Int. J. Num. Meth. Fluids*, 13:713–727, 1991.

21. K. F. Stetson and R. L. Kimmel. On hypersonic boundary-layer stability. Technical Report 92-0737, AIAA, 1992.

22. T. Tatsumi and T. Yoshimura. Stability of the laminar flow in a rectangular duct. *J. Fluid Mech.*, 212:437–449, 1990.

23. V. Theofilis. The discrete temporal eigenvalue spectrum of the generalized Hiemenz flow as solution of the orr-sommerfeld equation. *J. Eng. Math.*, 28:241–259, 1994.

24. V. Theofilis. On globally unstable basic flows in open cavities. Technical Report 00-1965, AIAA,

2000.

25. V. Theofilis. On steady laminar basic flows and their global eigenmodes: An elliptic cone in compressible flow. Technical Report F61775-99-WE049, EOARD, 2000.

26. V. Theofilis. Advances in global linear theory for nonparallel flows. *Progress in Aerospace Sciences*, page (to appear), 2001.

27. V. Theofilis. Advances in global linear instability theory. *Prog. Aero. Sci.*, 2001 in preparation.

28. V. Theofilis, S. Hein, and U. C. Dallmann. On the origins of unsteadiness and three-dimensionality in a laminar separation bubble. *Phil. Trans. Roy. Soc. London (A)*, 358:3229–3246, 2000.

29. X. Zhong. High-order finite-difference schemes for numerical simulation of hypersonic boundary-layer transition. *J. Comput. Phys.*, 144:662–709, 1998.

30. X. Zhong. DNS of boundary-layer receptivity to freestream sound for hypersonic flows over blunt elliptical cones. In H. Fasel and W. S. Saric, editors, *IUTAM Symposium on Laminar-Turbulent Transition V*, 1999.

N	$\delta_2 = 0$	$\delta_2 = 0.05$	$\delta_2 = 0.1$	$\delta_2 = 0.15$
	c	c	c	c
48	0.856328 +i 0.000000	0.856333 +i 0.000418	0.856129 +i 0.000355	0.855075 −i 0.000462
64	0.856543 +i 0.000000	0.856357 +i 0.000407	0.856382 +i 0.000395	0.856723 −i 0.000134
80	0.856937 +i 0.000000	0.856356 +i 0.000408	0.856354 +i 0.000412	0.856228 +i 0.000550
96	0.857174 +i 0.001755	0.856356 +i 0.000408	0.856356 +i 0.000408	0.856324 +i 0.000356

Table 1. Dependence of the eigenvalue c on the number of collocation nodes and the complex mapping parameter δ_2 in the case of planar, compressible, adiabatic flow for $\alpha = 0.365$ (mode II) and $M_\infty = 3.8$.

N	η_{max}	l	δ_1	Mode I $\omega = 0.0386$, $n = 3$	Mode II $\omega = 0.334$, $n = 0$
				α	α
32	25	25	−0.05	0.050338 −i 0.003137	0.367236 −i 0.004590
64	25	25	−0.05	0.050338 −i 0.003137	0.366888 −i 0.004487
80	25	25	−0.05	0.050339 −i 0.003136	0.366903 −i 0.004485
96	25	25	−0.05	0.050339 −i 0.003136	0.366903 −i 0.004485
80	40	40	−0.04	0.050339 −i 0.003136	0.366905 −i 0.004483
90	60	60	−0.04	0.050339 −i 0.003136	0.366902 −i 0.004483

Table 2. Dependence of the eigenvalues on the number of collocation nodes and the mappings parameters, for the case of adiabatic cone flow with $M_\infty = 3.8$ and $\lambda = 1$, at $\zeta = 0.05$.

$N\xi$	$N\eta$	$f_{\mathrm{H}}(x = a, y = 0)$	$f_{\mathrm{S}}(x = a, y = 0)$	$f_{\mathrm{A}}(x = a, y = 0)$
10	10	-0.901970	-1.360926	-0.863940
20	20	-0.901970	-1.367825	-0.867146
40	40	-0.901970	-1.375666	-0.868566
80	80	-0.901970	-1.375823	-0.868586

Table 3. Convergence history of numerical solution of the Poisson problems H, S and A, subject to homogeneous Neumann boundary conditions. $N\xi$ and $N\eta$ respectively denote the number of collocation points along the ξ and η coordinate directions.
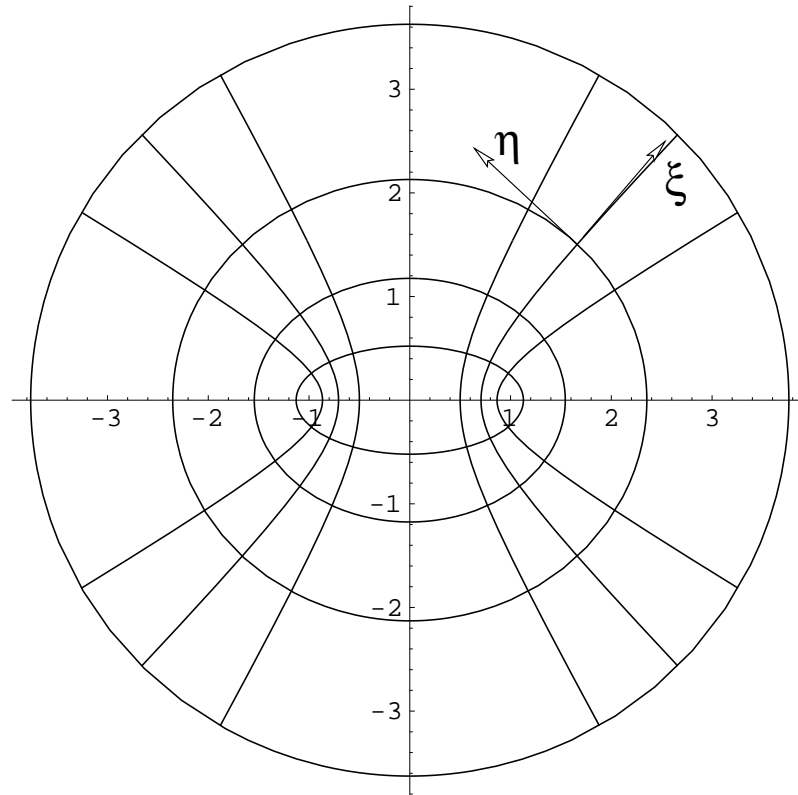
Figure 1. The confocal elliptical coordinate system $O\xi\eta$.

V. Theofilis
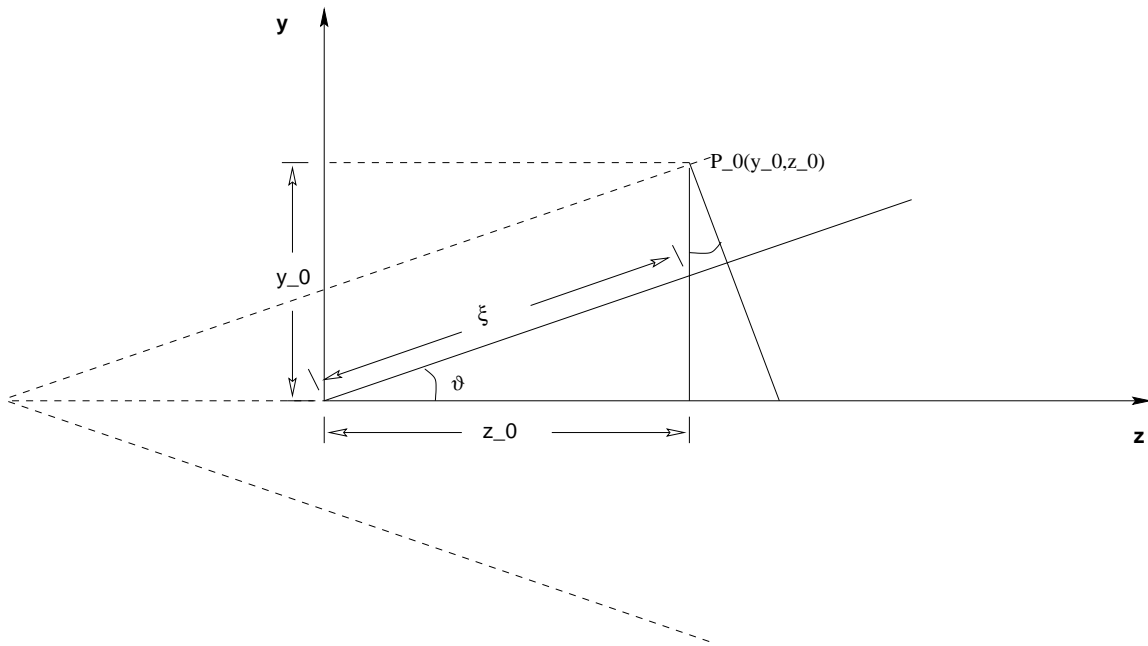
Figure 2. Projection of the coordinates on the plane $x = 0$
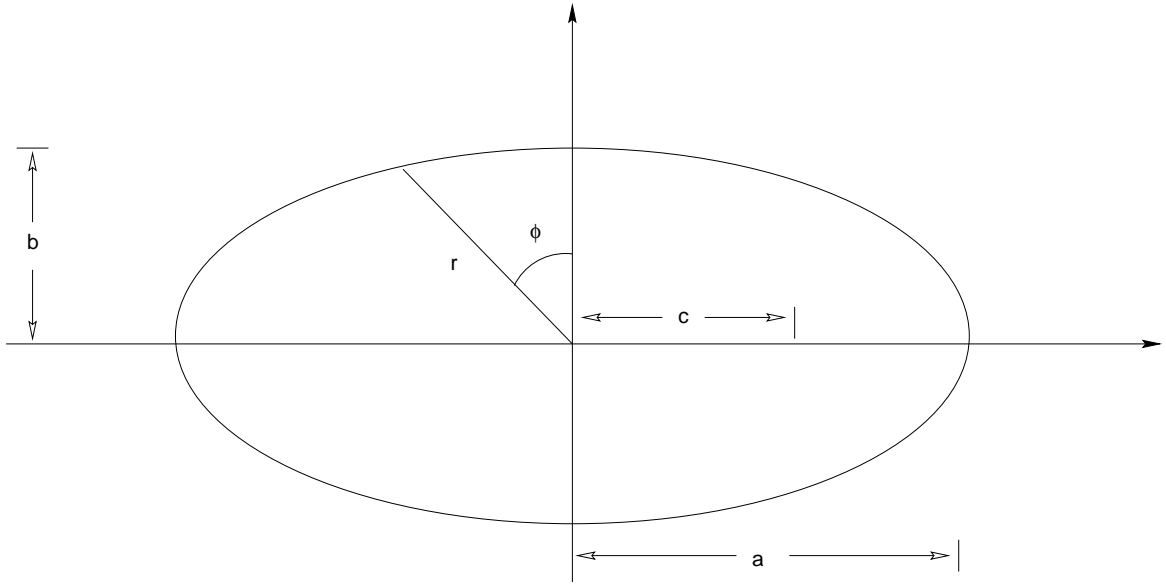
Figure 3. Projection of the coordinates on the plane $z = cnst.$
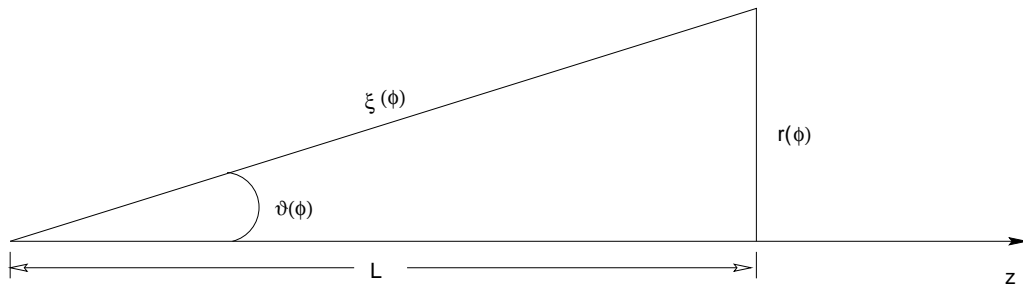
Figure 4. An arbitrary location $\vartheta(\phi)$.
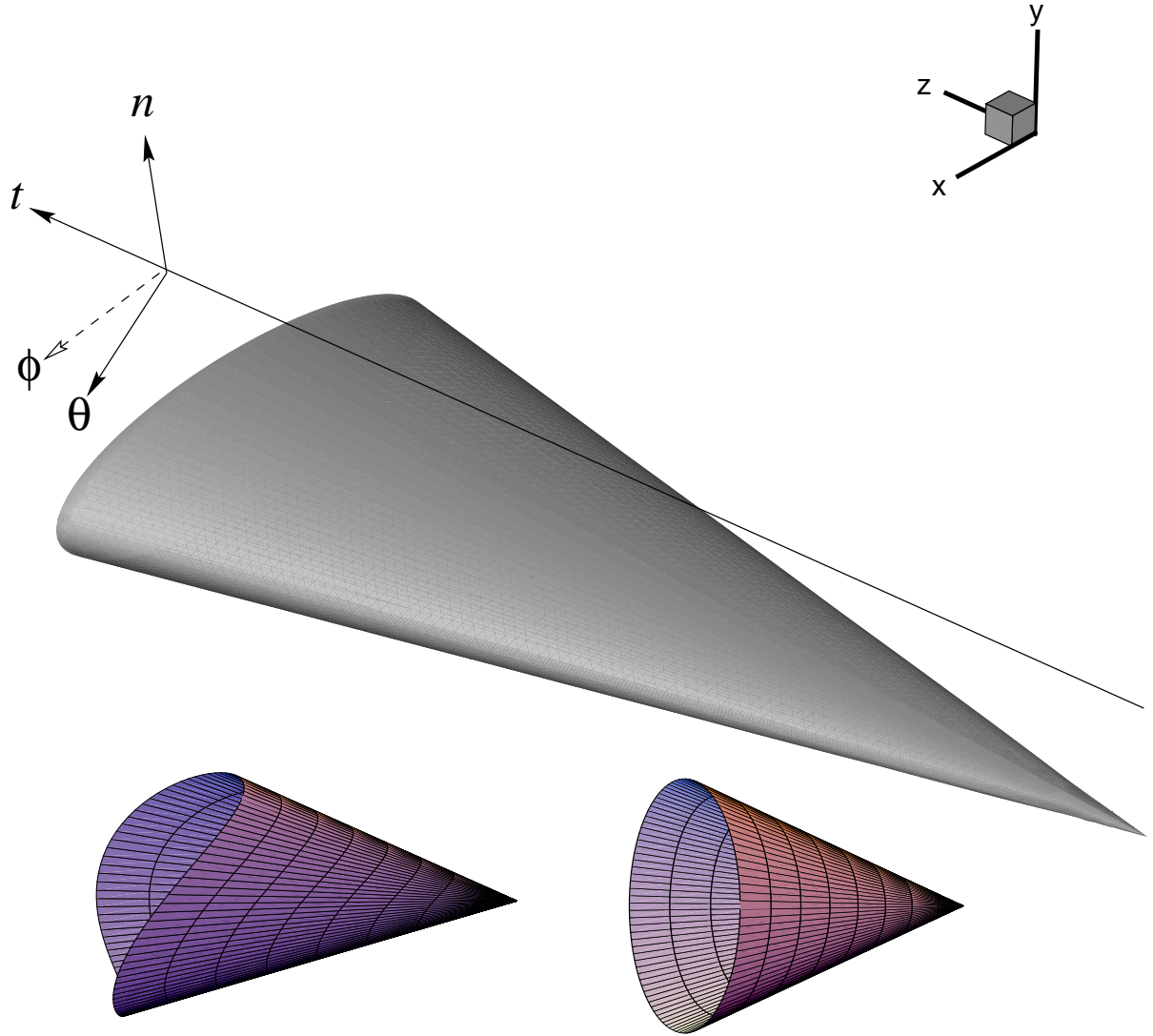
Figure 5. One orthogonal body-fitted coordinate system which defines the $On\theta$ plane on which a global instability analysis can be performed.

V. Theofilis
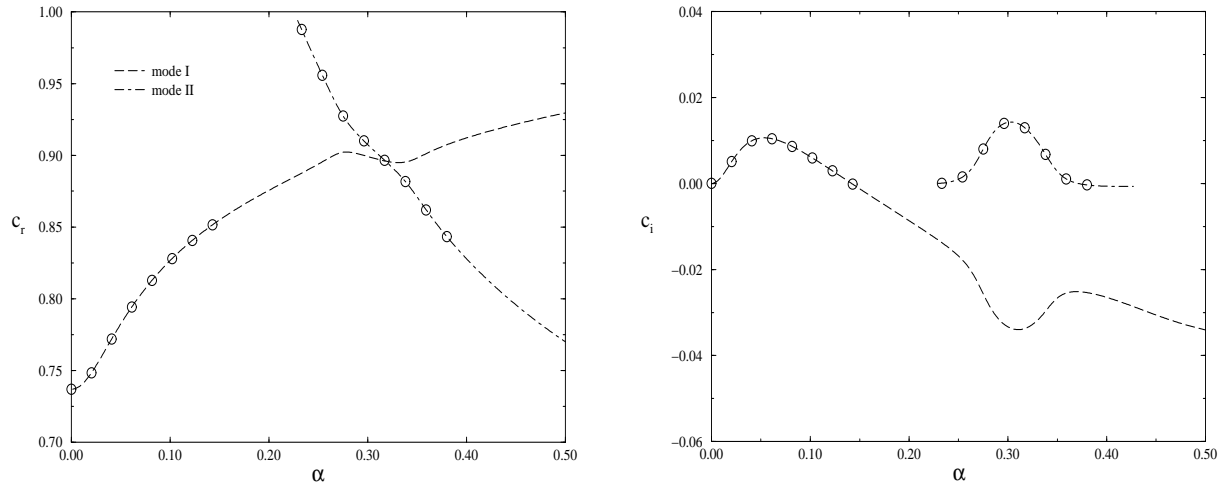
Figure 6. Frequencies c_r and growth rates c_i of mode I (dashed) and II (dash–dotted) instabilities as function of the wavenumber α in $M_\infty = 3.8$ boundary-layer flow over an insulated flat plate. Superimposed, denoted by open symbols, are the results of [8].
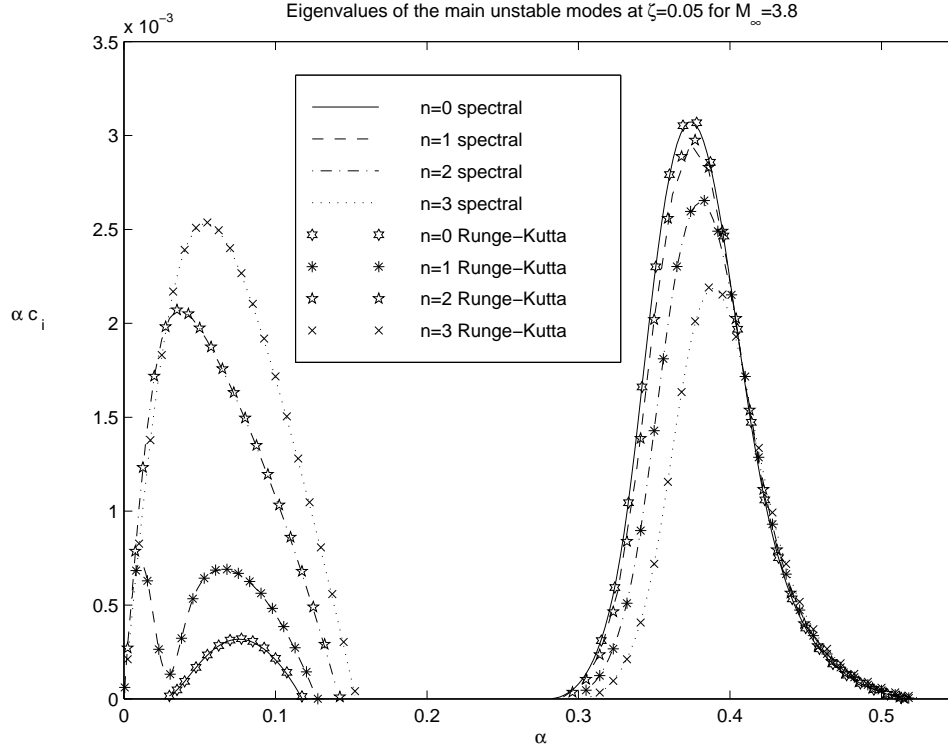
Figure 7. Temporal instability results. Distribution of the temporal growth rate αc_i with α for modes I and II, $\zeta = 0.05$ and various azimuthal wavenumbers. For comparison, the results of [9] are also shown indicated by symbols.
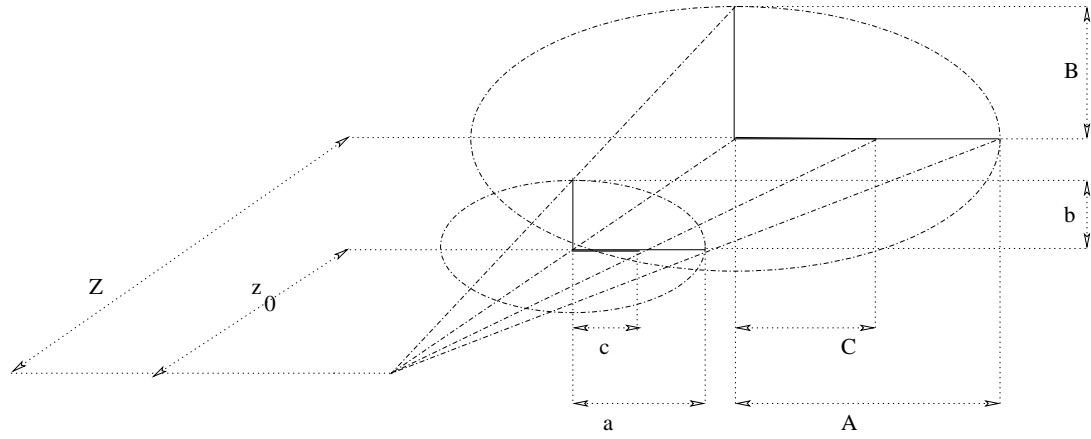
Figure 8. Calculation of geometric parameters on the instability analysis plane

Figure 9. The structure of the matrix discretizing the spatial eigenvalue problem
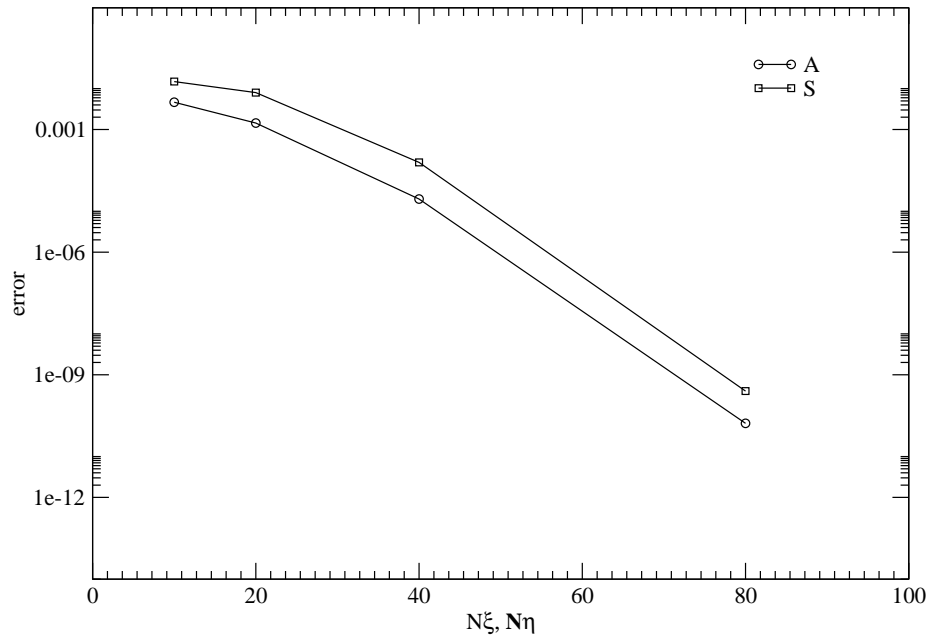
Figure 10. Convergence of the numerical solution of the Poisson problems S and A on the elliptic confocal grid
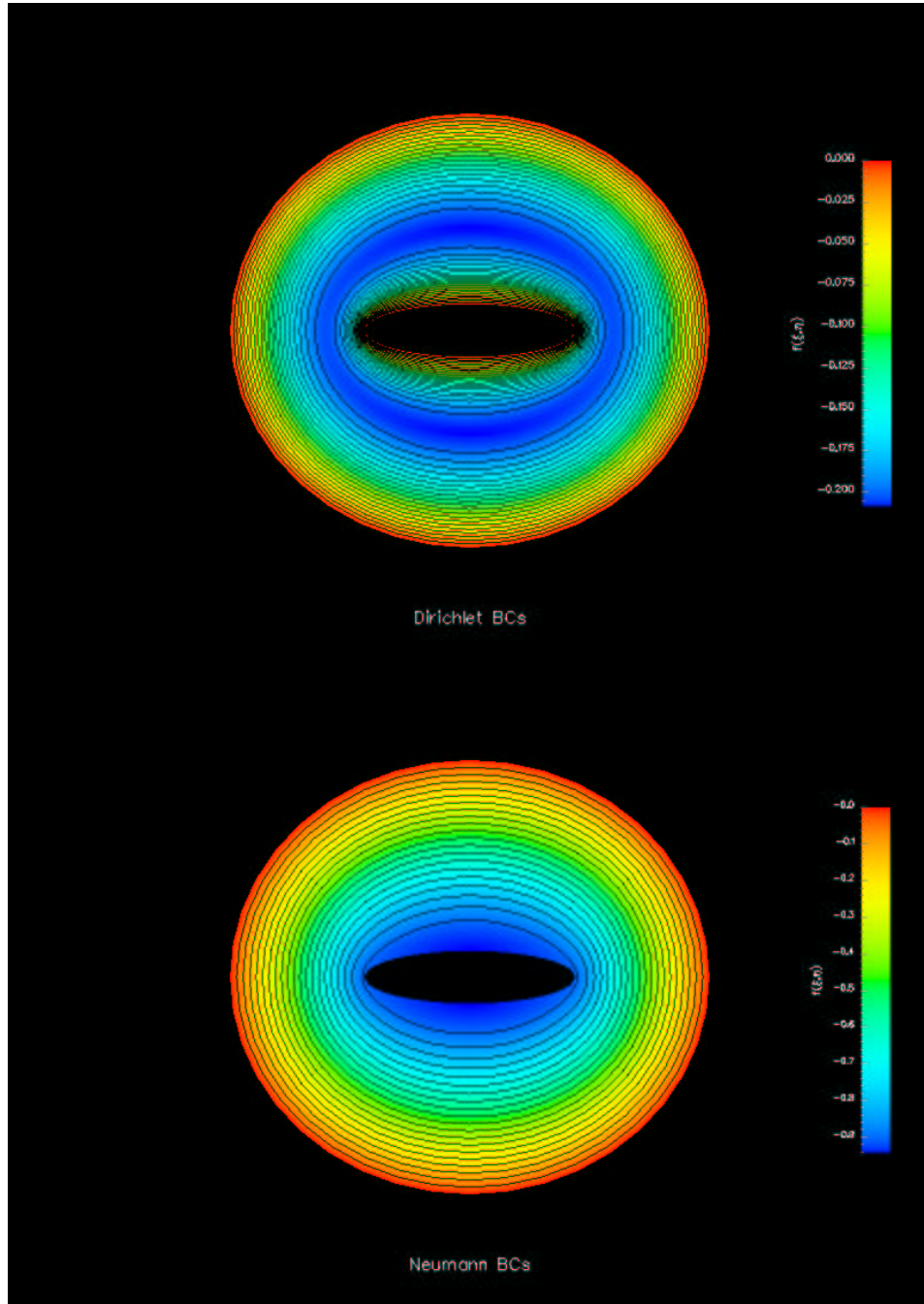
Figure 11. Numerical solution of the Poisson problem (6.1) using (6.3). Upper: $f(\xi = \xi_w, \eta) = 0$; lower: $f_\xi(\xi = \xi_w, \eta) = 0$.
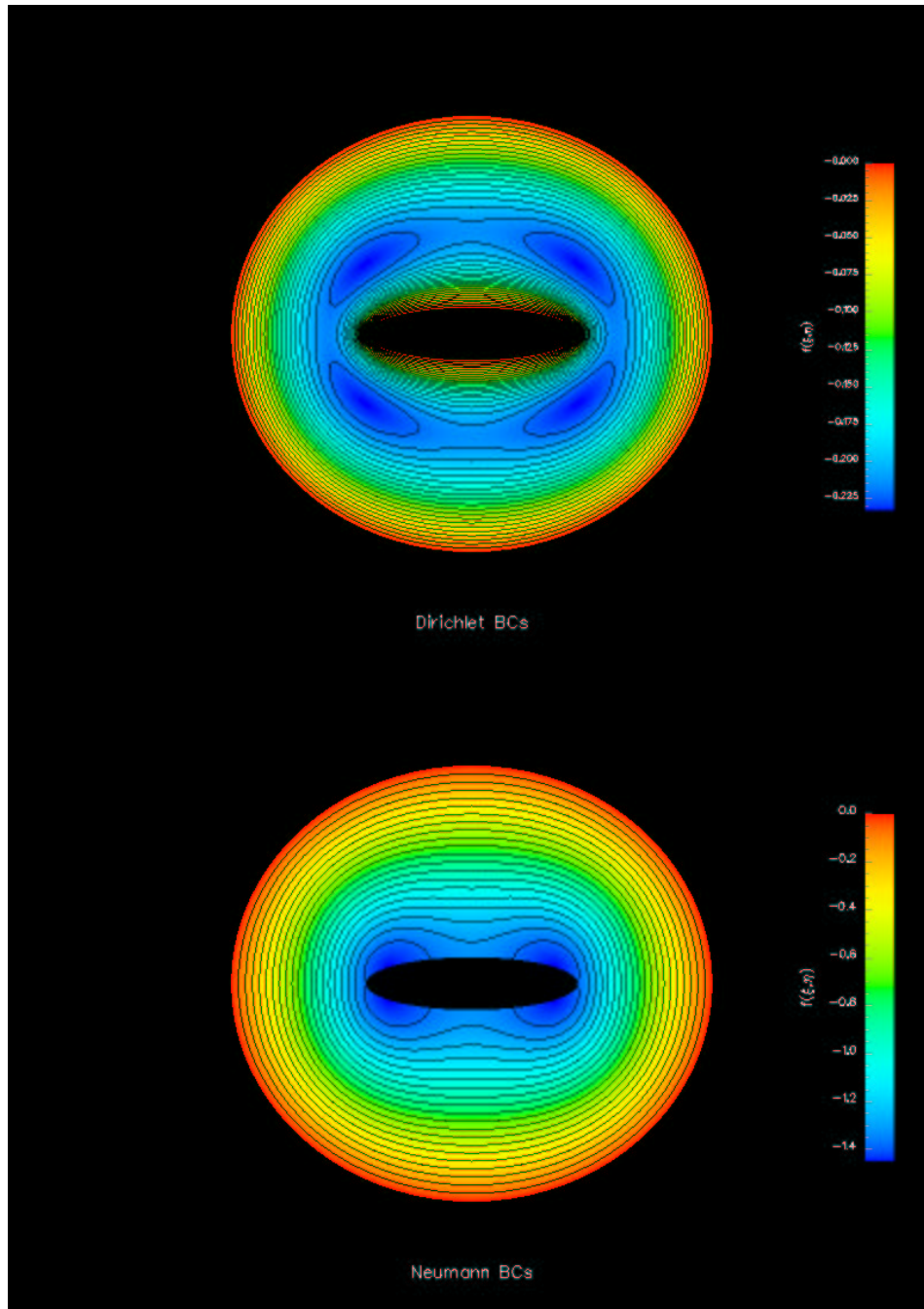
Figure 12. Numerical solution of the Poisson problem (6.1) using (6.4). Upper: $f(\xi = \xi_w, \eta) = 0$; lower: $f_\xi(\xi = \xi_w, \eta) = 0$.
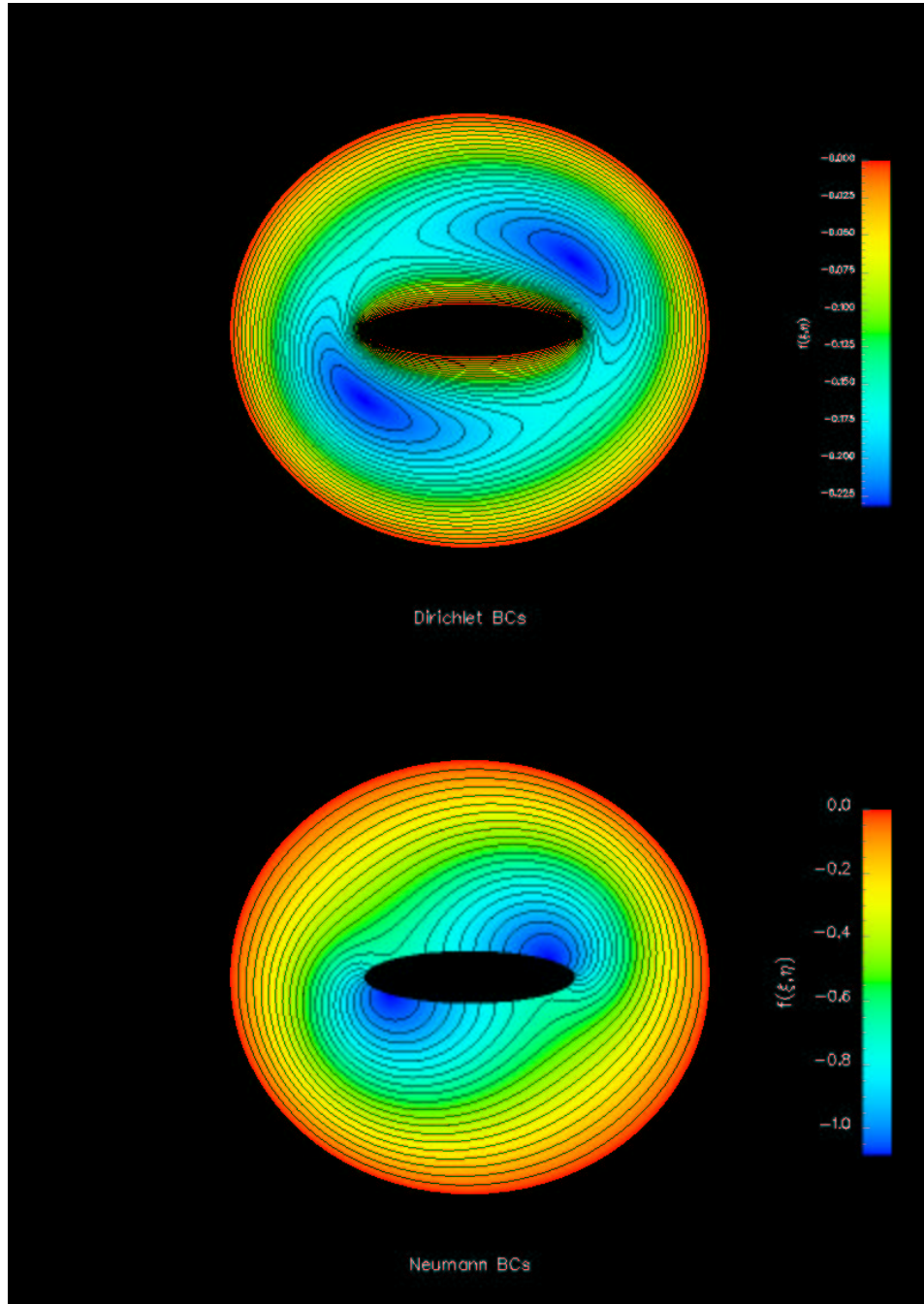
Figure 13. Numerical solution of the Poisson problem (6.1) using (6.5). Upper: $f(\xi = \xi_w, \eta) = 0$; lower: $f_\xi(\xi = \xi_w, \eta) = 0$.
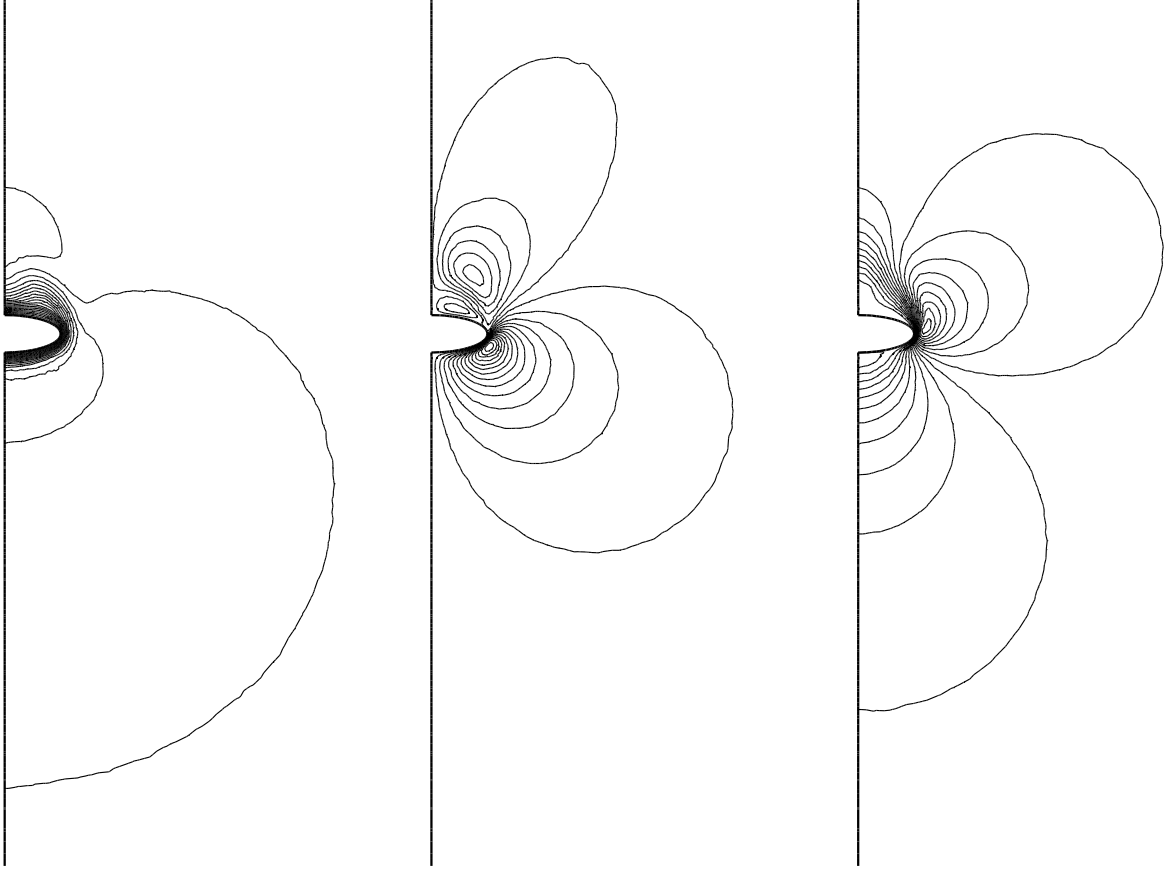
Figure 14. A qualitative view of the basic flow velocity components at $M = 0.5[25]$; from left to right, $\bar{w}, \bar{v}, \bar{u}$.
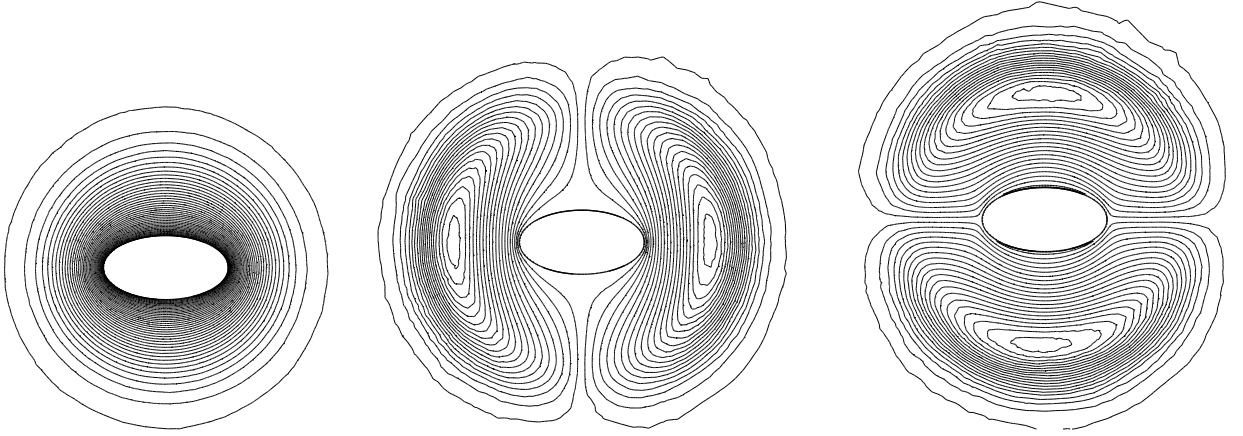
Figure 15. A qualitative view of the basic flow velocity components at $M = 8.0[25]$; from left to right, $\bar{w}, \bar{v}, \bar{u}$.
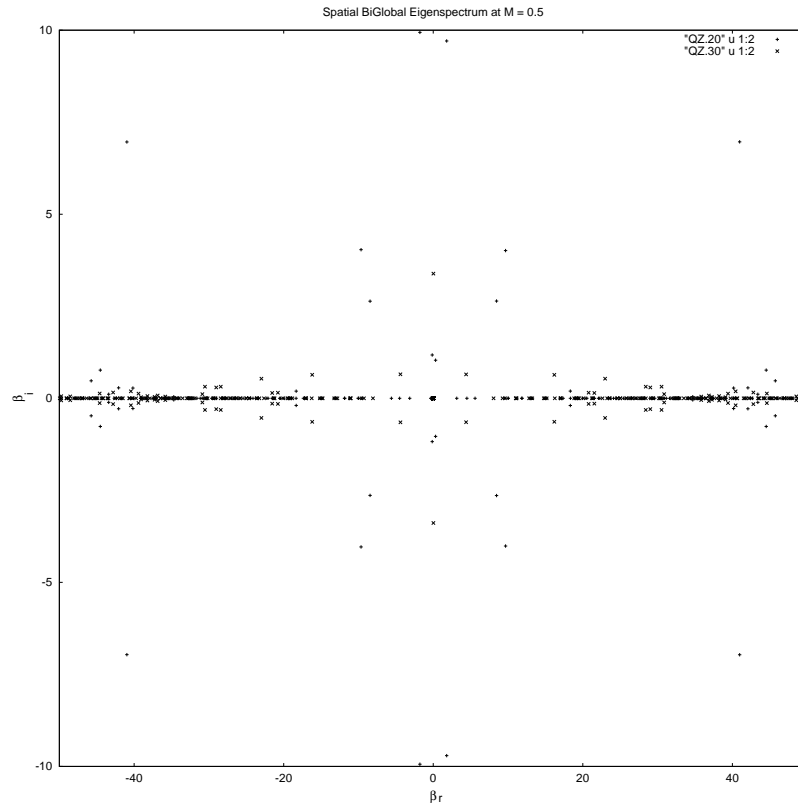
Figure 16. Eigenvalue spectra at $M = 0.5$ and resolutions 20×20 and 30×30
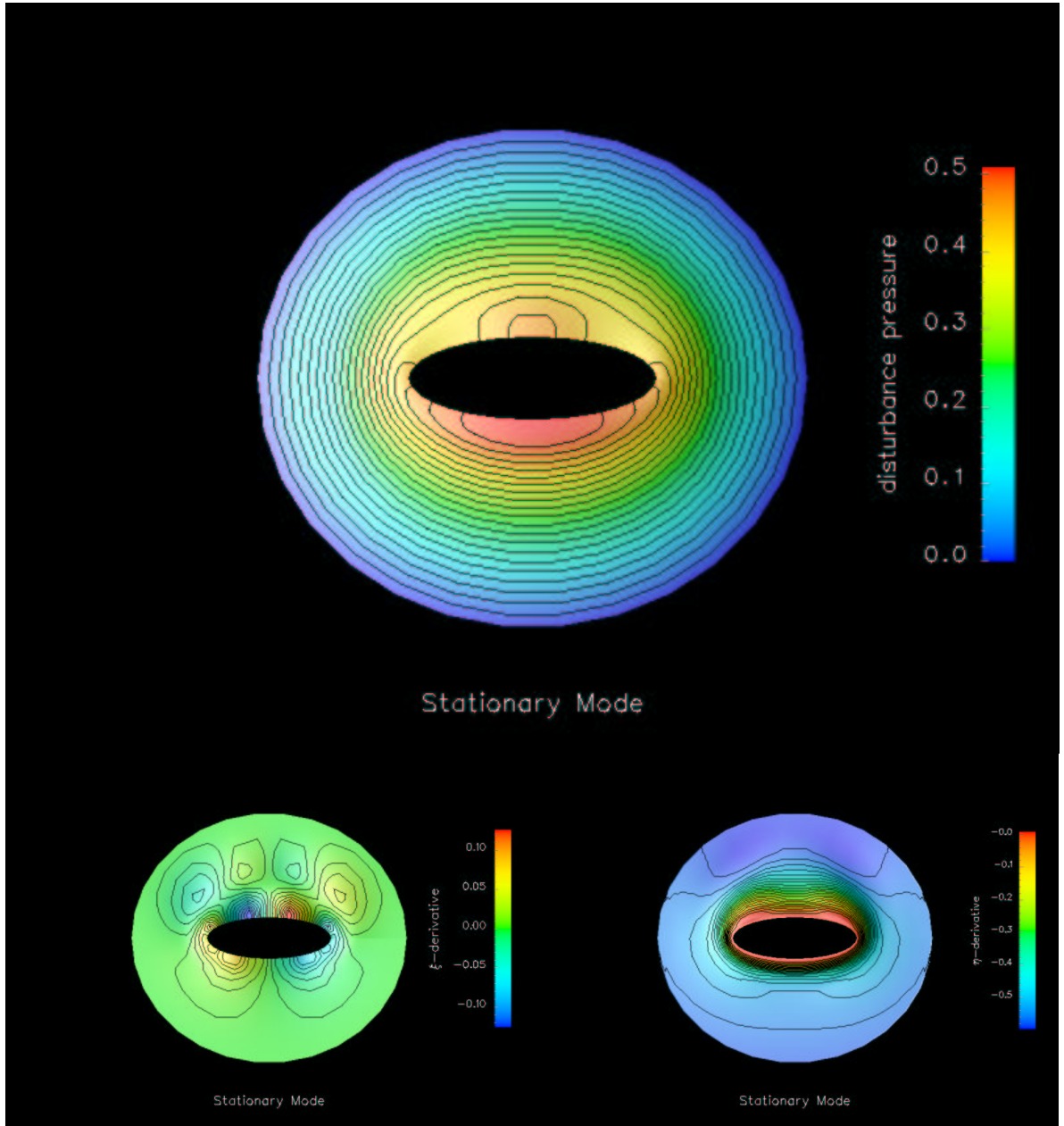
Figure 17. A stationary mode at $M = 0.5$. Upper $\hat{p}$, lower left $\hat{p}_\xi$, lower right $\hat{p}_\eta$.
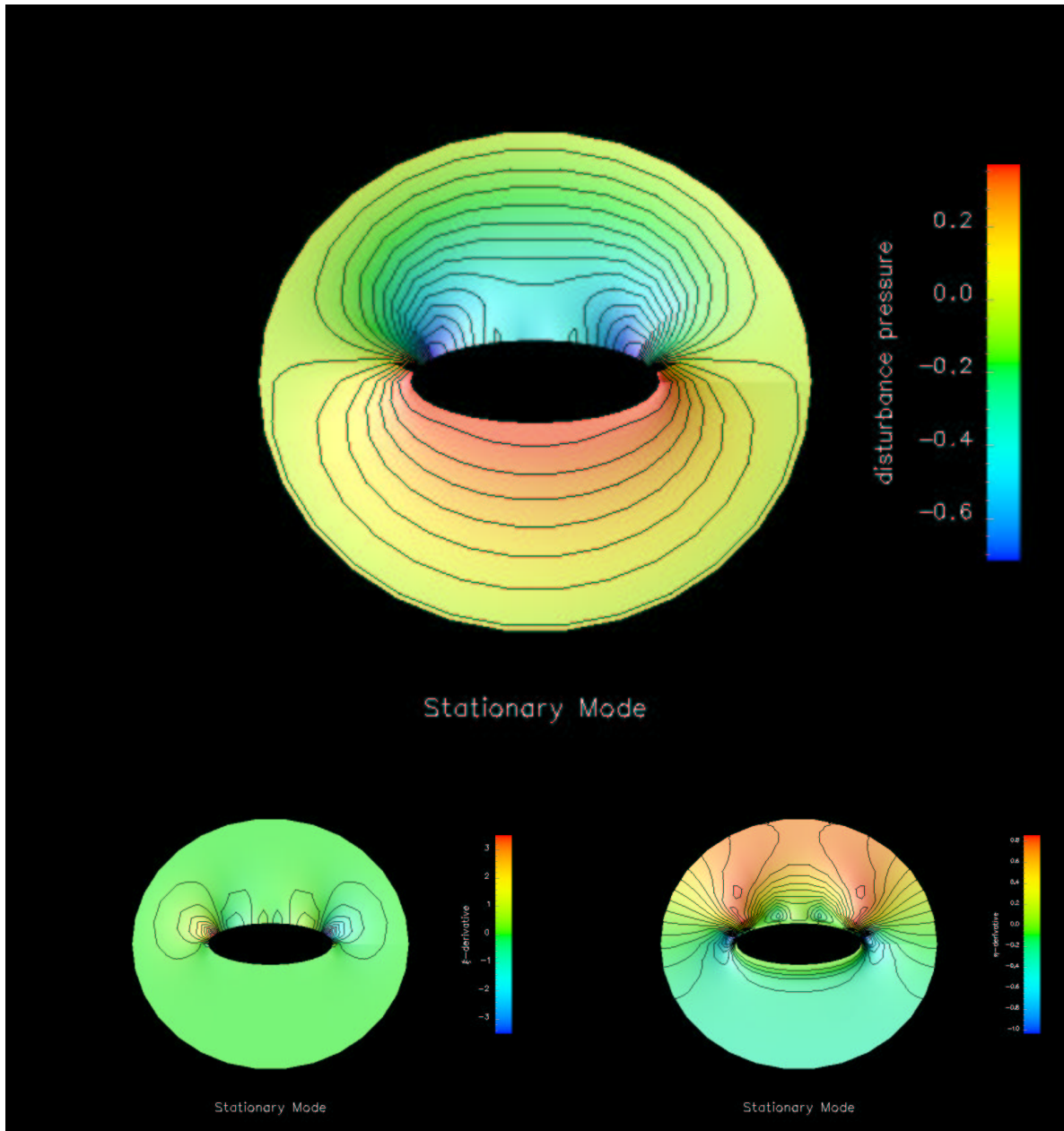
Figure 18. A stationary mode at $M = 0.5$. Upper $\hat{p}$, lower left $\hat{p}_\xi$, lower right $\hat{p}_\eta$.
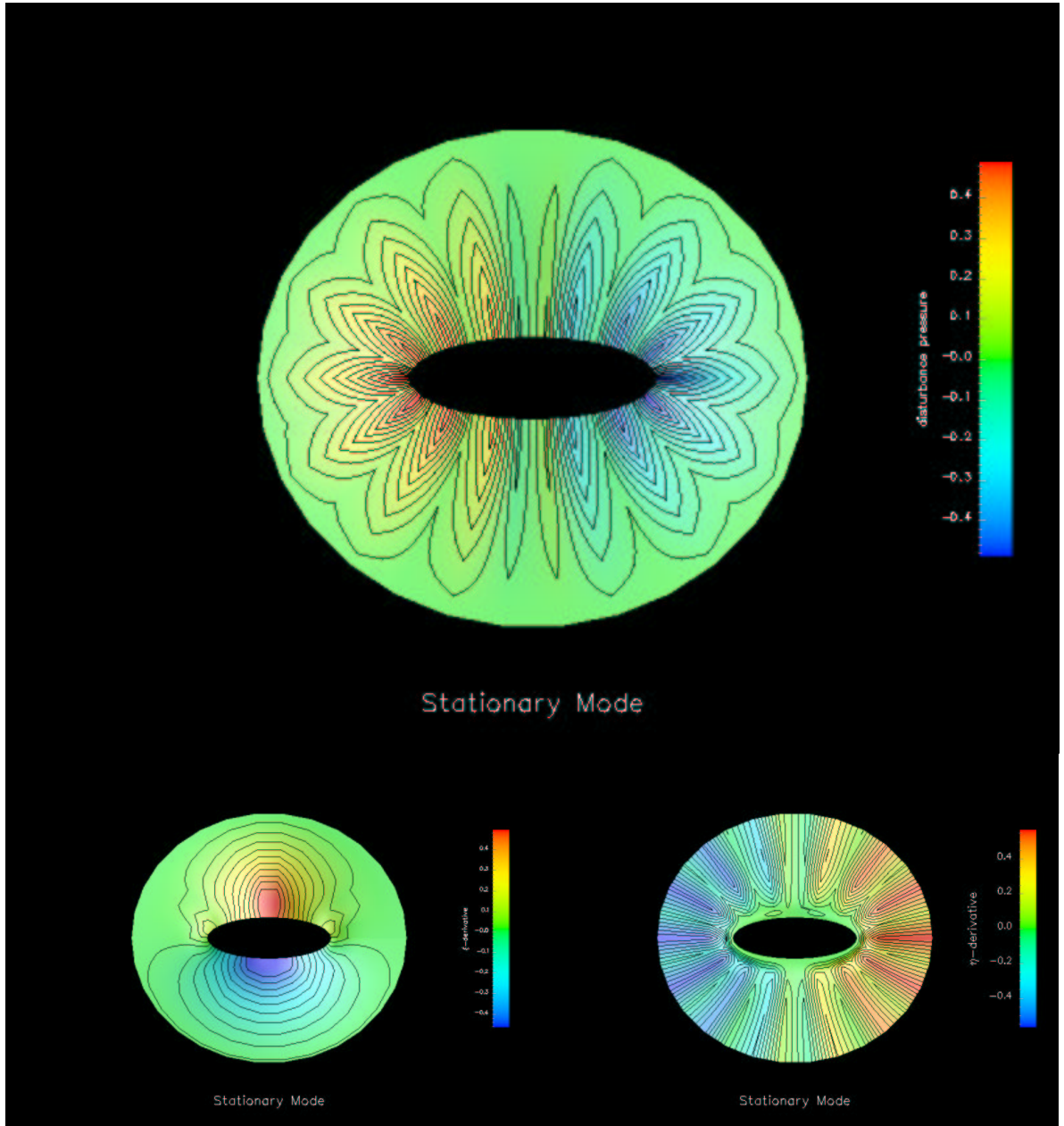
Figure 19. A stationary mode at $M = 0.5$. Upper $\hat{p}$, lower left $\hat{p}_\xi$, lower right $\hat{p}_\eta$.
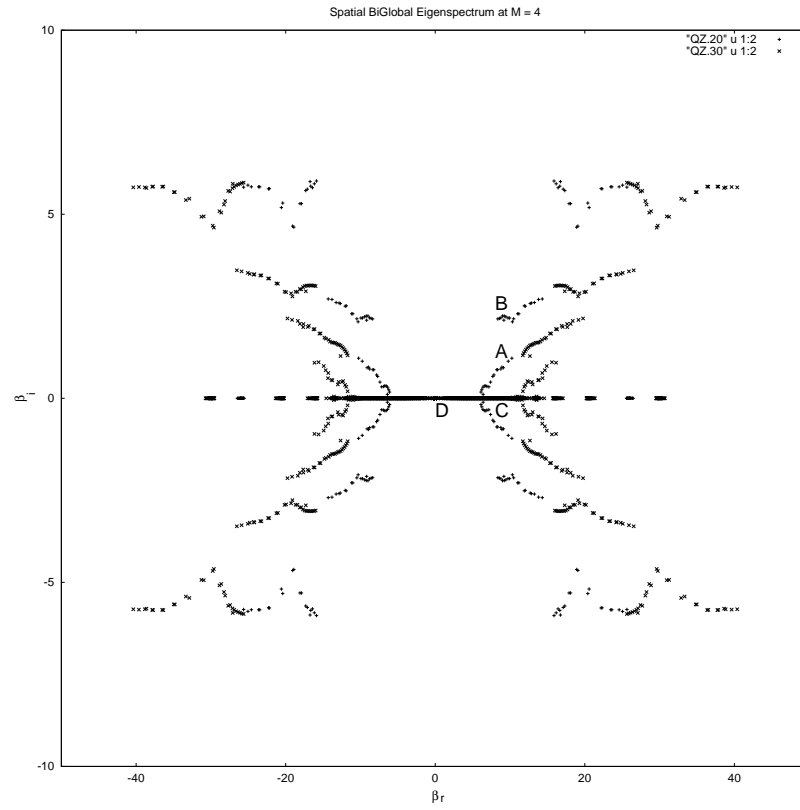
Figure 20. Eigenvalue spectra at $M = 4$ and resolutions 20×20 and 30×30
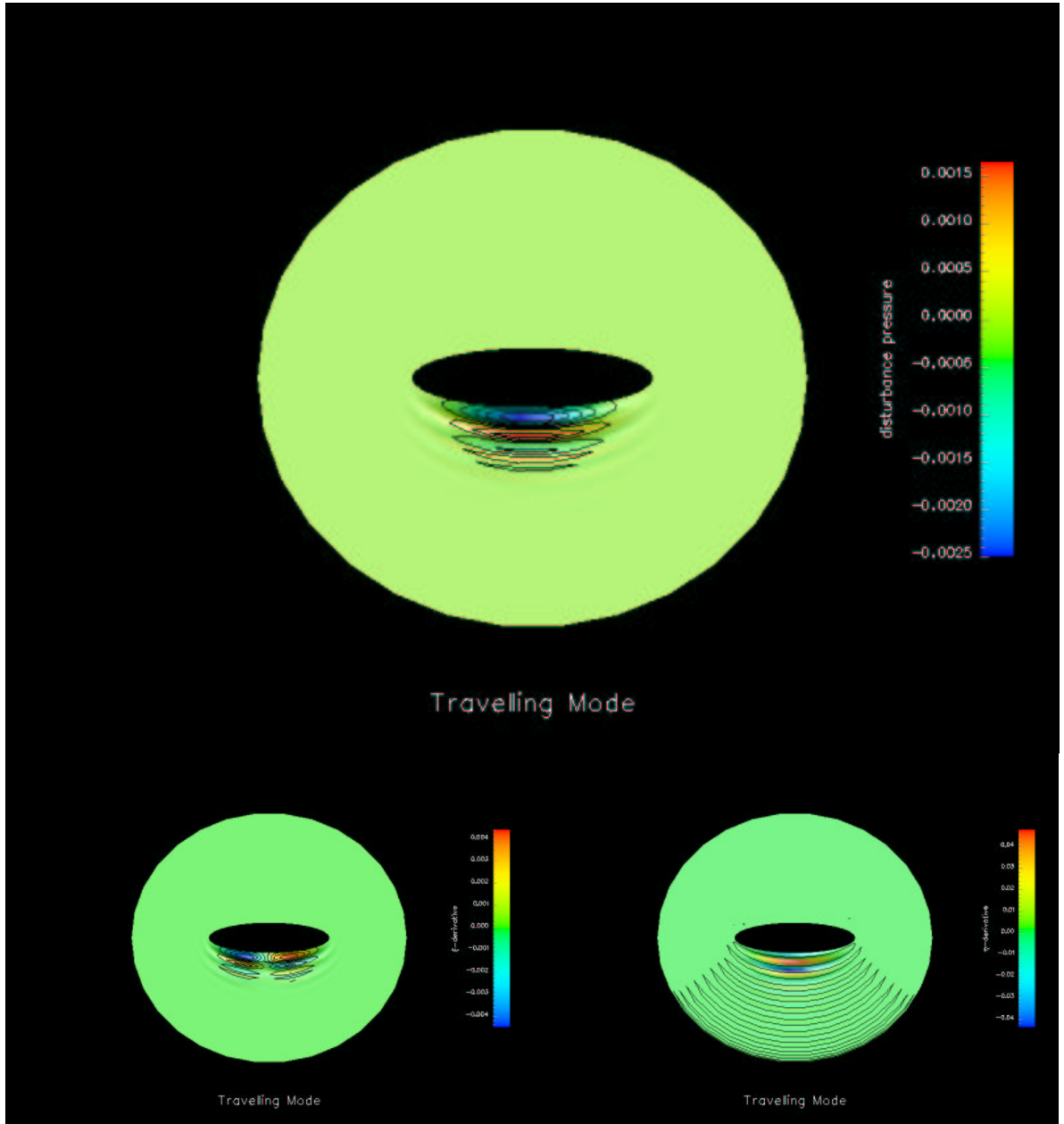
Figure 21. A travelling mode - member of family A - at $M = 4.0$. Upper $\hat{p}$, lower left $\hat{p}_\xi$, lower right $\hat{p}_\eta$.
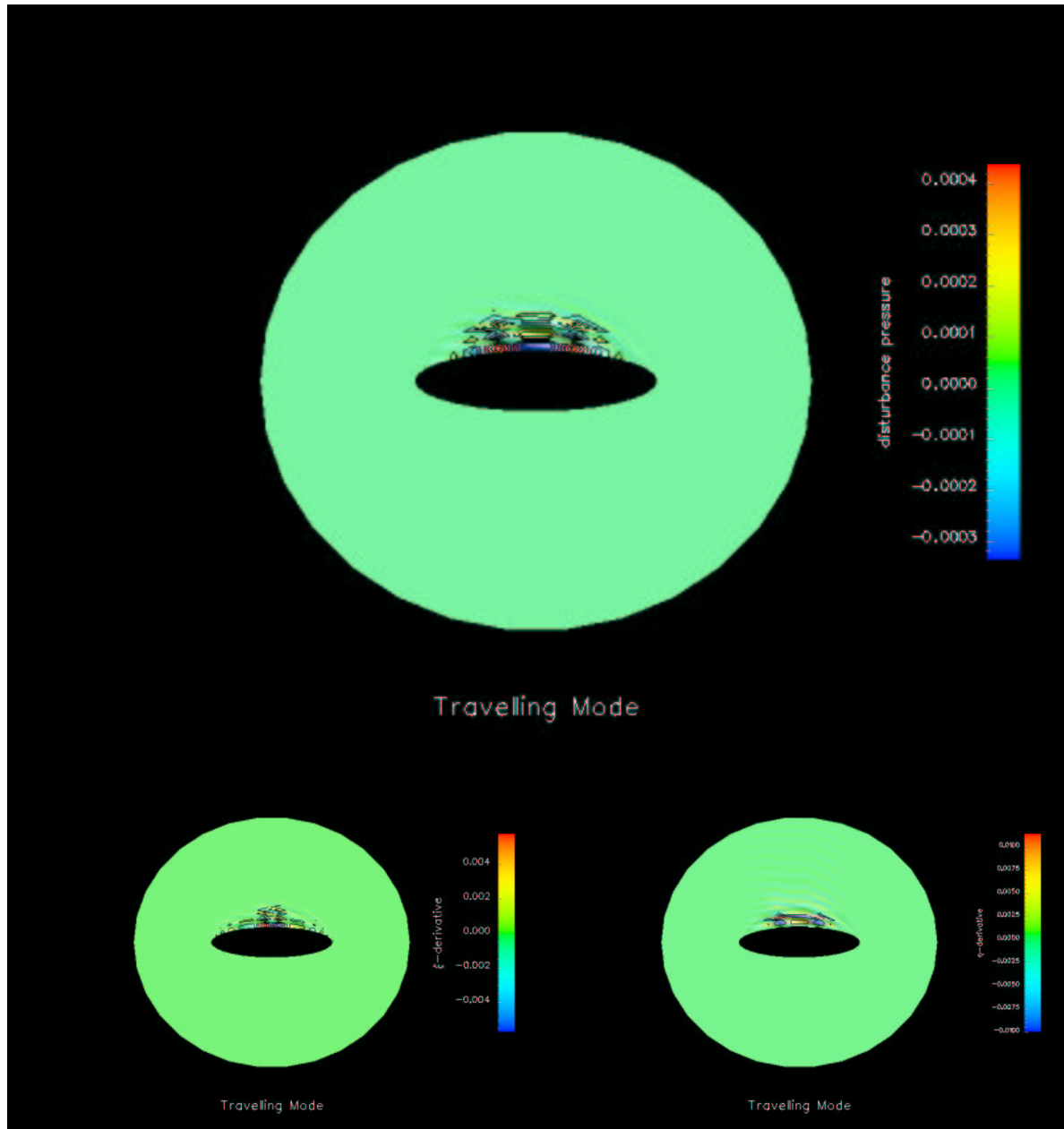
Figure 22. A travelling mode - member of family B - at $M = 4.0$. Upper $\hat{p}$, lower left $\hat{p}_\xi$, lower right $\hat{p}_\eta$.
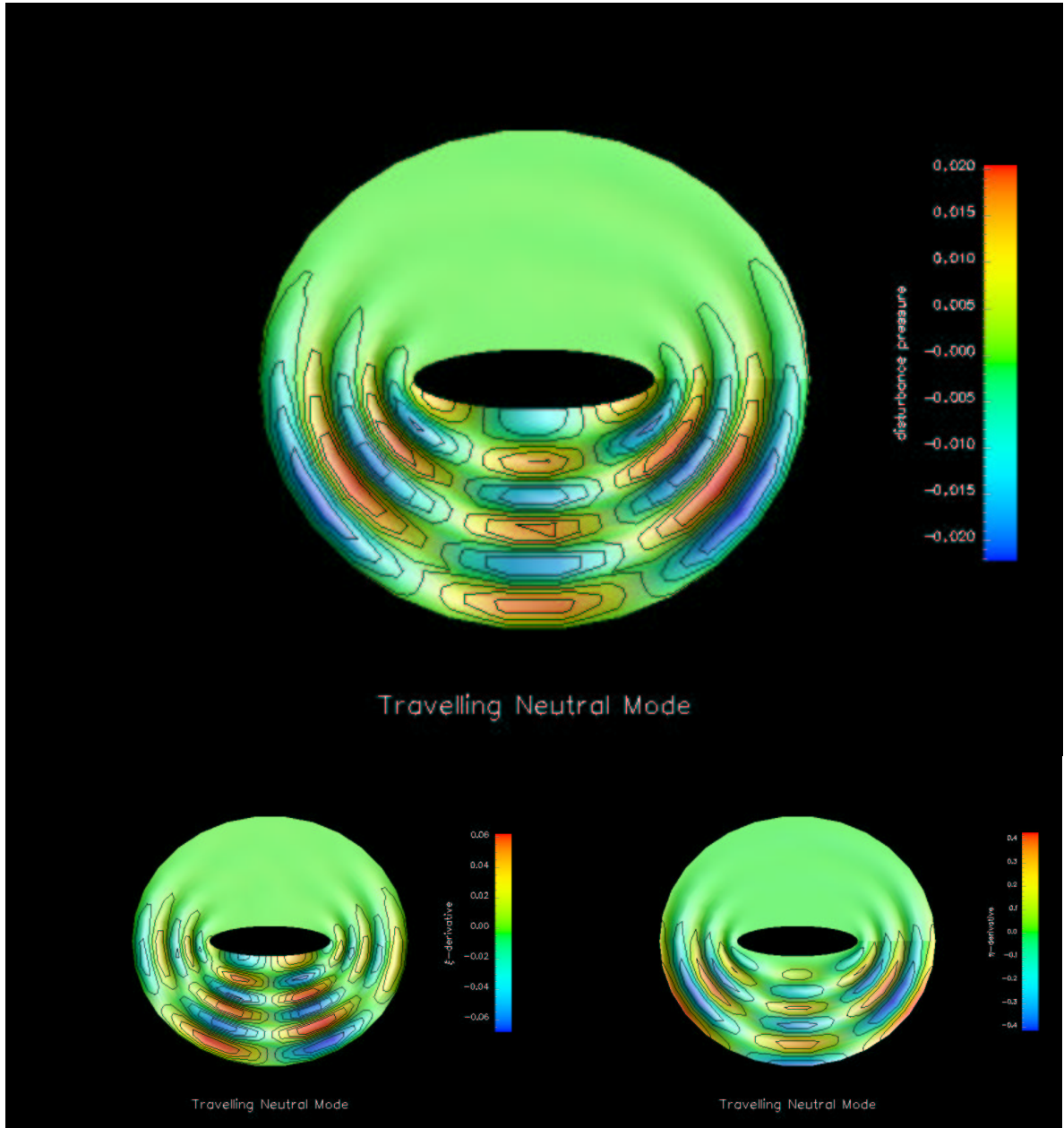
Figure 23. A travelling neutral mode - member of family C - at $M = 4.0$. Upper $\hat{p}$, lower left $\hat{p}_\xi$, lower right $\hat{p}_\eta$.
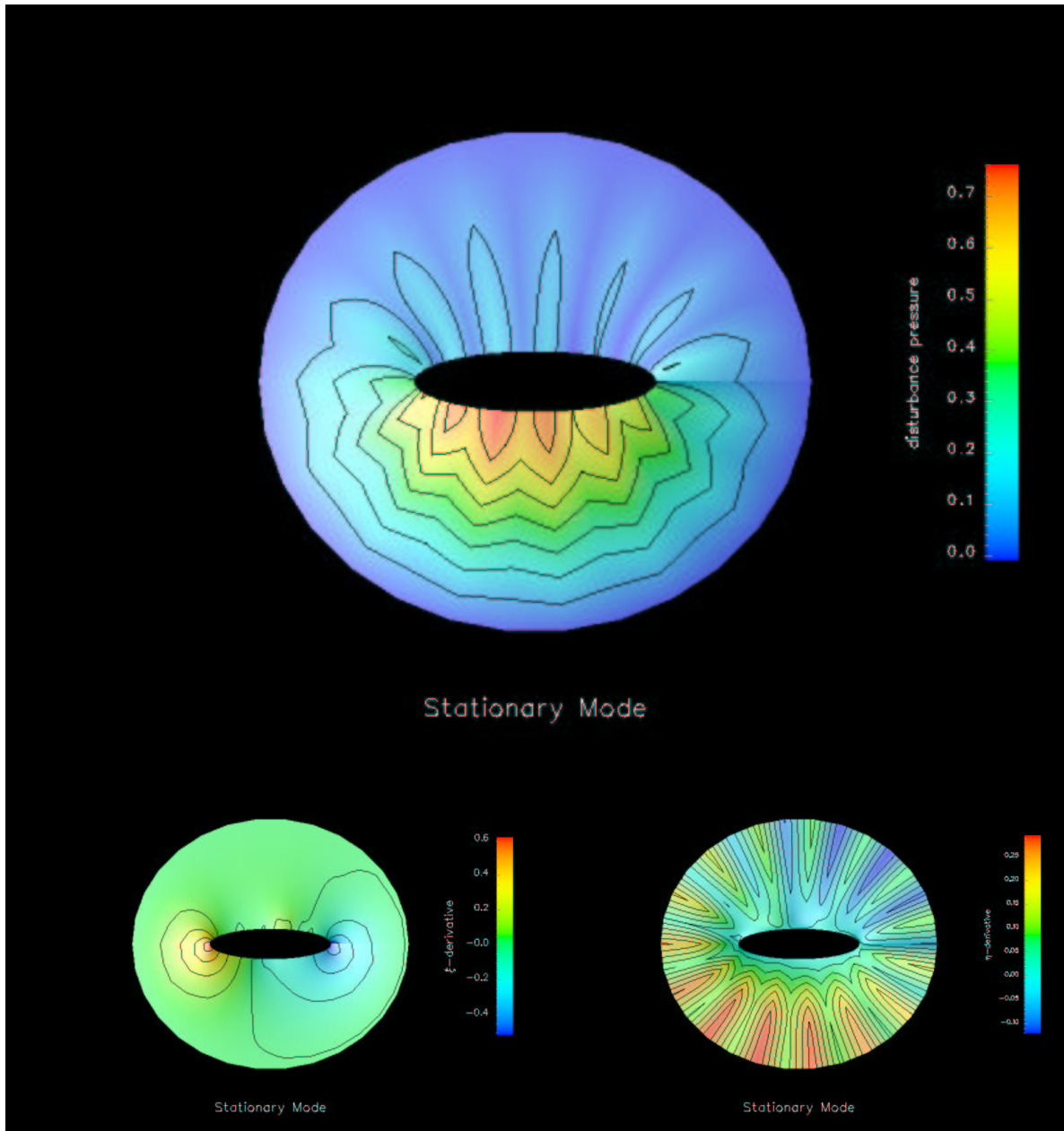
Figure 24. A stationary mode - member of family D - at $M = 4.0$. Upper $\hat{p}$, lower left $\hat{p}_\xi$, lower right $\hat{p}_\eta$.
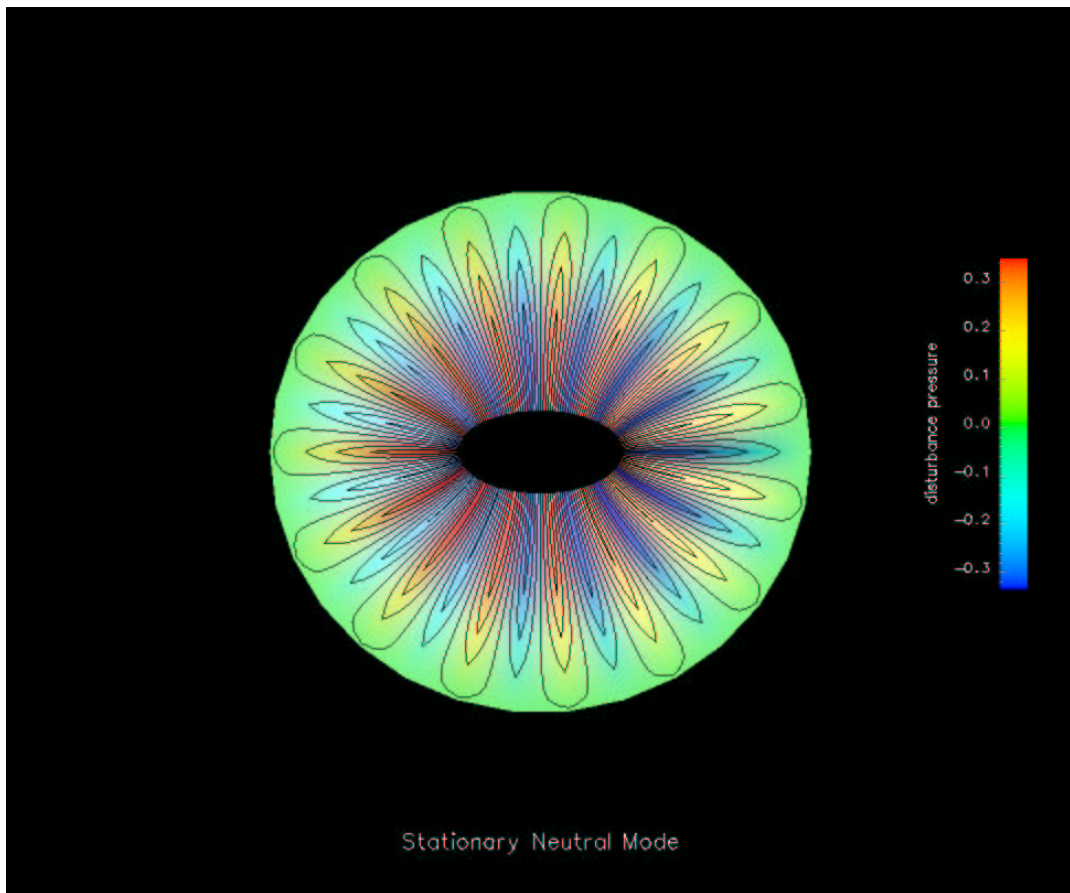
Figure 25. A stationary neutral pressure eigenmode at $M = 8.0$.
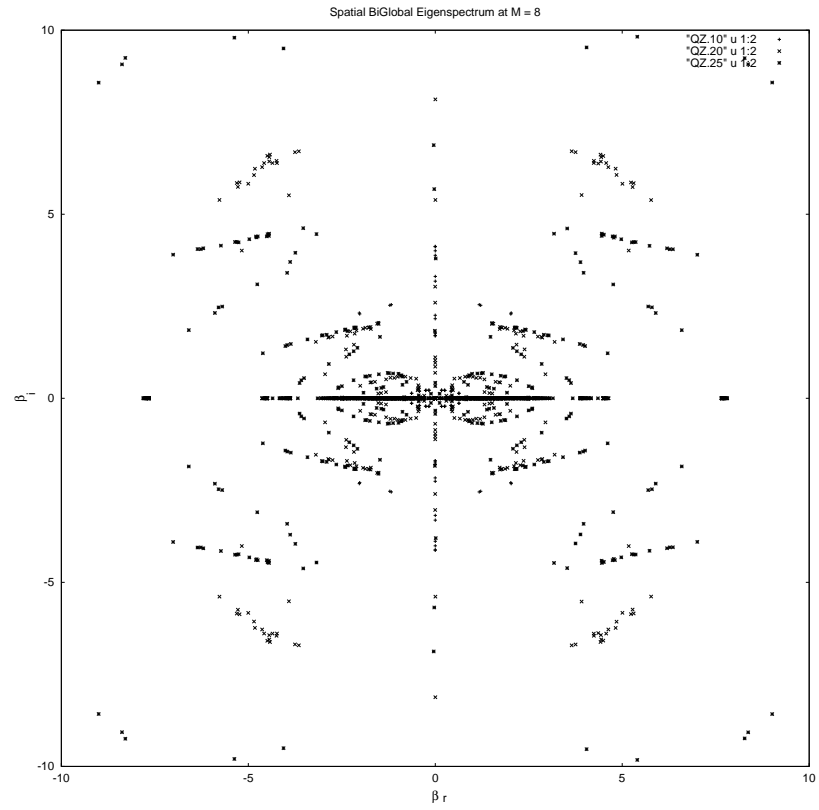
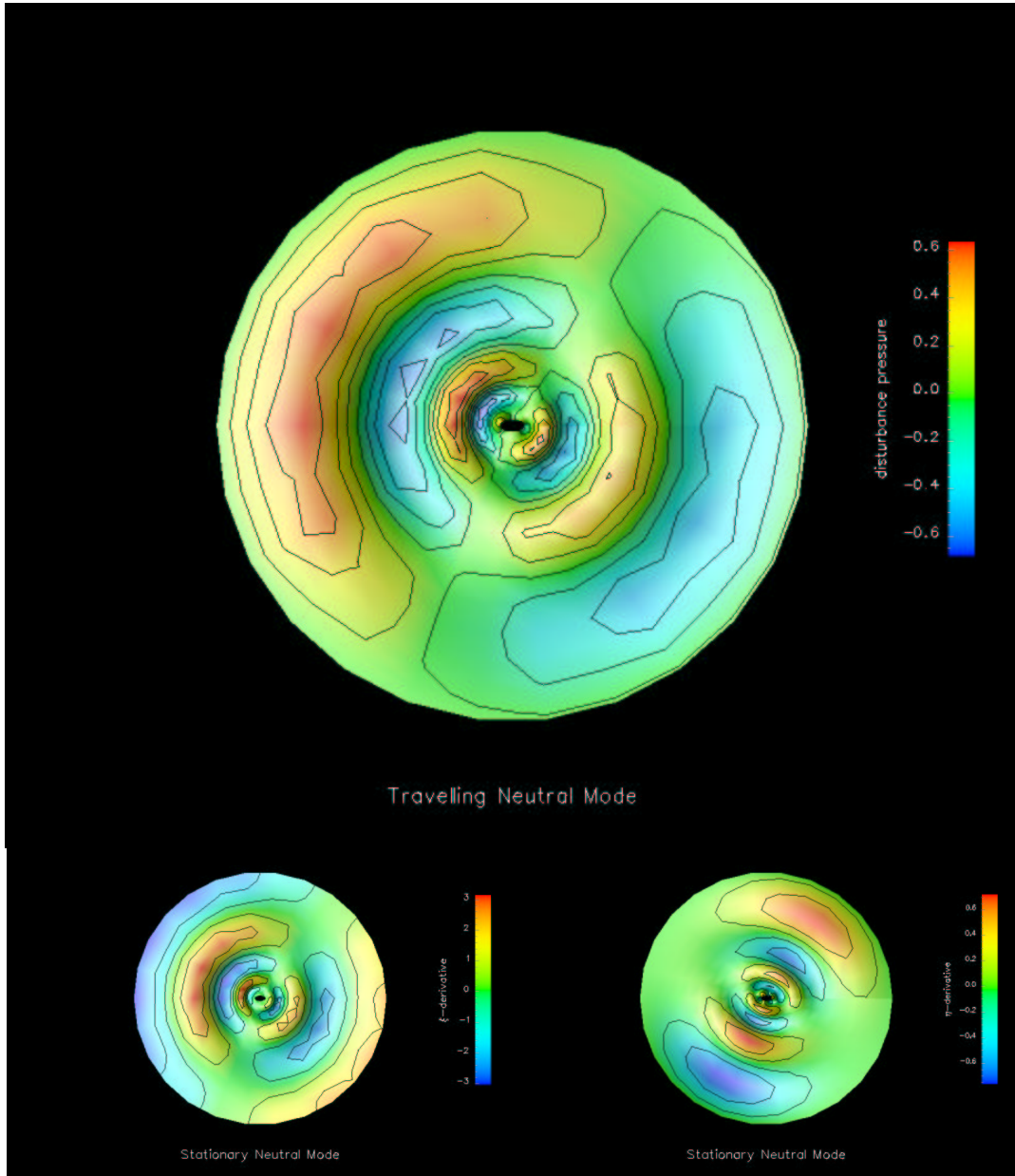Figure 26. Eigenvalue spectra at $M = 8$ and resolutions $10^2, 20^2$ and 25^2

Figure 27. A stationary neutral mode at $M = 8.0$. Upper $\hat{p}$, lower left $\hat{p}_\xi$, lower right $\hat{p}_\eta$.
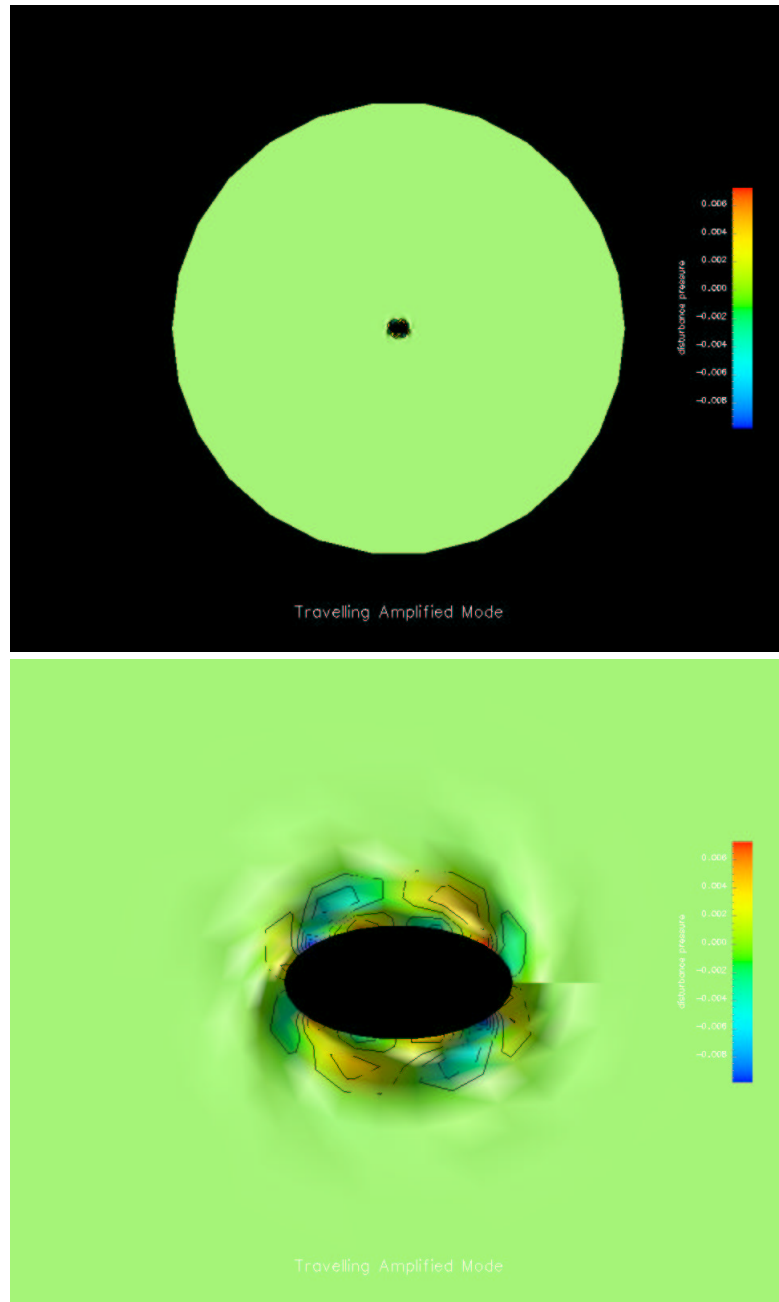
V. Theofilis

Figure 28. Disturbance pressure travelling eigenmode at $M = 8.0$. Upper, full calculation domain; lower, detail in the neighbourhood of the elliptic cone.
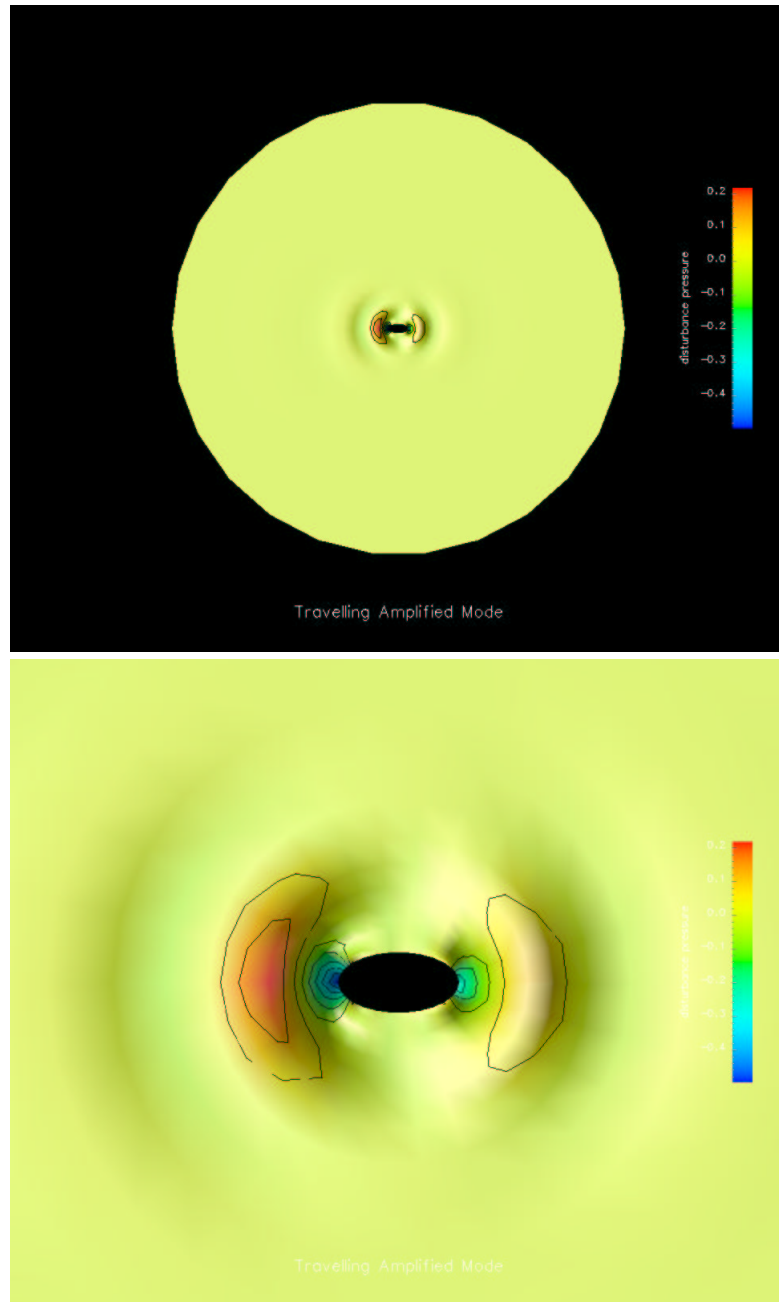
Figure 29. Disturbance pressure travelling eigenmode at $M = 8.0$. Upper, full calculation domain; lower, detail in the neighbourhood of the elliptic cone.